Additive manufacturing of inherently porous polymers: Polymerized high internal phase emulsion (polyHIPE) structures via vat photopolymerization

Nihan SENGOKMEN OZSOZ

The University of Sheffield

Faculty of Engineering

Department of Materials Science and Engineering

A thesis submitted in fulfillment of the requirements for the degree of
Doctor of Philosophy

Submitted December 2023

Acknowledgements

"Science is the only true guide in life."

Mustafa Kemal Ataturk

I would like to express my gratitude to individuals and institutions, all of whom have played a significant role in shaping my PhD experience.

First of all, I gratefully acknowledge the Turkish Ministry of National Education for my PhD fellowship; this research would not be possible without their financial support.

I would like to convey my deepest gratitude to my supervisor, Prof Frederik Claeyssens, for consistently being a supportive mentor. I appreciate your trust in allowing me to work independently, for encouraging me to aspire to significant goals, and for showing concern for both my development as a scientist and as an individual.

I would like to thank Prof Neil Cameron and Dr Chris Holland for agreeing to be examiners for my PhD Viva. Additionally, I would like to thank Prof Russell Goodall and Dr Nicola Green, who assessed my work during the first year and second year Viva, for engaging in insightful discussions that broadened my perspectives.

I also would like to thank Dr Rebecca Boston for letting me use a high-temperature oven, a crucial component in Chapters 3 and 4 of this thesis, in her laboratory, Dr Colin Sherborne for his kind helps on 3D printing of PolyHIPEs and inspiring discussions on their applications, Dr Nik Reeves-McLaren for training me on Raman Spectroscopy, Dr Ian Ross for training me on Scanning Electron Microscopy, Dr Oday Hussein for training me on Helium Pycnometry, ATR/FTIR, Thermogravimetric analysis and for providing technical support on Mercury Intrusion Porosimetry, Dr Robert Moorehead for training me on X-ray Diffractometer, Dr Vanessa Singleton for helping always in Kroto Labs, Dr Enes Durgut for being always there when I need any kind of help.

I thank Mina Aleemardani, with whom I have shared my PhD journey from beginning to end. Despite having entirely different projects, thank you for always trying to help me.

Abstract

High internal phase emulsions (HIPEs) show promise as vat photopolymerization additive manufacturing (AM) resins for creating innovative lightweight porous materials. Despite their potential, HIPEs often scatter light during the AM process, resulting in poorly defined and low-resolution structures. However, the incorporation of light absorbers can significantly enhance printing resolution. This study investigated the inclusion of light absorbers into the HIPE-based resin and assessed the compatibility of these resins with a commercial vat photopolymerization additive manufacturing setup. A water-in-oil emulsion, stabilized by the surfactant (hypermer) and formulated with 2-ethylhexyl-acrylate and isobornyl-acrylate was used in this study. Light absorbers, including hydrophobic beta-carotene and hydrophilic tartrazine molecules dissolving in the organic and aqueous phases respectively, were incorporated. The use of beta-carotene and tartrazine together was found effective in achieving the best 3D printing resolution. Moreover, the emulsion remained stable throughout the printing process, resulting in a porous polyMIPE structure with open surface porosity.

Expanding the application of 3D-printed polyHIPE structures, their utility as templates for electroless nickel plating to create highly porous metallic lattice structures with consistent wall thickness was examined. The electroless nickel plating process on polyHIPEs was optimized and the effects of different atmospheres during the heating process to remove the polyHIPE template from metallized 3D-printed polyHIPE lattice structures were explored. Distinct compounds were formed in various atmospheres, with fully oxidized nickel-coated polyHIPEs in an air atmosphere and the formation of nickel phosphide (Ni_3P) structures in argon and reducing atmospheres alongside Ni metal. Notably, the porous structure of the polyHIPEs was retained in argon and reducing atmospheres, where the internal structure undergoes complete carbonization. This study demonstrated the versatility of intricate polyHIPE structures as templates for creating ultra-porous metal-based lattices.

Furthering the exploration, inherently porous polyHIPE lattices with three distinct porosities (80%, 85%, and 87.5%) at various temperatures (500ºC, 600ºC, 700ºC, and 800ºC) were pyrolyzed to fabricate porous carbon structures. The successful carbonization was confirmed through Raman spectra and XRD analysis. Mechanical testing results indicated a higher

Young's modulus in carboHIPEs compared to polyHIPEs, with carboHIPE lattices demonstrating a lower Young's modulus compared to monolithic carboHIPE discs. This comprehensive exploration contributed valuable insights into the design and performance of hierarchically porous carbon materials fabricated using 3D-printed polyHIPE lattices.

In conclusion, this study established the potential of HIPEs as printing resins for creating inherently porous intricate structures and utilizing them as templates for producing highly porous complex metal-based and carbon structures.

Published Content and Contributions

Chapter 2 has been adapted from:

1. N. Sengokmen Ozsoz, S. Pashneh-Tala, and F. Claeyssens, "Optimization of a High Internal Phase Emulsion-Based Resin for Use in Commercial Vat Photopolymerization Additive Manufacturing," *3D Print Addit Manuf*, **2023**, doi: 10.1089/3dp.2022.0235.

   Contributions: N.S.O. designed and performed the experiments, analyzed the results, and wrote the manuscript.

Chapter 3 has been adapted from:

2. N. Sengokmen-Ozsoz, R. Boston, and F. Claeyssens, "Investigating the Potential of Electroless Nickel Plating for Fabricating Ultra-Porous Metal-Based Lattice Structures Using PolyHIPE Templates," *ACS Appl Mater Interfaces*, 15, 25, 30769–30779, **2023**, doi: 10.1021/acsami.3c04637.

   Contributions: N.S.O. designed and performed the experiments, analyzed the results, and wrote the manuscript.

Table of Contents

List of Figures

List of Tables

Abbreviations

µm	Micrometer
µSL	Micro-stereolithography
3D	Three dimensional
Ag	Silver
AM	Additive manufacturing
Ar	Argon
ATR	Attenuated total reflectance
Au	Gold
BJT	Binder jetting
CAD	Computer-aided design
carboHIPE	Carbonized high internal phase emulsion
CDLP / CLIP	Continuous digital light processing / Continuous liquid interface production
DED	Directed energy deposition
dH$_2$O	Distilled water
DIW	Direct ink writing
DLP	Digital light processing
EDX	Energy dispersive X-ray
EHA	2-ethylhexyl acrylate
FDM	Fused deposition modelling
FFF	Fused filament fabrication
FTIR	Fourier Transform Infrared
H$_2$	Hydrogen

H_3BO_3	Boric acid
HA	Hydroxyapatite
HCl	Hydrochloric acid
HIPE	High internal phase emulsion
IBOA	Isobornyl acrylate
kN	Kilonewton
kV	Kilovolt
LCD	Liquid crystal display
LED	Light emitting diode
MEX	Material extrusion
mg	Milligram
MIPE	Medium internal phase emulsion
MJF	Multi jet fusion
MJT	Material jetting
mm	Millimeter
MOF	Metal organic framework
MPa	Megapascal
N	Newton
N_2	Nitrogen
Ni	Nickel
$Ni_{0.98}C_{0.02}$	Nickel carbide
$Ni_{12}P_5$	Nickel phosphide
Ni_2P	Nickel phosphide
Ni_3P	Nickel phosphide

NiO	Nickel oxide
nm	Nanometer
O	Oxygen
O/W	Oil-in-water
P	Phosphorus
PBF	Powder bed fusion
PBF-EB	Electron beam powder bed fusion
PBF-LB	Laser powder bed fusion
PCL	Polycaprolactone
Pd	Palladium
PdCl$_2$	Palladium chloride
PFDMA	Propylene fumarate dimethacrylate
PLA	Polylactic acid
polyHIPE	Polymerized high internal phase emulsion
polyMIPE	Polymerized medium internal phase emulsion
SEM	Scanning electron microscopy
SHL	Sheet lamination
SLA	Stereolithography
SLS	Selective laser sintering
SnCl$_2$	Tin chloride
ST-co-DVB	Styrene-co-divinylbenzene
STL	Standard triangulation language
T$_g$	Glass-transition temperature
TGA	Thermogravimetric analysis

TiO$_2$	Titanium dioxide
T$_m$	Melting temperature
TMPSM	3-(trimethoxysilyl)propyl methacrylate
TMTPA	Trimethylolpropane triacrylate
UV	Ultraviolet
UV/Vis	Ultraviolet/visible
VPP	Vat photopolymerization
W/O	Water-in-oil
XRD	X-ray diffraction

CHAPTER 1

Introduction

1.1. Additive Manufacturing

Objects are fabricated utilizing diverse techniques and materials, depending on the intended application. Traditional manufacturing processes, like casting or injection molding, result in objects taking their ultimate form, whereas subtractive manufacturing approaches, including milling and lathing, shape objects by eliminating material. An alternative manufacturing technology to these well-established methods is additive manufacturing (AM), which was initially introduced by Hideo Kodama in 1980 [1], [2], [3].
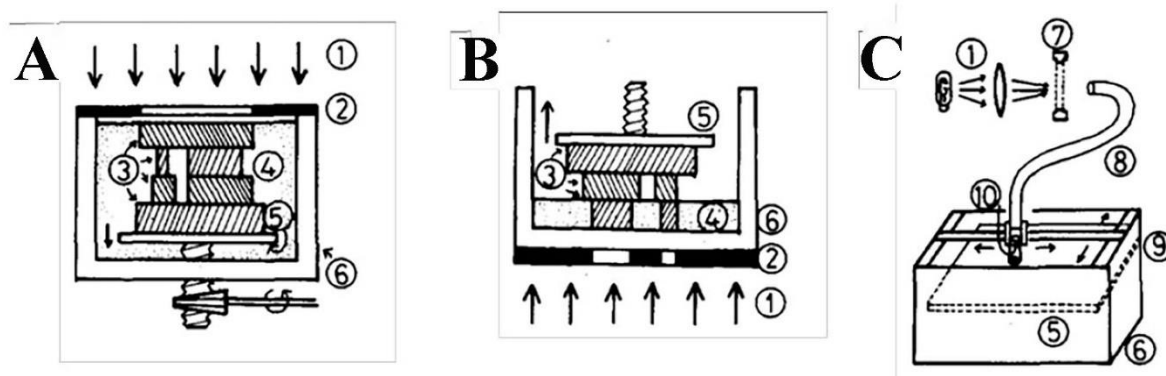
Figure 1. 1. Schematic diagrams of Kodama's three types of stereolithography apparatuses. Photopatterning is controlled by (**A**) a mask with light projected from the top, (**B**) a mask with light projected from the bottom, or (**C**) a scanning fiber transmitter mounted on an XY plotter. (① UV light, ② mask, ③ solidified polymer layers, ④ liquid photoresin, ⑤ build plate, ⑥ vat, ⑦ shutter, ⑧ optical fiber, ⑨ XY plotter, ⑩ optical lens) Adapted with permission from [4] Copyright 1981 American Institute of Physics.

Following this, in 1984, Charles Hull secured a patent for the pioneering 3D printing technology, known as stereolithography (SLA) [5]. Additionally, despite the fact that Kodama's patent application was unsuccessful, he is widely acknowledged as the inventor of additive manufacturing. The schematic of Kodama's stereolithography apparatuses Hull's 1984 stereolithography patent are illustrated in Figure 1.1 and Figure 1.2, respectively.

In brief, additive manufacturing, a layer-by-layer fabrication method, allows for the production of three-dimensional objects using computer-aided design (CAD).
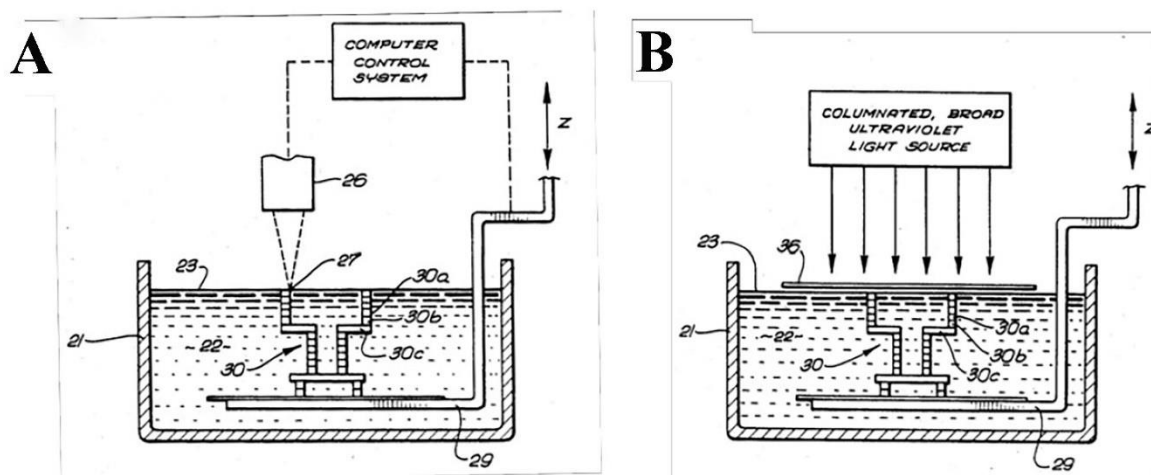
Figure 1. 2. Schematic diagrams of Hull's 1984 stereolithography patent. Photopatterning is controlled by **(A)** a raster scanned spot source or **(B)** a masked collimated light source. (21, resin container; 22, UV-curable liquid resin; 23, surface of the liquid resin; 26, programmable source of UV light; 27, spot source of UV light; 29, elevator platform; 30, printed three-dimensional object composed of layers such as 30a/b/c; 36, mask for collimated UV source) Adapted from reference [5].

From these initial developments the field of additive manufacturing emerged, for example in 1988 fused filament fabrication was developed by Scott Crump [6], and selective laser sintering was developed by Deckard and Beaman in the mid-80s Nowadays, additive manufacturing technologies are primarily categorized into seven groups according to ISO/ASTM 52900:2015 - Additive Manufacturing-General Principles-Terminology. These categories, which include

sheet lamination (SHL), directed energy deposition (DED), binder jetting (BJT), material jetting (MJT), powder bed fusion (PBF), material extrusion (MEX), and vat photopolymerization (VPP), are illustrated in Table 1.1. Each sub-method differs from the others in terms of curing, the types of materials used in production, and the manufacturing process [2], [7].

All the methods mentioned in Table 1.1 are described briefly, while vat photopolymerization is explained in more detail since the scope of this thesis focuses on vat photopolymerization additive manufacturing of inherently porous polymers.

Table 1. 1. Additive manufacturing categories.
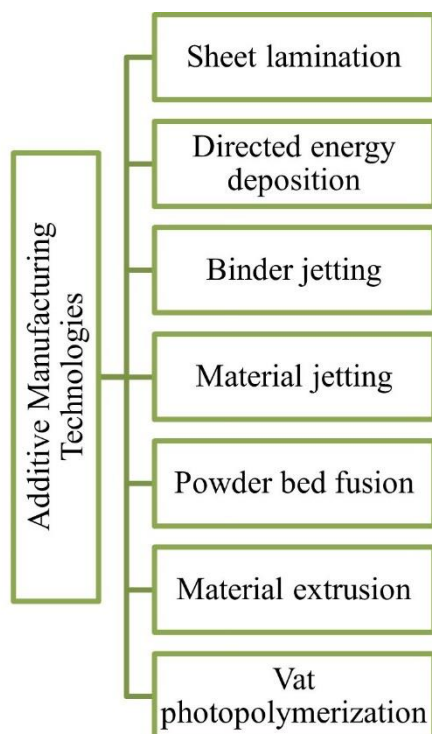
1.1.1. Sheet Lamination

Sheet lamination additive manufacturing technique primarily utilizes paper material sheets to create three-dimensional objects [8], [9]. The sheet lamination method can be divided into two subcategories: laminated object manufacturing and ultrasonic consolidation [8].

In this method, pre-manufactured material sheets, cut using a laser cutter, are used to produce the final part [8], [9]. Each material sheet forms one layer of the final part, making this process faster than other additive manufacturing techniques [8], [9].

1.1.2. Directed Energy Deposition

Directed energy deposition enables the fabrication of net-shape items from wires or powders layer by layer (Figure 1.3A) [10], [11]. Although directed energy deposition shares similarities with powder bed fusion (PBF), it differs from PBF in terms of the process principle. In this technique, the feeding material (wires or powder) and energy source are applied simultaneously, whereas in powder bed fusion, the order is powder followed by the energy source [11], [12].

1.1.3. Binder Jetting

Binder jetting is used to create three-dimensional objects by consolidating powders (Figure 1.3B) [13]. In this method, powder is initially spread across the building platform using a roller, and then a binder liquid is deposited onto the powder particles via a print head as the second step [13], [14]. After each layer is thermally cured with a heater, these steps are repeated until the final product, specified before the fabrication process begins, is achieved [13], [14].

Finally, unbound powders are removed, and the resulting product is sintered in a furnace to achieve the desired strength and density [13], [14]. However, it's worth noting that this post-processing step may take longer than the actual production, potentially leading to a significant increase in costs [14].

1.1.4. Material Jetting

Material jetting is also known as inkjet 3D printing, and it involves the deposition of liquid photopolymers onto a base platform layer by layer using printheads (Figure 1.3B) [15]. Furthermore, UV light is employed to solidify these photopolymers, which means that curing is achieved through UV light in this method [15].

Generally, while material jetting is commonly used for fabricating prototypes, it is also well-suited for manufacturing lightweight honeycomb structures, scaffolds, and lifestyle wearable products [16], [17], [18].

1.1.5. Powder Bed Fusion

Powder bed fusion is one of the additive manufacturing techniques that employs a heat source to consolidate metal or polymer powder, thereby creating three-dimensional objects (Figure 1.3C) [19], [20]. The heat source can be either a laser or an electron beam [21]. Depending on the heat source, powder bed fusion is referred to as laser powder bed fusion (PBF-LB) or electron beam powder bed fusion (PBF-EB) [21], [22], [23].

This three-dimensional fabrication method allows for the production of complex and uniquely shaped components with superior mechanical properties [19], [20]. Consequently, it is preferred over traditional manufacturing methods [19], [20], [21].
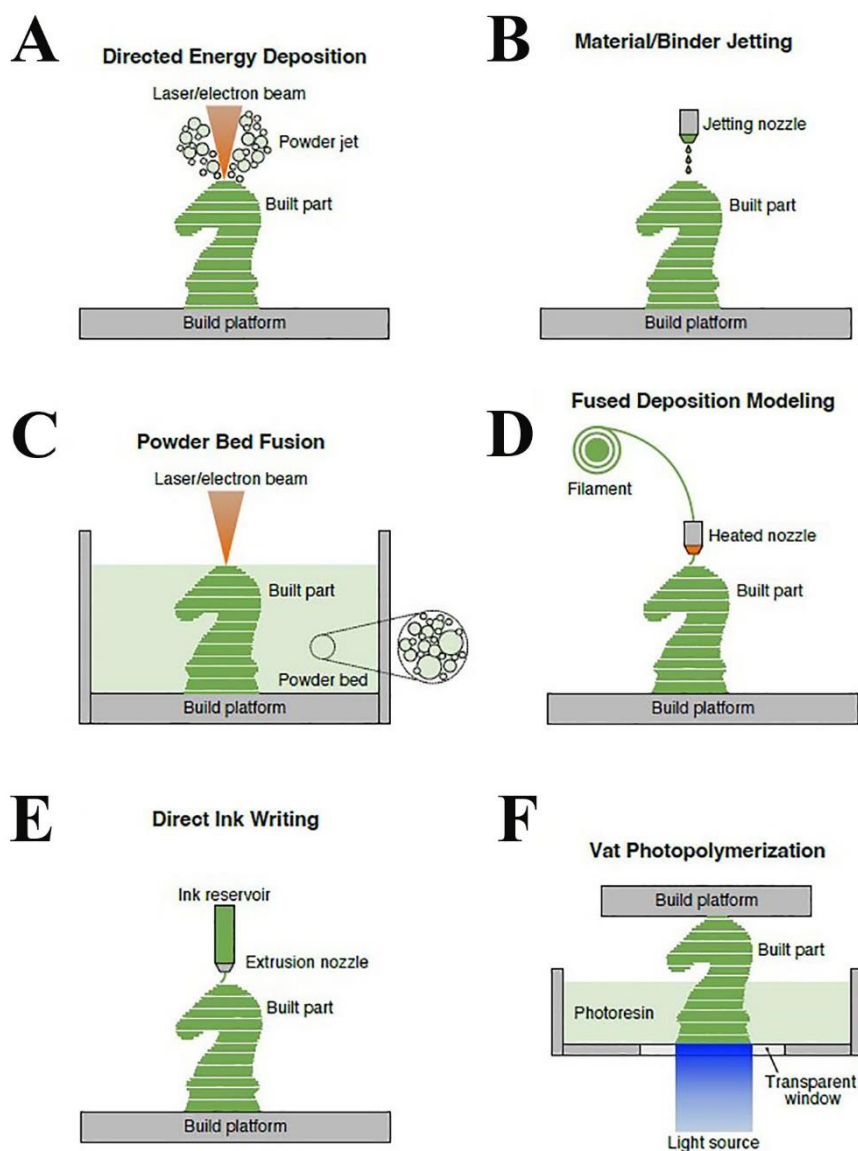
Figure 1. 3. Schematic diagrams of common additive manufacturing methods. (**A**) Directed energy deposition (**B**) Material/Binder jetting, (**C**) Powder bed fusion, (**D**) Fused deposition modeling, (**E**) Direct ink writing, and (**F**) Vat photopolymerization (DLP technique). (**A-B**) Adapted from [24] Copyright 2022, (**C-F**) Adapted with permission from [25] Copyright 2022 The Materials Research Society.

1.1.6. Material Extrusion

Material extrusion, also known as fused filament fabrication (FFF) or fused deposition modeling (FDM), is an often-used additive manufacturing techniques for thermoplastic polymer objects [26], [27]. Essentially, a fused deposition modeling printer includes either a single-nozzle head or a multi-extruder nozzle head which is computer numerically controlled (CNC) [27]. If it contains multiple nozzles, one is used for the main material, while the others can be used for additional modeling materials and/or supports [27].

In FDM technique (Figure 1.3D), the production principle involves melting thermoplastic polymer filaments and extruding them onto a base plate from heated nozzles [28]. The nozzle head moves upward, or the base plate moves downward automatically to create the next layer after each layer is formed. If the shear thinning inks are used rather than thermoplastics, the method is called direct ink writing (DIW) (Figure 1.3E). Furthermore, when the shear thinning inks are biocompatible hydrogels, with inclusion of living cells, this technique is called bioprinting.

1.1.7. Vat Photopolymerisation

Vat photopolymerization is another additive manufacturing technology that relies on the curing of photosensitive resin using a laser or ultraviolet light [2], [29], [30] (Figure 1.3F). Essentially, the light-sensitive liquid resin is cured in a vat until it completely solidifies.

It would be beneficial to review the 3D printing process and the photopolymerization principle separately to gain a detailed understanding of the working principle of vat photopolymerization.

The 3D printing process involves three main steps to fabricate three-dimensional objects: pre-processing, processing, and post-processing [2], [30]. The first step begins with the design of a 3D model using computer-aided design software [2]. Once the design is completed, the 3D model is converted into the standard triangulation language (STL) format [2]. In the second step, the STL model is sliced, and if necessary, a base and/or supports are added using software compatible with the 3D printer. The sliced model is then transferred to the 3D printer [2], [30]. Before printing the object, printing parameters are set and optimized; afterward, the object is created [2]. Finally, post-processing involves removing the cured objects from the 3D printer

and washing them to clean off any residual resin [2], [30]. Additionally, if needed, post-curing may be applied [30].

The photopolymerization process requires photopolymers that can be cured using ultraviolet light and sometimes visible light [2], [29]. A light-sensitive photopolymer is placed in a vat, and the polymerization reaction is initiated while the curing light is applied [2]. After completing the crosslinking of the photopolymer, a solidified object with the same shape and dimensions as the 3D model previously transferred from the computer in STL format is obtained [2], [31], [32].
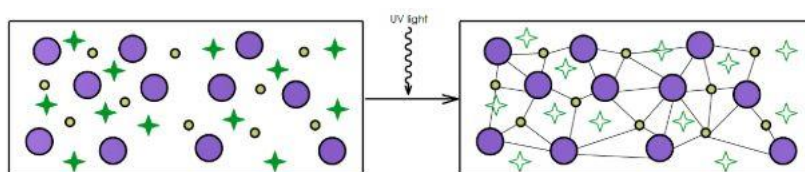
Figure 1. 4. Liquid photopolymer to polymerization. Small circles, purple circles, and stars symbolize monomers, oligomers, and photoinitiators, respectively. Adapted from [2] Copyright 2021.

Figure 1.4 presents the photopolymerization process schematically. Photoinitiators enable the formation of chains between monomers and oligomers by releasing free radicals and reagents when ultraviolet light is applied to the liquid photosensitive resin [2], [32]. Therefore, objects can be produced by repeating this reaction for each layer.

Vat photopolymerization can be categorized into three sub-categories based on curing technologies: stereolithography (SLA), digital light processing (DLP), and continuous digital light processing/continuous liquid interface production (CDLP/CLIP) [2], [33].

In stereolithography, a laser is used to cure a light-sensitive polymer that is placed in a transparent tank [2], [34]. The curing process is the typical photopolymerization process explained above. On the 3D printer side, the build platform moves either down or up, depending on whether the 3D printer is working in a top-down or bottom-up manner, respectively [34]. This process continues until the designed object is obtained.

Digital light processing differs from stereolithography only in terms of the curing technique. While stereolithography uses a mirror to reflect the laser, digital light processing utilizes a digital light projector [35]. In this technique a 2D binary image is projected, notably speeding up the production process compared to stereolithography, which builds up the image pixel by pixel. In 2019, computed axial lithography was reported and allowed for a single 3D object to be rapidly produced in a rotating bath of resin via exposure to a dynamically changing light field [36].

Continuous digital light processing/continuous liquid light processing method employs an oxygen-permeable window and digital projection with LEDs for the curing process [37]. An area is created by the oxygen-permeable window, allowing the flow of photocurable polymer between the window and the printed object. Consequently, this leads to an increase in the resolution of the final object and a reduction in the rate of printing failures. The CLIP technology was recently improved by introducing a syringe pump to inject the resin (iCLIP) [38].

Materials for vat photopolymerization must include a light-curable, reactive, and cross-linkable monomer or a blend of monomers and an initiator to initiate the photopolymerization reaction [33]. There are various commercial resin types available as starting materials for vat photopolymerization, categorized as standard resin, structural resin, tough and durable resin, elastic and flexible resin, ceramic and castable wax resin, and biocompatible resin, which can be selected based on the specific application [2]. Furthermore, photocurable resins can be prepared by mixing monomers, a crosslinker, and a photoinitiator. The most commonly used monomers for preparing starting materials for vat photopolymerization are acrylates and methacrylates [33].

In this thesis, water-in-oil high internal phase emulsions were used as resin for vat photopolymerization additive manufacturing. These emulsions are created by mixing monomers, a crosslinker, a photoinitiator, and water through the emulsion templating technique. Section 1.3 provides detailed information about the formation mechanisms and fundamentals of high internal phase emulsions.

1.2. Polymer Additive Manufacturing
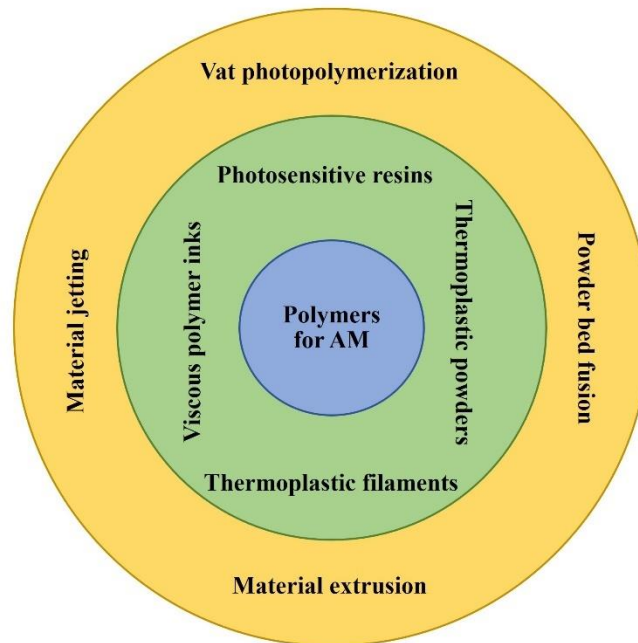
Figure 1. 5. Polymer materials, used for typical polymer AM techniques.

Various forms of polymers are employed in the AM methods described above, including PBF, MJT, MEX, and VPP. Feeding materials can be in the form of thermoplastic powders, thermoplastic filaments, viscous inks, and photosensitive resins (Figure 1.5).

Thermoplastics possess the distinctive ability to soften or melt under elevated temperatures and solidify when cooled, granting them the flexibility to undergo reshaping and recycling procedures [39]. This class of materials is classified into two categories: amorphous and semicrystalline, each defined by specific molecular arrangements. In the case of amorphous thermoplastics, exemplified by polystyrene and polycarbonate, their molecular structures lack order and confer flexibility, transiting to a glassy state beyond the glass transition temperature (T_g) [40]. In contrast, semicrystalline thermoplastics such as polyamides exhibit distinct T_m and T_g points that correspond respectively to their crystalline and amorphous domains [41]. Notably, the viscosity of semicrystalline thermoplastics reduces when heated past their T_m, as they shift from solid to a more fluid-like state [42]. The processing of powdered forms of

thermoplastics and their composites can be achieved through the Powder Bed Fusion (PBF) technique, encompassing methods like Selective Laser Sintering (SLS) and Multi-Jet Fusion (MJF), which share similarities in their sintering mechanisms and material prerequisites [39].

Thermoplastic filaments and their composite variants are suitable for fabrication using the Fused Deposition Modeling (FDM) technique [39]. In the standard FDM process, a filament is initially unwound through a feed pinch roller and directed into a heated liquefier. This heated segment causes the lower part of the filament to soften or melt, and it is subsequently pushed through the nozzle by the intact, solid upper portion of the filament, which is simultaneously introduced into the heated liquefier. The result of this process is the deposition of the liquefied filament, referred to as the "printed road," which then cools and solidifies on the build platform.

Viscous polymer inks that are suitable candidates for the Direct Ink Writing (DIW) process encompass two primary categories: reactive resins, including photocurable and thermally curable resins, and polymer solutions [39]. Particularly prominent within this realm are highly viscous photocurable resins, extensively employed in DIW applications [43], [44]. These resins necessitate the integration of an external source of ultraviolet (UV) light within DIW systems to facilitate their photo-curing upon deposition, often termed as UV-assisted DIW. Noteworthy among the photocurable options are hydrogels such as gelatin methacrylate (GelMA), capable of undergoing chemical gelation when exposed to UV radiation. Beyond photosensitive alternatives, thermally curable resins, exemplified by epoxy resin, which solidify through heat-induced processes, have been effectively harnessed [45]. Polymer solution inks, formed by dissolving polymers in suitable solvents, present a versatile avenue for DIW, with their viscosity amenable to adjustment by manipulating factors like polymer molecular weight and volume/mass fractions.

Photosensitive resins, commonly used in VPP and MJT techniques, react to radiation, forming interconnected networks and solidifying permanently [39]. These resins consist of photoinitiators, monomers, oligomers, and additives, each playing a crucial role. Monomers, characterized by their small sizes and variable functional groups (e.g., mono-, di-, tri-, tetra-functional), significantly influence curing, cross-linking, and final properties [36], [46].

The addition of additives improves resin performance. Inhibitors or retarders are used to regulate factors like penetration depth and gelation, counteracting reflected light effects. Common inhibitors include quinones, sterically hindered phenols, and oxygen [47]. Sensitizers

enhance the activity of photoinitiators, while solvents help modulate viscosity and facilitate heat transfer during polymerization [39].

1.2.1. Porous Polymers

A porous structure is generally described as a solid framework with notably abundant empty space enclosed within a well-defined boundary [48]. The pores become evident as enclosed air spaces, exhibiting individual pore sizes that range from the nanoscale to the macroscale. Porous structures combine large surface area, lightweight, and a high adsorption capability in comparison to solid structures.

Porous polymers are a sub-category of porous materials, preferred over other porous materials due to their ease of machinability [49]. This sub-category attracts the attention of researchers due to its controllable properties: well-defined porosities, high surface areas, unique structures, design flexibility, ease of use, cost-effectiveness compared to other materials, and suitability for various applications including thermal insulation, electrochemical energy storage, tissue engineering, contaminant removal, water treatment, and catalysis [48], [49], [50], [51], [52], [53].

After 1990, there has been an increasing interest in combining porous structures with polymer materials [49]. Polymers can be produced with a range of pore sizes, including microporous, macroporous, and millimeter-sized pores [49], [54]. The choice of pore size depends on the application area.

The conventional in-situ foaming technique is widely applied to manufacture porous materials like polymeric foams and sponges [48]. Additionally, methods like sacrificial templating and replica templating are employed to fabricate insulation pads and filtration foam [48]. For porous ceramic structures, the sol-gel method, combined with subsequent solvent exchange, proves highly efficient [48]. When shaping porous structures into straightforward bulk shapes, molding is the most commonly used manufacturing method. Precise control over porosity and pore arrangement is crucial for achieving specific functions. These emerging challenges go beyond the capabilities of traditional design and manufacturing approaches, hindering the creation of multi-scale and multi-functional porous networks within three-dimensional (3D) objects.

Additive manufacturing offers a versatile and efficient method for fabricating intricately designed 3D porous structures with minimal to no post-processing [48].

1.2.2. Additive Manufacturing of Porous Polymers

With the advancement of nature-inspired multi-scale porous structure design, 3D-printed porous networks can naturally achieve multiple functionalities [48]. This includes robust mechanical properties and hierarchical pore arrangements for energy storage, as well as nutrient transfer in tissues [48]. While 3D-printed porous networks outperform counterparts in various applications, the optimization of ink for 3D printing remains incomplete [48]. Optimized ink design and rheological behavior are expected to enhance the performance of multi-scale porous networks [48]. This also opens doors for novel applications such as triboelectric-based energy harvesting, solar energy storage, and carbon dioxide capture [48]. Despite promising advancements, current applications like 3D-printed batteries and bones are in their early stages and require in-depth research to ensure long-term stability, especially in challenging environments [48]. In-depth studies on degradation mechanisms and side effects, particularly for 3D-printed multi-scale porous structures, could offer meaningful insights.

1.3. High Internal Phase Emulsions / Polymerized High Internal Phase Emulsions (HIPEs / PolyHIPEs)

PolyHIPEs are a type of porous polymers known as polymerized emulsion-templated high internal phase emulsions (HIPEs) [49]. Emulsions are classified as high internal phase emulsions when the internal phase, dispersed within the continuous phase, exceeds 74% of the total volume [49], [55], [56]. When preparing HIPEs, two immiscible liquids, the internal phase and continuous phase, are mixed by gradually adding the internal phase to the continuous phase. The internal phase is then removed through solidification of the emulsion, resulting in a porous structure [57]. Figure 1.6 presents the production step of polyHIPEs. The solidification process can be done through light, a redox-based polymerization, or heat [58].
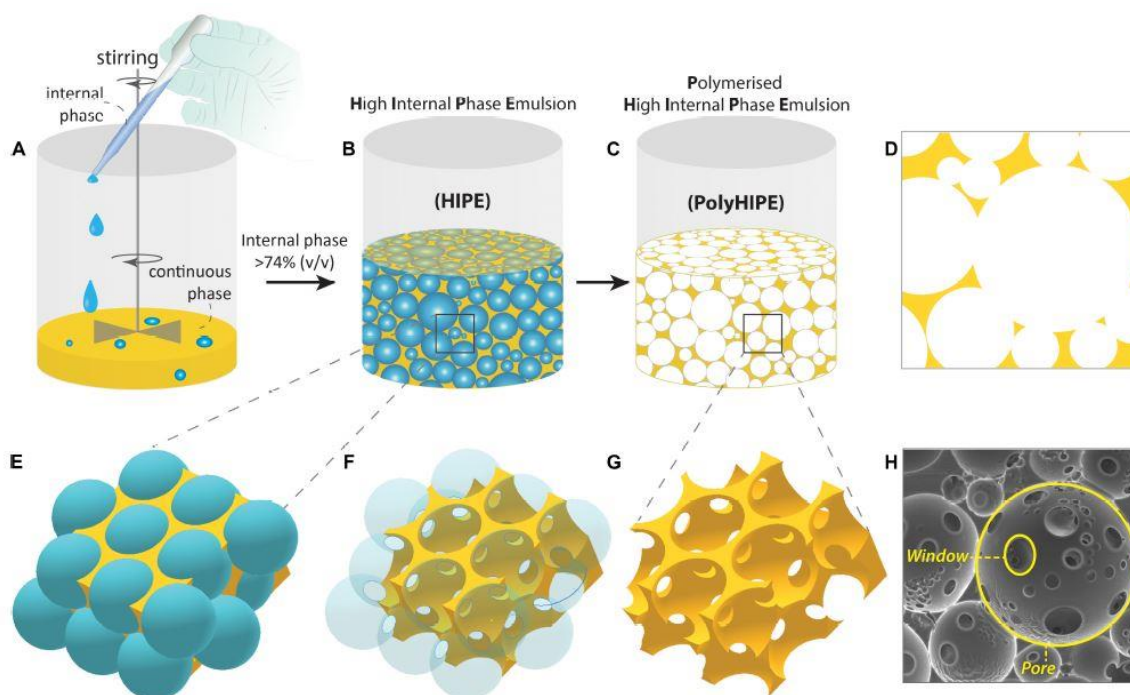
Figure 1. 6. Production steps of polyHIPEs. **(A, B)** The gradual addition of the internal phase into the continuous phase while the system is mixed, **(C)** polymerization of the high internal phase emulsion (HIPE), **(D)** 2D projection of PolyHIPE, **(E-G)** the formation of the pores and windows, and **(H)** scanning electron microscope image of the PolyHIPE. Adapted from [57] Copyright 2020.

1.3.1. High Internal Phase Emulsion Stabilization

PolyHIPEs are created from stable HIPEs formulated with stabilizing agents to reduce the interfacial tension between the continuous phase and the internal phase [49], [57], [59], [60]. If the interfacial tension is high, achieving the desired porous microstructure may be challenging. To address this issue, surfactants or particles can be used as stabilizers, as emulsions are thermodynamically unstable [61].

Typically, surfactants, which have a water-soluble (hydrophilic) head and an oil-soluble (hydrophobic) tail, are considered amphiphilic compounds, and are preferred as stabilizers. [57], [60]. Surfactants ensure the formation of a continuous film around the inner phase, which can either be the continuous phase in a water-in-oil (W/O) emulsion or the internal phase in an

oil-in-water (O/W) emulsion. This continuous film stabilizes the emulsion and reduces interfacial tension [57]. Figure 1.7A illustrates surfactant-stabilized emulsions. Additionally, surfactant types can be classified as anionic, cationic, non-ionic, or amphoteric, depending on the charge of the water-soluble head [57]. The amount of surfactant used to prepare the emulsion affects its stability and the microstructure and properties of polyHIPEs [57], [58].

When emulsions are stabilized using microparticles or nanoparticles placed at the interface between the continuous phase and the internal phase, they are referred to as Pickering emulsions [57], [60]. [57]Oil-wetted particles stabilize water-in-oil emulsions, while water-wetted particles stabilize oil-in-water emulsions, depending on the wetting properties of the particles. The schematic diagram of particle-stabilized emulsions is shown in Figure 1.7B. This stabilization method is less effective than surfactant stabilization because particles tend to disperse in the phase they are wetted by if they are not wetted by both phases [57], [60].
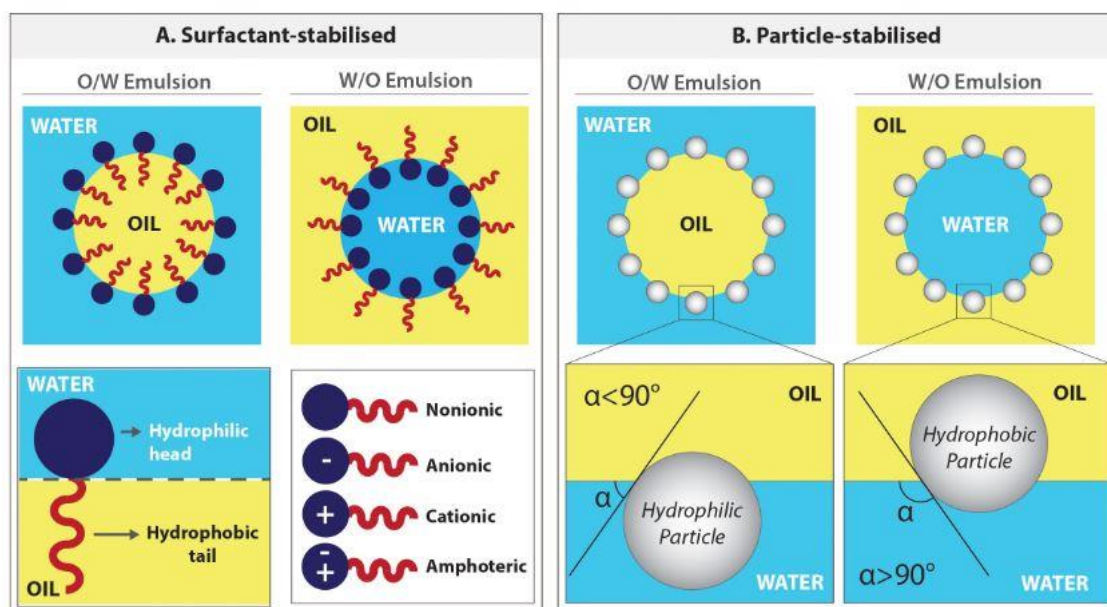
Figure 1. 7. (A) Surfactant-stabilized and **(B)** particle-stabilized emulsions. Adapted from [57] Copyright 2020.

1.3.2. Polymerization Mechanisms

PolyHIPEs are primarily synthesized from monomers such as styrenes, methacrylates, and acrylates, using free radical polymerization [49], [57], [59], [62]. Free radical polymerization can be initiated by photoinitiators, thermal methods, or redox reactions [57]. Typically, this is a chain-growth polymerization reaction where monomers are added one by one to a growing polymer chain.

Another polymerization mechanism is step-growth polymerization, where polymerization occurs through multifunctional monomers initially reacting to form dimers. These dimers then further react to form higher molecular weight oligomers. Condensation polymerization commonly follows this process. PolyHIPEs produced through condensation polymerization have had limited success [62]. Although this polymerization mechanism results in higher density and fewer interconnections in porous structures, successful production of polyurethane-based PolyHIPEs has been reported in the literature [62], [63].

Additionally, ring-opening polymerization is a relatively recent method that can be employed for the polymerization of ε-caprolactone and L-lactide-based HIPEs [57].

1.3.3. Polymerized High Internal Phase Emulsion Morphology

The morphology of polyHIPEs includes pore size, pore shape, pore interconnectivity, and the size of interconnecting holes [60]. Pore interconnectivity is a significant morphological property because it plays a crucial role in determining the applications of polyHIPEs [60]. Based on pore interconnectivity, polyHIPEs are categorized into two types: open-cell structures and closed-cell structures [60]. The pore size of polyHIPEs typically falls within the range of 1-150 µm [57].

The morphology of polyHIPEs can be controlled by adjusting the concentration of the stabilizer, the amount of internal phase, and the mixing speed [57], [60], [62]. Although the degree of porosity is primarily controlled by the internal phase, the volume of the internal phase may not always equal the percentage porosity measured after curing [57], [60], [62]. This discrepancy is because polyHIPE objects can shrink during drying or swell when washed with solvents [57]. Furthermore, the surfactant, acting as a stabilizer, plays a crucial role in

determining the porous structure. The concentration of surfactant can determine whether polyHIPEs will have an open-cell structure or a closed-cell structure [62].

1.3.4. Rheological, Physical, and Mechanical Properties

Rheologically, HIPEs are viscous emulsions in which viscosity depends on the concentration of the internal phase, the composition of the continuous phase, and mixing speed [49], [57]. Viscosity is a critical factor as it influences the reproducibility of the fabrication and printing quality.

Physically, the density of polyHIPEs is approximately 0.1 g/cm³, classifying them as low-density polymeric foams [49], [57]. Higher porosity can be achieved in polyHIPEs to further reduce their densities.

Mechanically, polyHIPEs can exhibit a range of mechanical properties through adjustments in their porous morphology and composition [49], [57]. When porosity is increased, mechanical properties tend to decrease. Furthermore, enhancing mechanical properties can be achieved by increasing pore size and density.

1.4. Additive Manufacturing of PolyHIPEs

The recent interest lies in utilizing additive manufacturing to create inherently porous structures. PolyHIPEs, due to their inherent porosity, facilitate the production of ultralightweight structures for various applications, including tissue engineering and catalysis. They can also serve as templates for fabricating ultralight and inherently porous metallic and carbon structures.

Inherently porous polyHIPEs were fabricated via light-based additive manufacturing by 2 different research groups in 2013 for the first time, simultaneously. Susec et al. explored the use of high internal phase emulsions (HIPEs) in lithography-based additive manufacturing using trimethylolpropane triacrylate (TMPTA) as the monomer and thiol-ene-based composition for higher toughness (Figure 1.8A) [64]. In the study conducted by Johnson et al., researchers investigated the use of acrylate-based HIPEs in a micro-stereolithography

(µSL) set-up and the research combined micro-stereolithography (µSL) and emulsion templating to create large-scale structures with precise micron-scale porosity control, integrating additive manufacturing with microstructuring (Figure 1.8B) [65]. Both investigations demonstrated the effective use of light-based additive manufacturing to polymerize high internal phase emulsions, resulting in the fabrication of complex porous structures that retain a morphology consistent with the bulk photopolymerization of HIPEs. This achievement highlighted the potential for manufacturing hierarchical materials through this approach.

In the following research, the four-layer woodpile structured scaffolds were fabricated from acrylate-based HIPEs via a single-photon direct-write micro-stereolithography setup for bone tissue engineering applications for the first time (Figure 1.8C) [66]. This study also showed that by varying ratios of EHA and IBOA monomers and overall porosity, the mechanical properties of the PolyHIPEs could be tuned. Furthermore, same research group were investigated hydroxyapatite (HA) containing acrylate-based HIPEs by using the same technique (Figure 1.8D) [67]. According to this research, the inclusion of HA particles improved the polyHIPEs' mechanical characteristics, specifically the Young's modulus and maximum stress at yield. Importantly, the inclusion of HA did not disrupt the phase separation or the porous microstructure of the HIPE. Similarly, Malayeri et al. fabricated inherently porous woodpile structure from acrylate-based HIPEs by using a single-photon direct-write micro-stereolithography setup to structurally mimic the trabecular bone for osteosarcoma-based 3D cell culture (Figure 1.8E) [68]. The researchers mentioned that these polyHIPE scaffolds were modified using acrylic acid plasma polymerization, displaying enhanced biocompatibility over extended periods, and facilitating the proliferation of osteosarcoma cells in a manner resembling in vivo conditions. This implied their potential uses in regenerative medicine for replicating tissue structures and simulating tumor behavior.
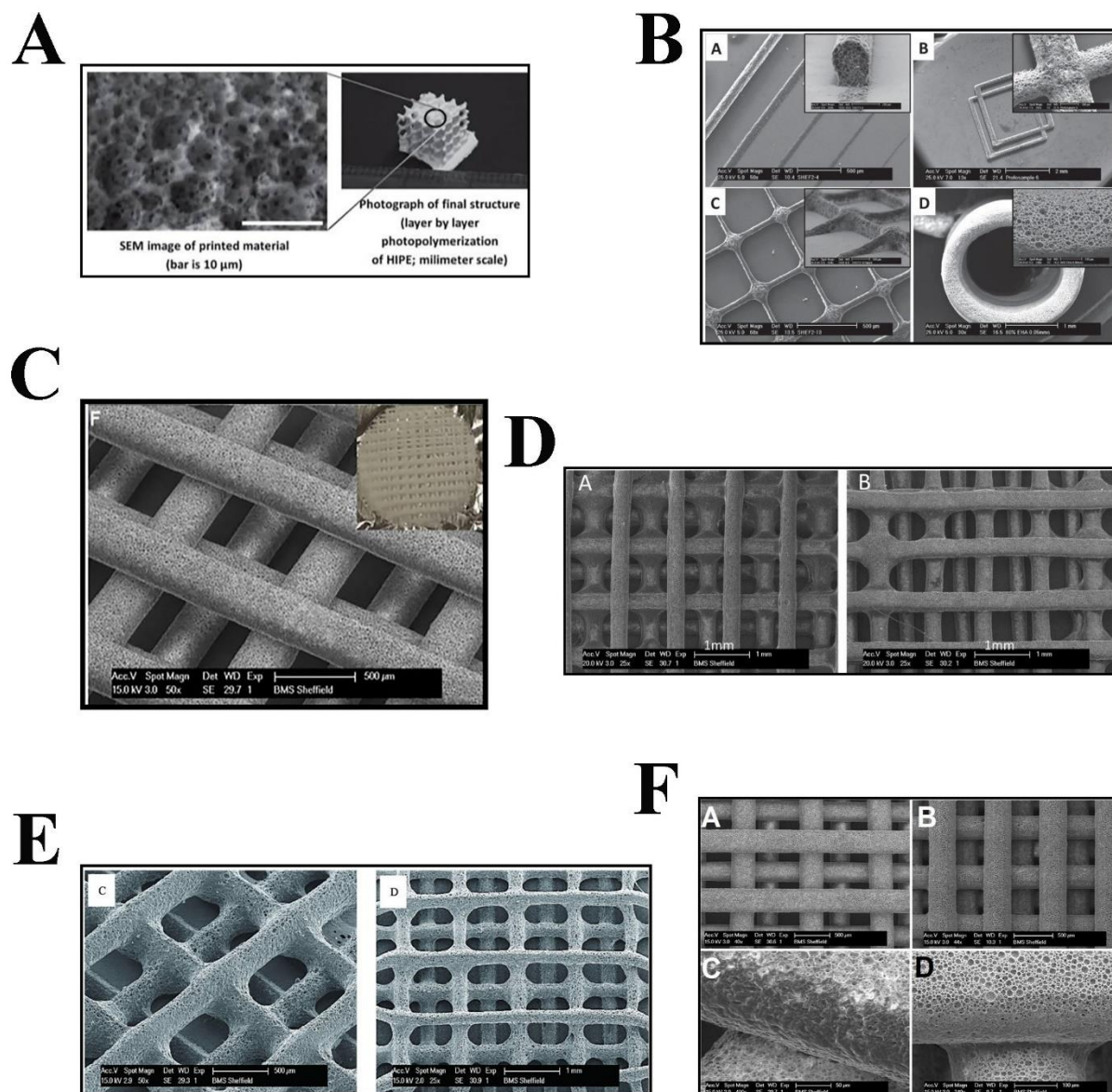
Figure 1.8. Examples of polyHIPE structures fabricated via light-based additive manufacturing. Additively manufactured polyHIPE structures for the first time **(A)** Adapted with permission from [64] Copyright 2013 WILEY-VCH Verlag GmbH & Co. KGaA and **(B)** Adapted with permission from [65] Copyright 2013 WILEY-VCH Verlag GmbH & Co. KGaA. Additively manufactured woodpile polyHIPE structures **(C)** Adapted with permission from [66] Copyright 2013, **(D)** Adapted with permission from [67] Copyright 2016 Elsevier, **(E)** Adapted from [68] Copyright 2016, and **(F)** Adapted from [69] Copyright 2018.

Interestingly, Sherborne et al. observed that challenges arise from the HIPEs' light-scattering nature, resulting in lower resolution and the formation of a closed porosity 'skin' layer on the surface (Figure 1.8F) [69]. Their study aimed to improve resolution and minimize skin formation using acrylate-based HIPEs with a UV light-absorber (UV-234 or Tinuvin®234) through light-based additive manufacturing. The results demonstrated that the addition of this absorber enhances resolution, reduces skin formation, and promotes cell proliferation. It was found that the incorporation of light absorbers holds potential for enhancing the resolution of PolyHIPE structures, making them appropriate materials for tissue engineering and cell culture applications.

Thanks to recent advancements in additive manufacturing, several commercially available 3D printer options have emerged, primarily relying on vat photopolymerization additive manufacturing. Notably, the same two research groups that pioneered the use of light-based AM setups to produce polyHIPEs achieved another milestone in 2023 by utilizing HIPEs on commercial light-based 3D printers simultaneously for the first time.

In the one of them, researchers developed a reactive thiol-ene high internal phase emulsion using specific monomers (1,6-hexanediol diacrylate and tris 2-(3-mercaptopropionyloxy)ethyl isocyanurate) for light-based additive manufacturing, resulting in highly porous and customizable polyHIPE materials (Figure 1.9A) [70]. The main objective of this formulation was to enable shorter exposure times and reduce the amount of photoinitiators, all while avoiding the use of harmful solvents for scalability. The addition of a selected thiol as a chain-transfer agent improved the flexibility of the acrylate-based system and reduced oxygen inhibition.
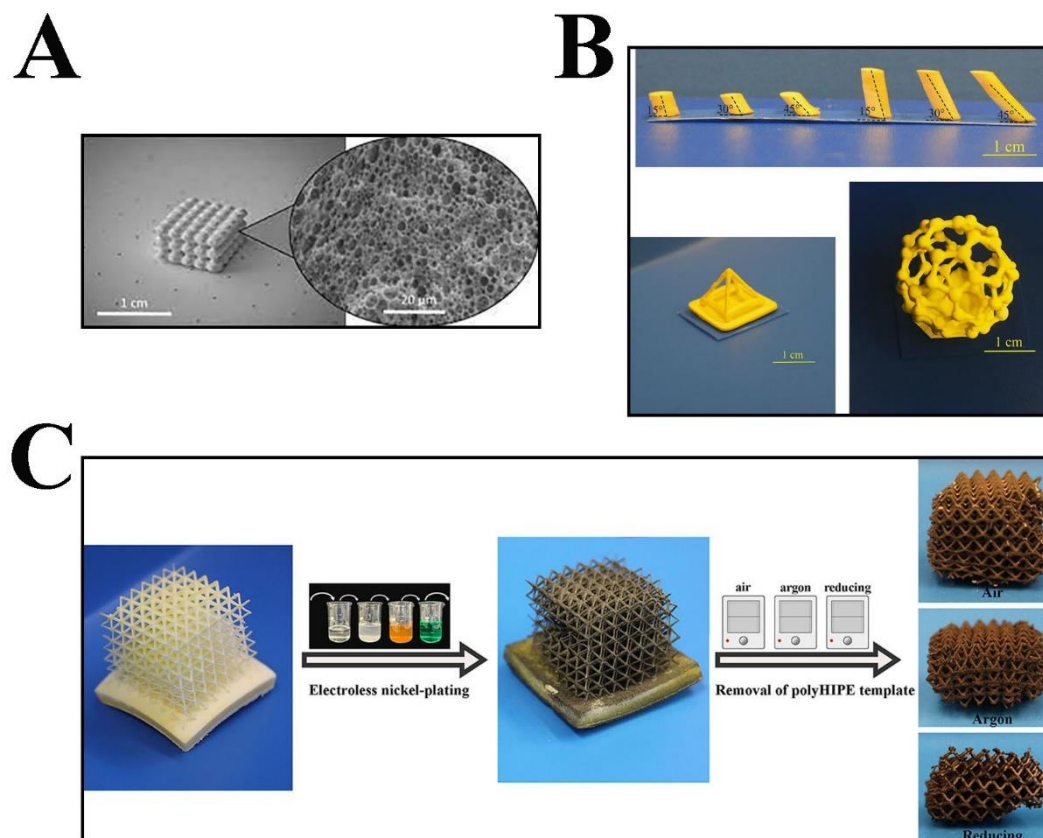
Figure 1.9. Examples of intricate polyHIPE structures fabricated via light-based additive manufacturing. **(A)** Adapted with permission from [70] Copyright 2023, Mary Ann Liebert, Inc., **(B)** Adapted from [71], and **(C)** Adapted from [72].

In the other study, Sengokmen Ozsoz et al. focused on optimizing acrylate-based HIPEs to use in commercial vat photopolymerization additive manufacturing, which employs a 405 nm LED source and DLP projector for high-resolution printing by using various amounts of beta-carotene (hydrophobic) and tartrazine (hydrophilic) as light absorbers (Figure 1.9B) [71]. The research emphasized a significant enhancement in improving the 3D printing resolution of polyHIPEs for fabricating intricate porous polymer structures. This was achieved by utilizing a blend of beta-carotene and tartrazine as light absorbers. Moreover, the study found that it is practical to fabricate intricate inherently porous polymers using commercial stereolithography, revealing a wide range of potential applications.

In addition, the same research group used their optimized HIPE resin to create inherently porous lattice structures utilizing a different commercial 3D printer that works on the same

principle (Figure 1.9C) [72]. Then, they focused on using these polyHIPEs as templates for electroless nickel plating to create ultra-porous metal-based lattice structures with a consistent wall thickness. The research aimed to optimize the electroless nickel plating process on polyHIPEs and investigate the effects of different atmospheres during the heating process to remove/carbonize the polyHIPE templates. The study demonstrated the potential of using intricate polyHIPE structures as templates to produce ultra-porous metal-based lattices for diverse applications.

Another additive manufacturing technique to fabricate polyHIPEs is extrusion-based AM. Up to 2016, the use of HIPEs as vat photopolymerization additive manufacturing resins were only investigated. Their use as extrusion-based additive manufacturing inks was studied by Sears et al. for the first time in 2016 (Figure 1.10A) [73]. The researchers used methacrylate monomers (DUDMA and PPGDMA) to prepare the emulsion ink. 3D-printed polyHIPE constructs were created using extrusion-based additive manufacturing. The utilized emulsions exhibited a tendency for shear-thinning behavior, allowing them to be deposited layer-by-layer. UV polymerization through the cure-on-dispense technique was applied to each layer, resulting in complex scaffolds featuring internal lattice structures and microscale porosity. The study emphasized the notable impact of viscosity and cure rate on the precision of the printing process. The same research group investigated the use of HIPEs for multi material printing to fabricate bone grafts by modifying their extrusion-based printer (Figure 1.10C) [74]. In the study, propylene fumarate dimethacrylate (PFDMA) was utilized as the material for creating bone grafts due to its compatibility with living tissues and its capability to facilitate bone growth. A novel technique was introduced to manufacture bone grafts, involving a combination of PFDMA polyHIPEs, known for their hierarchical porosity, and a robust outer layer made from either poly(ε-caprolactone) (PCL) or poly(lactic acid) (PLA). This innovative approach was made possible by a multi-mode printing setup that integrated paste extrusion and thermoplastic extrusion methods. This resulted in scaffolds with enhanced strength, thereby promoting the vitality and proliferation of cells.
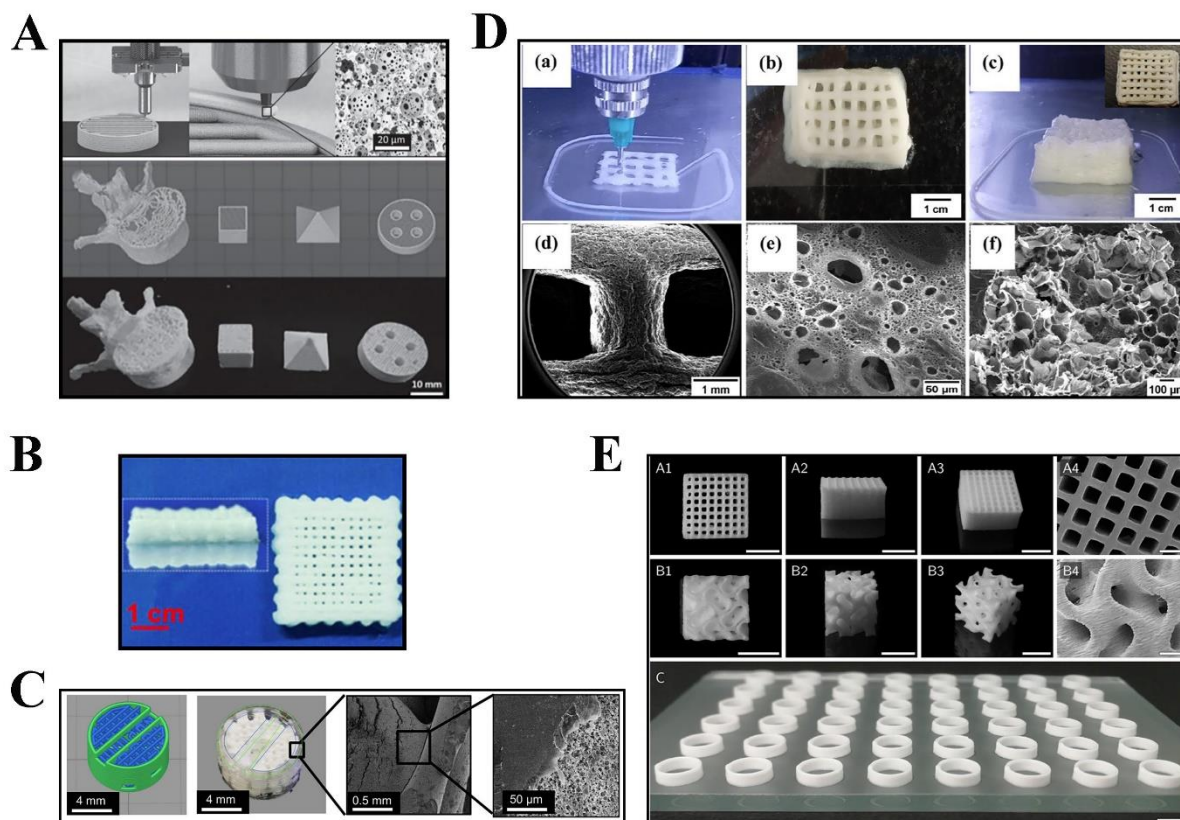
Figure 1.10. Examples of polyHIPE structures fabricated via extrusion-based additive manufacturing. **(A)** Adapted with permission from [73] 2016 WILEY-VCH Verlag GmbH & Co. KGaA, **(B)** Adapted with permission from [75] Copyright 2017 American Chemical Society, **(C)** Adapted with permission from [74] Copyright 2017 IOP Publishing Ltd, **(D)** Adapted with permission from [76] Copyright 2017 American Chemical Society, and **(E)** Adapted from [77] Copyright 2020.

Particle-stabilized HIPEs (Pickering HIPEs) can also be considered as potential printing resins/inks, just like surfactant-stabilized HIPEs.

Extrusion-based additive manufacturing was utilized by Yang et al. to create inherently porous cuboid scaffolds with a consistent macroporous structure from Pickering HIPEs for the first time (Figure 1.10B) [75]. These Pickering polyHIPE scaffolds, intended for drug delivery applications, consisted of a polymer matrix incorporating poly(L-lactic acid) (PLLA) and poly(ε-caprolactone) (PCL). The manufacturing process included the solvent evaporation of 3D printed Pickering HIPEs, which were stabilized with hydrophobically modified silica

nanoparticles (h-SiO2). Another study focused on the use of Pickering HIPEs in extrusion-based additive manufacturing was performed by Ghosh et al (Figure 1.10D) [76]. They employed poly(ε-caprolactone) (PCL)-based HIPEs stabilized with hydrophobically modified nanoclay particles to print woodpile structure for bone tissue engineering applications. The 3D-printed scaffold's characteristics including morphology, mechanical properties, biomineralization, drug release, and cell viability, were investigated. The findings suggest that these scaffolds hold promise for bone tissue engineering and controlled drug delivery, showcasing their versatility and potential for applications in bone implants and other fields.

HIPEs can also be used as printing materials for functional purposes. An interesting study demonstrating this was carried out by Wenger et al., focusing on using enzyme-laden hydrogel-filled acrylate-based HIPEs in extrusion-based additive manufacturing to fabricate biocatalytic reactors (Figure 1.10E) [77]. The prepared HIPEs as printing inks exhibited excellent printability for intricate structures, eliminating the requirement for support material. The research demonstrated the potential of HIPEs for enzyme-containing bioinks in 3D printing, thereby improving the efficiency of biocatalytic reactors.

In conclusion, over the past decade, surfactant-stabilized and particle-stabilized HIPEs have been employed as printing resins/inks in light-based and extrusion-based additive manufacturing to fabricate intricate inherently porous structures for a wide range of potential applications. The studies conducted so far have shown significant advancements in this field.

1.5. Applications of polyHIPEs

There is an increasing body of research on polyHIPE materials that show that polyHIPEs could be utilized in numerous potential applications. Indeed, the original patent from Unilever highlighted air filters, catalyst supports and insulation materials as applications [78].

The recent studies demonstrated that the most widely studied polyHIPE applications involve adsorption, absorption, and catalysis, followed by exploring polyHIPE scaffolds for tissue engineering and controlled release [60]. There is also recent interest in utilizing polyHIPEs for thermal and acoustic insulation purposes [60].

1.5.1. Adsorption and Absorption

The recent emphasis has broadened the application spectrum of hydrophobic polyHIPEs beyond their original use in absorption-related contexts, extending from the absorption of bodily fluids to the removal of pollutants from water [60]. Their hierarchical porous structure, facilitating fluid passage with minimal resistance and adaptable surface chemistry, implies promising opportunities for extensive industrial adoption and potential commercialization.

The domain of aqueous solution absorption remains a focal point, with both hydrophobic and hydrogel-infused polyHIPEs under scrutiny for their efficacy in absorbing water and various solutions [60]. Particularly noteworthy is the swelling-driven expansion of voids in hydrogel-incorporating polyHIPEs [79], leading to effective absorption of substantial amounts of water and synthetic urine (Figure 1.11A) [80]. Additionally, the utility of polyHIPEs in the extraction/purification of aqueous solutions [81], [82], [83], [84], [85], [86], [87], [88], [89] and the separation of water-oil mixtures [90], [91], [92] has been substantiated. These applications harness the inherent benefits of polyHIPEs, encompassing their high capacity for accommodating large quantities, consistent performance, and enduring stability. Investigations into gas adsorption and permeability underscore the potential of polyHIPEs in capturing and storing carbon dioxide [93], [94]. Refinements in surface chemistry and the inclusion of materials with substantial surface areas have bolstered the CO_2 adsorption capabilities [95]. Notably, the permeabilities of nitrogen gas exhibit variability influenced by factors like pore diameter interconnections and surface chemistry, potentially holding implications for gas permeability applications [96], [97].

1.5.2. Flow-Through Reactions and Catalysis

Various polyHIPEs have been investigated for facilitating flow-through reactions and catalytic supports. The effectiveness of polyHIPEs in supporting catalysts was conditional upon various factors, including the characteristics of the catalyst itself, its integration onto polyHIPE surfaces, and its availability [60]. For instance, a polyHIPE membrane containing Metal-Organic Frameworks (MOF) exhibited notable success in enabling Friedel−Crafts alkylation of *p*-xylene (Figure 1.11B) [98]. Hydrophobic polyHIPEs were employed as stationary phases in chromatography [99], catalyst supports for reduction reactions [100], and coatings for electrochromatography separation columns [101]. Additionally, polyHIPE catalysts featuring

acid−base sites exhibited promise in catalyzing the conversion of cellulose [102], while polyHIPEs incorporating catalytic gold nanoparticles effectively facilitated the reduction of 4-nitrophenol [103]. These applications collectively underscore the remarkable adaptability and efficiency of polyHIPEs across a wide spectrum of catalytic processes.

1.5.3. Release and Encapsulation

Applications related to absorption and adsorption frequently require the recovery of sorbates to enable the reuse of sorbents [60]. In contrast, the utilization of polyHIPEs in controlled release entails the integration of substances intended for release within the voids.

Noteworthy findings from release behavior investigations emphasize the profound influence of the porous structure, exemplified by the liberation of water-soluble dyes from hydrogel-incorporating polyHIPEs (Figure 1.11C) [104], [105]. The encapsulation of liquids is pivotal in sectors like pharmaceuticals and cosmetics [60]. Some polyHIPEs possess closed-cell configurations, enabling straightforward removal of the internal phase [59], [106]. Recently, elastomeric polyHIPEs characterized by their closed-cell architecture have been engineered, showcasing impressive water retention and resistance to compression [59]. These advances have found applications in areas such as controlled-release fertilizer and the storage of thermal energy.
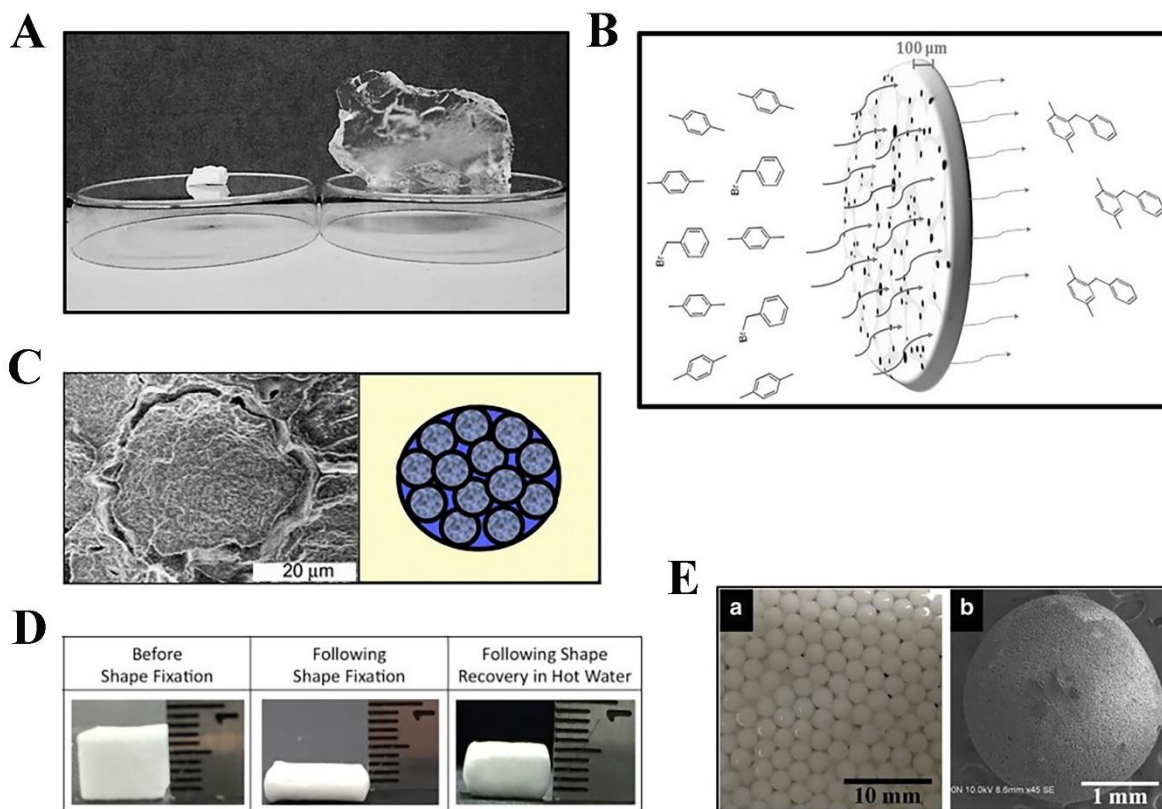
Figure 1.11. Examples of the applications of polyHIPEs. **(A)** Absorption, Adapted with permission from [80] Copyright 2016 WILEY-VCH Verlag GmbH & Co. KGaA, **(B)** Catalysis, Adapted with permission from [98] Copyright 2016 WILEY-VCH Verlag GmbH & Co. KGaA, **(C)** Release, Adapted with permission from [109] Copyright 2010 Elsevier Ltd, **(D)** Shape memory, Adapted with permission from [107] Copyright 2015 Elsevier Ltd, **(E)** Beads, Adapted with permission from [108] Copyright 2015, Springer Science Business Media Dordrecht.

1.5.4. Tissue Engineering Scaffolds

Macroporous structures find significant relevance in diverse biomedical applications like 3D cell culture, tissue engineering, and controlled release [60]. However, their adoption in the biomedical sector necessitates meeting stringent criteria for material purity and biocompatibility. A crucial challenge lies in eliminating residual external phase constituents while preserving the porous structure. Tissue engineering utilizing polyHIPEs has witnessed progressive evolution, particularly in the field of 3D cell culture scaffolds.

Noteworthy advancements include polyesters [109], [110], [111], [112], [113], [114], polymethacrylate hydrogels [115], polyacrylates [67], and polyacrylamide [116], [117] characterized by biocompatibility and cytocompatibility. Emerging research avenues involve integrating bioactive nanoparticles, such as hydroxyapatite, to enhance the mechanical attributes and bioactivity of polyHIPEs [67], [109], [110], [111]. Innovations in advanced polymer chemistries and additive manufacturing techniques hold substantial promise for fabricating intricate shapes tailored to tissue engineering needs [64], [67], [73]. Another interesting point is the development of injectable HIPEs that undergo in-body reactions to yield polyHIPEs, necessitating biocompatible components and physiological temperature responsiveness [109], [114], [118], [119]. The outlook for realizing commercial applications of polyHIPEs in tissue engineering remains promising.

1.5.5. Shape Memory Materials

Shape memory polymers find extensive application, particularly in the biomedical field, offering the demand for minimally invasive implantation [120]. These polymers commonly incorporate a reversible transition element to uphold temporary configurations and a restoration element for reverting to their original forms. The reversible transition can be predicated on temperature parameters like glass transition (T_g) or melting point (T_m), while the restoration mechanism may entail cross-linking or higher transition temperatures. The growing repertoire of intricate macromolecular structures within polyHIPEs presents an avenue for innovating novel shape memory systems. Illustratively, shape memory polyHIPEs fabricated from (meth)acrylates featuring crystallizable aliphatic side chains adopt temporary shapes at elevated temperatures, regaining their original forms through elastomeric networks [121], [122]. The emergence of shape memory hydrogel-filled polyHIPEs exhibiting swift recovery kinetics, particularly when immersed in heated water, underscores the potential in this domain (Figure 1.11D) [107].

1.5.6. Membranes and Beads

PolyHIPEs provide the benefit of facilely fabricating monolithic forms, aided by methods like doctor blading tailored for membrane uses [123]. Notably, polyHIPE beads incorporating

photocatalytic TiO_2 nanoparticles exhibited robust efficacy in wastewater treatment, sustaining performance throughout successive cycles (Figure 1.11E) [108].

1.5.7. Porous Carbons and Porous Inorganics

The primary focus of porous carbons and inorganic substances derived from polyHIPEs has been on adsorption applications, leveraging the extensive surface areas resulting from micro- and meso-porosity [60]. Carbons derived from polyHIPE precursors, such as styrene, DVB, and VBC, offer hierarchical porosity that facilitates efficient substance transport [124]. Processes like carbonization, hyper-cross-linking, porogen removal, and activation contribute to their high surface areas and conductivity. Porous carbons derived from polyHIPEs have demonstrated efficacy in dye adsorption [125], vapor adsorption [126], and supercapacitor electrodes [127]. Moreover, porous Si(HIPE)s exhibited potential for biotechnological uses, particularly in bacterial colonization applications [128].

1.5.8. The use of PolyHIPEs as templates to fabricate intricate ultra-porous metallic/carbon/ceramic structures

With the help of the latest developments in the use of HIPEs in additive manufacturing (AM), polyHIPEs have emerged as promising materials for fabricating intricate, ultra-porous structures made of metals, carbon, or ceramics. This is a relatively new and open-ended field with vast potential for innovative applications and sustainability.

In this context, the use of HIPEs as printing resins in this thesis has been thoroughly investigated and optimized to create inherently porous, intricate structures. Furthermore, their potential in fabricating complex, ultra-porous structures combining metals and carbon has also been explored.

1.6. Aim and Objectives

The aim of this PhD thesis is to explore and optimize the use of High Internal Phase Emulsions (HIPEs) as vat photopolymerization additive manufacturing (AM) resins to create intricate

lightweight porous materials and to investigate their potential to fabricate inherently porous metal-based and carbon structures. This is achieved by:

1. Investigating the incorporation of light absorbers, hydrophobic beta-carotene and hydrophilic tartrazine molecules, into HIPE-based resin to enhance printing resolution in commercial vat photopolymerization additive manufacturing.

2. Assessing the compatibility of HIPE-based resin with commercial 3D printers based on vat photopolymerization, ensuring stability throughout the printing process and achieving the porous polyHIPE structure with open surface porosity.

3. Optimizing the electroless nickel plating process on polyHIPEs and investigating the effects of different atmospheres during the heating process to remove the polyHIPE template from metallized 3D-printed polyHIPE lattice structures.

4. Investigating the pyrolysis of 80%, 85%, and 87.5% porous polyHIPE lattices at various temperatures to fabricate porous carbon structures and evaluating their mechanical properties.

CHAPTER 2

Optimization of a High Internal Phase Emulsion (HIPE) based resin for use in commercial vat photopolymerization additive manufacturing
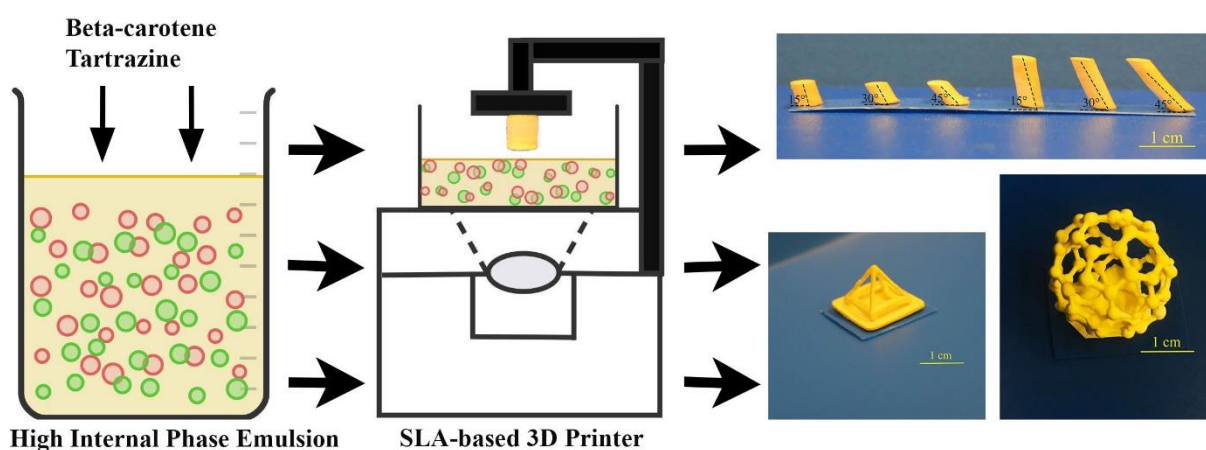
Abstract

High internal phase emulsions (HIPEs) are potential stereolithography-based resins for producing innovative lightweight porous materials; however, the use of these resins has only been shown in bespoke stereolithography setups. These studies indicated that HIPEs tend to scatter the light during structuring via stereolithography, and can produce poorly defined, and low-resolution structures, but the inclusion of light absorbers can drastically increase the printing resolution. In this study, we focused on the inclusion of biocompatible light absorbers within the resin and the compatibility of those resins with a commercial vat photopolymerization additive manufacturing (or stereolithography) setup. A surfactant (hypermer) stabilized water-in-oil emulsion based on 2-ethylhexyl-acrylate and isobornyl-

acrylate was used. For the light absorbers, both hydrophobic (beta-carotene) and hydrophilic (tartrazine) molecules were used, which dissolve in the organic phase and aqueous phase, respectively. It was found that using a combination of both beta-carotene and tartrazine provided the best stereolithography-based 3D printing resolution. Additionally, the emulsion was stable for the duration of the printing process and showed a porous polyHIPE structure with open surface porosity. The formulation of these HIPE-based resins permits them to be used in a wide range of applications since complex structures could be fabricated from HIPEs.

Keywords: PolyHIPE, Vat photopolymerization, Stereolithography, 3D printing, Light absorber

2.1. Introduction

From the 1990s onwards, there has been an increased interest in the manufacture of porous polymer structures because of their flexibility of design, and relatively easy and low-cost manufacture [49], [50], [51], [52], [53], [129]. Primarily, research in porous polymers focused on producing polymers with tunable physical properties, well-defined tunable porosities from micrometer to millimeter size and high surface areas. This led to a variety of potential applications, for example, filter materials, catalyst support, or scaffold materials in tissue engineering and 3D cell culture [49], [54]. Porous polymers can also be used as templates for the manufacturing of porous metals, ceramics, carbons, and composites [49].

One versatile technique to produce porous polymers is emulsion templating where an emulsion of a pre-polymer or polymer solution continuous phase is combined with water as dispersed phase. During the process the polymer sets, and the water is removed to obtain the remaining polymer network template formed by the emulsion. When using large amounts of internal phase (over 74% of the total volume) and a suitable emulsifying surfactant, this process produces High Internal Phase Emulsions (HIPEs) [49], [55], [56], [130]. These are templates to produce highly porous polymer structures (polyHIPEs) with potentially interconnected porosity [49]. PolyHIPEs can be shaped via traditional manufacturing techniques such as

casting (molding) to make structures with low design complexity and flexibility, where post-processing can be applied to create complex structures [73], [131]. An interesting novel route to shape polyHIPEs is via combining emulsion templating with additive manufacturing. This allows single-step manufacturing of inherently porous and lightweight complex structures with little to no post-processing [65], [66], [69].

Currently, additive manufacturing is emerging as an industrial manufacturing technique to fabricate three-dimensional objects directly from computer-aided design (CAD) files through layer-by-layer manufacturing, originally invented in the 1980s [1], [2]. Additive manufacturing is a general term for a group of technologies, also known by the public as 3D printing. Additive manufacturing technologies are mainly divided into seven categories according to the terminology set out by ISO/ASTM 52900: 2015 [2], [7]. These categories are binder jetting, directed energy deposition, material jetting, powder bed fusion, sheet lamination, material extrusion, and vat photopolymerization. Material extrusion (fused deposition modelling) and vat photopolymerization (stereolithography) are used for the additive manufacturing of polymer materials and have both been used to build porous polyHIPE 3D structures [65], [66], [67], [69], [74]. In these studies, bespoke emulsions were prepared by mixing water with suitable monomers, surfactants, crosslinkers, and photoinitiators and were printed on experimental in-house setups. However, to our knowledge, their printability in commercial stereolithography-based 3D printers has not been demonstrated.

Even though additive manufacturing allows the manufacturing of complex polyHIPE structures, HIPE-based resins tend to scatter light during structuring via stereolithography [69]. Therefore, this can cause the production of poorly defined, low-resolution structures. Improving the resolution by using light absorbers has previously been reported by Choi and Wicker in standard non-porous stereolithography resins [132], and by Sherborne et al. in emulsion-based resins [69]. Sherborne et al. used Tinuvin 234 as a light absorber to reduce the resolution in a house-built stereolithography set-up to 200 µm for HIPE-based inks by reducing the light scattering arising in the focal point. Additionally, it was observed that the surface of the structures without light absorbers was non-porous, which was attributed to surface skin from the poorly cured polymer in the scattering region. The surface skin reduced the functionality of the structures, especially in applications that depend on surface porosity (e.g., cell culture scaffolds).

In this study, the use of high internal phase emulsions as potential 3D printing resins for producing inherently porous structures with a commercial vat photopolymerization-based 3D printer (Kudo 3D Titan2 HR) was investigated. This set-up integrates a 405 nm LED source and a DLP projector to project high-resolution images (up to 25 µm) on a 10.2 cm × 7.4 cm build platform [133]. It illuminates the sample from the bottom through a transparent base and a thin layer of uncured resin on the z-translation platform (bottom-up setup). In this bottom-up setup, there are 3 steps: a curing step, a pull-off step where the z-platform translates to pull the reacted resin from the transparent base, and a third step where the build platform moves back to produce the next layer. This convoluted sequence of steps for each layer could have significant consequences for emulsion stability and porosity, and this has been studied in detail in this publication.

We aimed to investigate the effects of two light absorbers on mainly the printing resolution and porous microstructure. Beta-carotene and tartrazine were used, which are biocompatible light absorbers, as highlighted in previous literature [134]. Beta-carotene is a hydrophobic compound, while tartrazine is hydrophilic. Accordingly, beta-carotene resides in the organic phase, whereas tartrazine is retained in the aqueous phase. This study explores the overall effects of hydrophobic and hydrophilic light absorbers in these emulsions and determines whether employing both together has any advantages over using each one separately.

2.2. Experimental

2.2.1. Materials

2-ethylhexyl acrylate (EHA), isobornyl acrylate (IBOA), trimethylolpropane triacrylate (TMPTA), 2 different forms of photoinitiators; diphenyl (2,4,6- trimethyl benzoyl)-phosphine oxide (in crystal form) and 2-hydroxy-2-methyl propiophenone (in liquid form), beta-carotene (synthetic, ≥93% (UV), powder), and tartrazine (dye content ≥85 %) were all purchased from Sigma Aldrich. The surfactant Hypermer B246-SO-M was kindly donated by Croda.

2.2.2. Preparation of High Internal Phase Emulsions

37.30 wt% 2-ethylhexyl acrylate (EHA), 37.30 wt% isobornyl acrylate (IBOA), 16.40 wt% trimethylolpropane triacrylate (TMPTA) (crosslinker), and 9.00 wt% Hypermer B246-SO-M (surfactant) were mixed to form the continuous organic phase. This mixture was heated using a heat gun until the surfactant was dissolved at 50°C. Afterwards, photoinitiators were added to the continuous phase at 2.5 wt% in crystal form and at 2.5 wt% in liquid form. The solution was heated to 40°C for 5 minutes to dissolve the photoinitiator, which is in crystal form.

HIPEs containing beta-carotene and tartrazine were fabricated by adding both to the continuous phase before the addition of the photoinitiator. Beta-carotene was added from 0.1 to 1.0 wt% (of the continuous phase), and tartrazine was added from 0.1 to 0.4 wt% (of the continuous phase) in increments of 0.1 wt% (Table 2.1).

Finally, 80 vol.% of distilled water, dH2O, (the internal phase) was added to the continuous phase to form an emulsion. The water was added dropwise while stirring the emulsion at 300 rpm (SciQuip-Pro 40 stirrer).

Table 2. 1. EHA, IBOA, TMPTA, hypermer, beta-carotene, and tartrazine ratio (wt%)

Samples	Organic Phase				Light absorbers	
	EHA (wt %)	IBOA (wt %)	TMPTA (wt %)	Hypermer (wt %)	Beta-carotene[a] (wt %)	Tartrazine[a] (wt %)
Pure	37.30	37.30	16.40	9.00	-	-
Beta-carotene	37.30	37.30	16.40	9.00	0.10 to 1.00	-
Tartrazine	37.30	37.30	16.40	9.00	-	0.10 to 0.40
Blend	37.30	37.30	16.40	9.00	0.40	1.00

[a]Beta-carotene and tartrazine concentration with respect to the organic phase

2.2.3. 3D Printing of High Internal Phase Emulsions

PolyHIPE structures were 3D printed using a commercially available, desktop 3D printer (Kudo 3D Titan2 HR). The 3D printer employed the vat polymerization technique and combined stereolithography (SLA) and digital light projection (DLP) methods using a 405 nm light source.

Computer-aided design (CAD) was used to produce the structures for 3D printing (SolidWorks 2018). These were formatted as .stl files and then prepared for 3D printing and sliced using Creation workshop (version 1.0.0.75).

2.2.4. 5×5 mm cylinders for the optimization of the light absorber content

Cylinder samples, 5 mm diameter × 5 mm height, were 3D printed and used to optimize the amounts of light absorbers in the emulsion. These cylinders contained 233 layers with a base and supports after slicing (Figure A2). Initially, the HIPE containing no beta-carotene or tartrazine, further denoted as "pure", was used to 3D print the polyHIPE cylinders. Printing parameters (exposure time, lifting speed, lifting height, etc.) were varied to achieve the best 3D printing performance (the final parameters and overall print time are listed in Table A1 and Table A18, respectively). After determining the most suitable 3D printing parameters for the pure HIPE, HIPEs including beta-carotene and tartrazine at varying concentrations were used to 3D print the polyHIPE cylinder structures. Additionally, the 3D printing parameters were modified slightly to achieve the best results when including the light absorbers (Tables A2-A4,A18). Once 3D printing was completed, the cylinders were washed with acetone to remove non-polymerized HIPE and then air-dried.

2.2.5. Investigation of the 3D printing resolution

Various calibration objects were 3D printed using the HIPEs to determine the resolution that could be achieved.

A calibration object including 5 mm-high posts of 3 mm, 2 mm, 1 mm, and 0.5 mm diameters was 3D printed from the pure HIPE and then from HIPEs that contained the optimized amounts of beta-carotene, tartrazine, and a blend (0.4% beta-carotene and 0.1% tartrazine) (Figure A5 and Tables A12-A15, A18).

Additionally, cylinders, 5 mm diameter $\times$ 5 mm and 10 mm height, having 15°, 30°, and 45° inclines were also 3D printed from the pure HIPE and the HIPE containing the optimized amounts of beta-carotene, tartrazine, and a blend of them (Figures A3, A4 and Tables A5-A11, A18).

2.2.6. Pyramid and Buckyball structures

3D designs of pyramid and buckyball structures were obtained from thingiverse.com [135], [136]. These 3D-designed structures were fabricated from HIPEs containing a blend of beta-carotene and tartrazine to demonstrate the usability of HIPEs as 3D printing materials for producing complex geometric structures (Figures A6, A7 and Tables A16-A18).

2.3. Characterization of HIPEs and polyHIPEs

2.3.1. UV/Vis Spectrometer

A Jenway 6305 spectrophotometer was used to measure the light absorbance of optimized amounts of light absorbers at 405 nm using 10 mm disposable UV cuvettes. Beta-carotene was dissolved in the organic phase (hydrophobic compound), while tartrazine was dissolved in the aqueous phase (hydrophilic compound). Absorbances were measured against blank samples of the organic and aqueous phases for beta-carotene and tartrazine, respectively.

2.3.2. Scanning Electron Microscopy

A Tescan Vega3 Scanning Electron Microscopy (SEM) was used to image the cross-section and outer surface of 3D-printed polyHIPE samples. Before SEM imaging, samples were gold coated to provide conductivity (Edwards S150B sputter coater). ImageJ was used for measuring pore diameters, implementing a method that involved initially adding 50 grids to the image. This process facilitated precise quantification of pore sizes within the image. Subsequently, 100 pores were measured for each sample, with 2 pores selected from each grid to determine an average. A statistical correction factor of $2/\sqrt{3}$ was then applied to the results to account for the non-equatorial location of the pore diameter measurements [137], [138].

2.3.3. Helium Pycnometry

The porosity of the polyHIPEs was determined using helium pycnometry. PolyHIPE cylinders, 5 mm diameter × 5 mm height, were 3D printed from pure HIPE and from HIPEs that contained the optimized amounts of beta-carotene, tartrazine, and the blend (0.4% beta-carotene and 0.1% tartrazine). These cylinders were examined using an Accupyc 1340 Gas Pycnometer to calculate their porosity. The device determined the density and volume (V_{pyc}) of the samples. Equation 2.1 was used to calculate % porosity. V_{bulk} is the volume of the bulk cylinder sample.

$$\% \, porosity = \left(1 - \frac{Vpyc}{Vbulk} \right) \times 100 \tag{2.1}$$

Additionally, equivalent polyHIPE cylinders were also produced from UV-cured HIPEs, polymerized using a UV belt curer (GEW Mini Laboratory, GEW engineering UV) with a 100 W cm^{-2} UV bulb. Cylinders were cut from UV-cured polyHIPE samples using a 5 mm diameter hollow punch. UV-cured polyHIPE cylinders were produced from freshly prepared HIPEs and leftover HIPEs (which remained in the printing tank after 3D printing) to demonstrate the effect of the two-step up-and-down movement of the printing platform on porosity.

2.3.4. Statistical Analysis

All statistical analysis was undertaken in GraphPad Prism (version 8.4.3). One-way ANOVA with Tukey's multiple comparison analysis was applied to assess significant differences. Differences were considered significant when $p < 0.0001$. All experiments were repeated three times, and the number of replicates (n) is mentioned in the figure legend.

2.4. Results

2.4.1. UV-Vis Spectrometer

We aimed to formulate a resin that had a similar amount of light absorbance in the organic phase compared to the aqueous phase and to subsequently fine-tune the light absorbance within

the respective phases via changing the concentration of the light absorber (beta-carotene and tartrazine) and observe any changes in shape fidelity and internal structure. To achieve this, the optical absorption of the two different absorbers beta-carotene and tartrazine was measured, and their absorptions were recorded at 405 nm for 8 different concentrations, between 2.5 µM and 20 µM with 2.5 µM intervals. From the gradient of these plots, (i.e., the experimental extinction coefficients at 405 nm) it can be calculated that tartrazine is in general 6.23× more absorbent at 405 nm than beta-carotene at the same molar concentration.
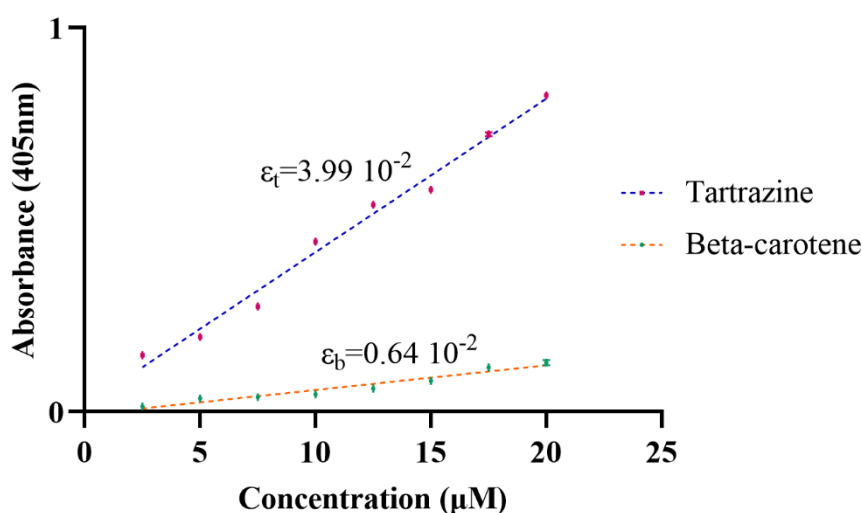
Figure 2.1. Extinction coefficient graph of beta carotene and tartrazine samples at 405 nm (n=3)

Important to note is that both beta-carotene and tartrazine are natural products, which can have batch-to-batch variation (due to impurities) in their absorbance but also time-dependent variation, likely because of oxidation. For this reason, the extinction coefficient is regularly checked (Figure 2.1) and the concentrations of the light absorbers are adjusted accordingly to achieve consistent results. Furthermore, the molecular structures and absorbance spectra of beta-carotene and tartrazine can be checked in Figure A1.

2.4.2. Optimization of light absorber content and examination of 3D Printing resolution

Cylinder samples which were fabricated with different amounts of light absorbers, the diameter and height values, and the aspect ratio graph of 3D printed 5×5 mm cylinders were presented in Figure 2.2.

The important figures to analyze were their diameter, height, and aspect ratio values, which are summarized in Figure 2.2. The shape fidelity of the print will likely be influenced by a few distinct and competing processes. As aforementioned, emulsion-based resins can scatter the light, which will translate into a larger object size both in the transversal and lateral directions of the printed stubs. The printed porous objects also exhibited shrinkage during the drying process after printing (Figure A8 and Table A19), which is a result of the water removal. Higher shrinkage will likely occur with under-cured objects because of lower cross-linking density. The results are highlighted in Figure 2.2. The results indicate that the inclusion of both beta-carotene and tartrazine influences the height, width, and aspect ratio of the printed structures. The printed cylinders included 1 mm spacer struts to easily disconnect the cylinder from the base (Figure A2). This allows for over-curing to occur in the z-direction, and this is observed in the cylinder cured without any light absorber (pure) (Figure A8). The aspect ratio varies non-linearly with increasing beta-carotene, indicating that the shape fidelity depends on a few competing factors as aforementioned. For both light absorbers, there was a maximum amount that could be added to the emulsion before print properties decreased. 1.0 wt % beta-carotene sample did not result in a successful print for beta-carotene, while 0.4 wt % of tartrazine addition resulted in a deteriorating structure.

Table 2.2. Diameter (mm), height (mm), and aspect ratio values

Samples	Diameter (mm)	Height (mm)	Aspect Ratio
Pure	4.73 ± 0.11	4.95 ± 0.02	0.96 ± 0.02
0.2 B	4.90 ± 0.04	4.84 ± 0.10	1.01 ± 0.01
0.4 B	4.89 ± 0.04	4.93 ± 0.05	0.99 ± 0.00

0.6 B	4.73 ± 0.06	4.94 ± 0.06	0.96 ± 0.02
0.8 B	4.53 ± 0.08	4.37 ± 0.01	1.04 ± 0.02
0.1 T	4.54 ± 0.04	4.68 ± 0.11	0.97 ± 0.03
0.2 T	4.20 ± 0.02	4.50 ± 0.19	0.93 ± 0.04
Blend	4.53 ± 0.09	4.60 ± 0.05	0.99 ± 0.03
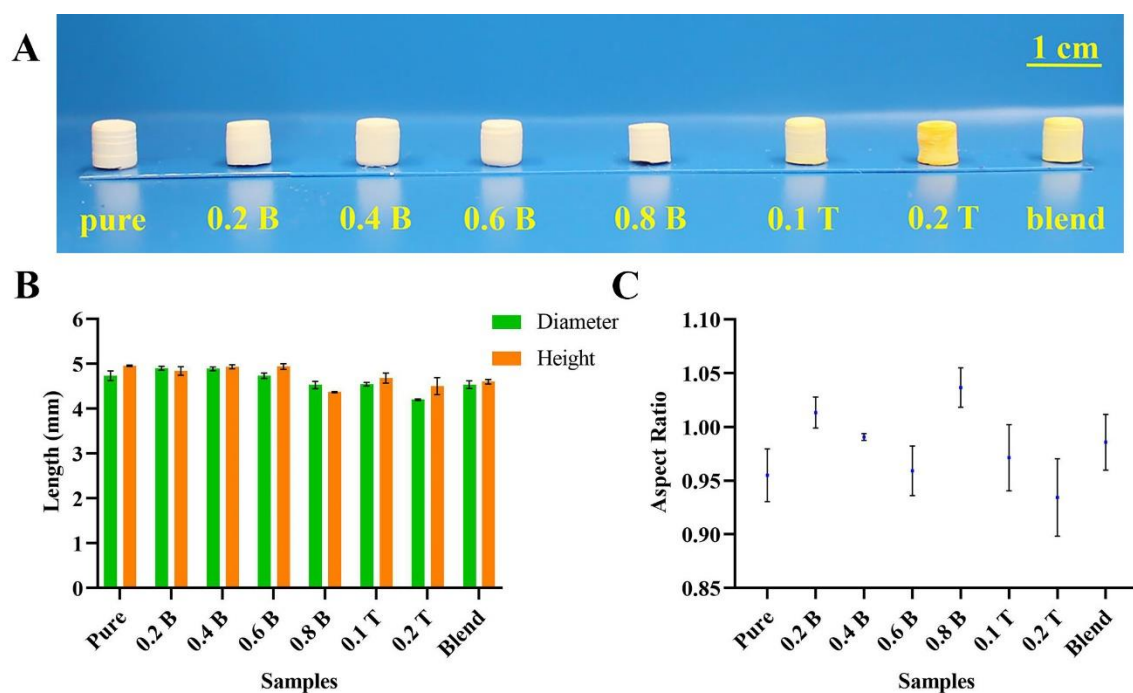
Figure 2.2. (**A**) 3D printed 5×5 mm cylinders. (**B**) Diameter and height values of the 3D printed 5×5 mm cylinders. (**C**) The aspect ratio of the 3D printed 5×5 mm cylinders. (n=3)

Overall, the 0.4 % beta-carotene allowed the manufacturing of structures that were closest to 3D design. The cylinder samples containing 0.4% beta-carotene have a diameter of 4.89 ± 0.04 mm and a height of 4.93 ± 0.05 mm (n=3) while the 3D model of the cylinder is 5×5 mm height. Also, the object with the aspect ratio closest to 1 is the 0.4 % beta-carotene structure. The 0.2 % beta-carotene structure is near second best with an aspect ratio was 1.01 ± 0.01 and diameter

of 4.90 ± 0.04 mm and a height of 4.84 ± 0.10 mm. We also investigated the addition of tartrazine to the aqueous phase of the HIPE. In this series, the 0.1% tartrazine provided the best results (aspect ratio is 0.97 ± 0.03). Additionally, the combination of both was investigated by combining the best ones from each category. Interestingly, the blend samples exhibited shape fidelity with an aspect ratio of 0.99 ± 0.03 even though both their diameter (4.53 ± 0.09 mm) and height (4.60 ± 0.05 mm) were lower than the pure and beta-carotene samples. The observed shrinkage might indicate a lower cross-linking density in the polymer phase due to absorbance and is mainly observed in the emulsions that include tartrazine (Table 2.2).
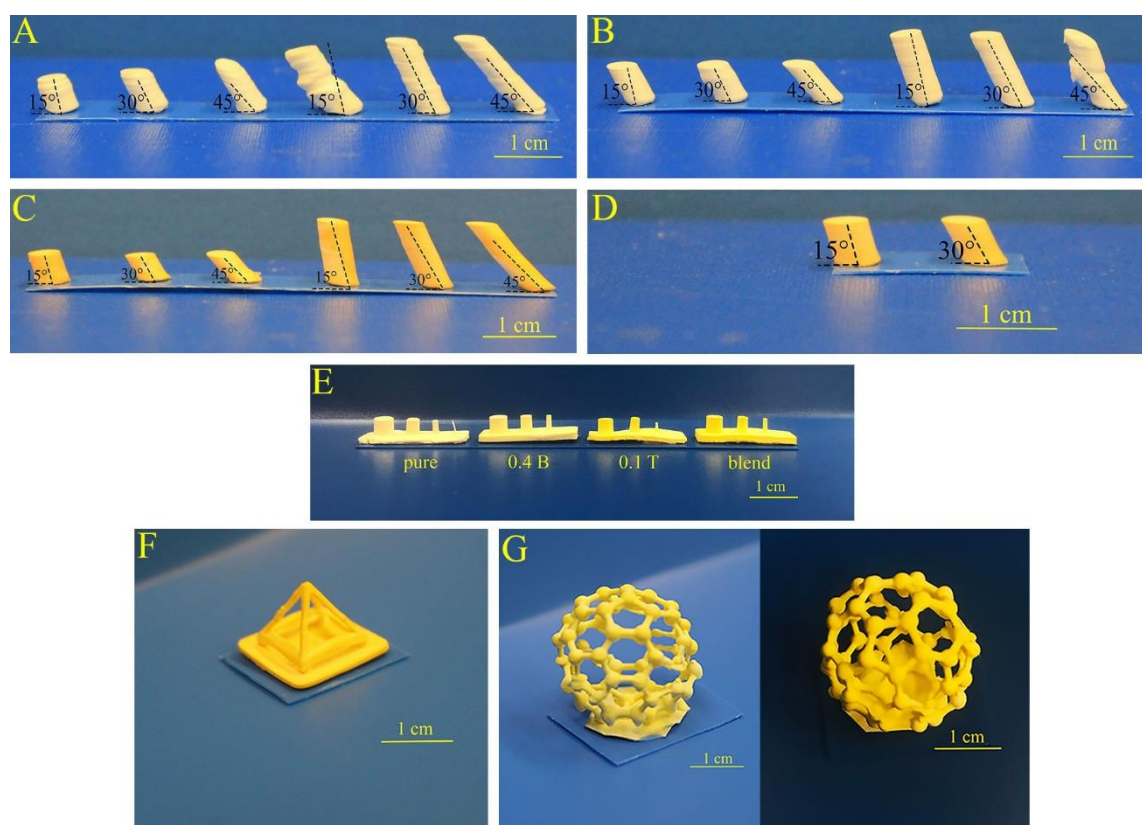
Figure 2.3. (A) 3D printed cylinders having 5 mm and 10 mm height, and 15°, 30°, and 45° inclines from pure HIPE. **(B)** 3D printed cylinders having 5 mm and 10 mm height, and 15°, 30°, and 45° inclines from HIPE that contained 0.4 % beta-carotene. **(C)** 3D printed cylinders having 5 mm and 10 mm height, and 15°, 30°, and 45° inclines from HIPE that contained blend (0.4 % beta-carotene and 0.1 % tartrazine). **(D)** 3D printed cylinders having 5 mm height, and 15° and 30° inclines from HIPE that contained 0.1 % tartrazine. **(E)** Calibration object

including 5 mm high posts of 3 mm, 2 mm, 1 mm, and 0.5 mm diameters which was 3D printed from pure HIPE and HIPEs that contained 0.4 % beta-carotene, 0.1 % tartrazine, and blend (0.4 % beta-carotene and 0.1 % tartrazine), respectively. **(F)** 3D printed pyramid structure from HIPE that contained blend (0.4 % beta-carotene and 0.1 % tartrazine). **(G)** 3D printed buckyball structure from HIPE that contained blend (0.4 % beta-carotene and 0.1 % tartrazine).

A second test was how well overhangs are recreated in polyHIPE 3D printing. For this purpose, various cylinder structures having 5 mm and 10 mm height, and 15°, 30°, and 45° inclines were printed and presented in Figure 2.3. As a result, although these cylinder structures were created from pure, beta-carotene, and blend categories, only the cylinders having 5 mm height and 15° and 30° inclines were obtained in the tartrazine category.

The 3D-printed structures were examined in terms of resolution, and the best resolution was obtained from the blend light absorber category. All 6 cylinders were 3D printed without any distortion and over-curing in the structure. On the other hand, pure polyHIPE cylinders presented the least optimal results due to their distorted, over-cured structure with a prominent layered appearance arising from the printing process. Even though the cylinders containing 0.4 % beta-carotene showed similarity with pure polyHIPE cylinders, they presented more uniform structures except for the sample having 10 mm height and 45° incline. However, the layered structure caused by printing was noticeable, though to a lesser extent compared to the pure cylinders. Unlike pure and 0.4 % beta-carotene, the cylinders that contained 0.4 % beta-carotene and the blend did not show any distorted or layered structure. Finally, only 2 cylinders having 5 mm height and 15° and 45° incline were 3D printed from the HIPEs containing 0.1 % tartrazine although they were as uniform as the cylinders containing blend. As the height and incline of the cylinders increased, the attachment of the printed objects to the printing platform decreased, and the cylinders dropped from the printing platform during the 3D printing process. For this reason, the other cylinders failed.

Figure 2.3E presents a series of 3D printed calibration objects, including 5 mm high posts of 3 mm, 2 mm, 1 mm, and 0.5 mm diameters. The 0.5 mm width post could only be seen in the calibration object of pure polyHIPE, and it could not be printed with the others. This is likely due to the tendency of scattering-induced over-curing in pure HIPE. Even though the over-curing of HIPEs is a problem when fabricating more complex designs, it may be advantageous

when fabricating the fine details. Except for the 0.5 mm post, the posts could be 3D printed from HIPEs containing 0.4% beta-carotene and the blend, while the 1 mm width post was incomplete in 0.1 % tartrazine. The pyramid structure containing inclined and thin edges (1.10 mm in the design file) and the buckyball structure including thin small spheroids (2 mm in the design file) connected by thin lines (0.90 mm in the design file) were 3D printed as proof of the usability of HIPEs to fabricate more complicated structures (Figure 2.3F-G).

2.4.3. Comparison of the porous structures of the polyHIPEs containing different amounts of light absorbers

The layered microstructure caused by the 3D printing process of the polyHIPEs is presented in Figure 2.4A-D. Layers and the interconnectivity between layers could be seen clearly. 6 layers from each category were measured, and the layer thicknesses were 30.35 ± 0.55 µm, 29.65 ± 0.65 µm, 29.40 ± 0.75 µm, and 29.70 ± 0.70 µm for pure, 0.4 % beta-carotene, 0.1% tartrazine, and blend, respectively (Figure 2.4K). These results also matched the z-layer thickness (30 µm) that was created by the slicing of the 3D model, and consequently the z-translation step of the z-stage.

After analyzing the effects of light absorbers on the resolution, we focused on investigating their effects on the pore structure since the degree of porosity and pore size are crucial properties in these materials, which directly affect the application area. PolyHIPEs that contained 0.4 % beta-carotene, 0.1 % tartrazine, the blend, and pure polyHIPE were investigated in terms of the degree of porosity and pore size. Also, to fully understand the influence of the printing process on the internal structure of the polyHIPEs, the pore size and porosity within 3D-printed structures were examined. The data were compared with the measured pore size and porosity in a fresh batch of UV-cured polyHIPEs and with a sample taken out of the resin tank after the printing process was completed (UV-cured leftover). These data are summarized in Table 2.3 and Figure 2.4 and Figure 2.5 and provide the following interesting insight into the printing process.

Table 2.3. Pore size (µm), porosity (%), and layer thickness (µm)

Samples		Pore Size (μm)	Porosity (%)	Layer Thickness (μm)
3D-printed	**Pure**	13.97 ± 3.13	70.59 ± 2.62	30.35 ± 0.55
	0.4 B	15.27 ± 3.31	70.70 ± 1.14	29.65 ± 0.65
	0.1 T	18.75 ± 5.76	64.17 ± 4.58	29.40 ± 0.75
	Blend	18.36 ± 2.60	67.47 ± 2.09	29.70 ± 0.70
UV-cured fresh	**Pure**	37.05 ± 3.85	82.50 ± 0.57	n/a
	0.4 B	29.15 ± 4.35	80.58 ± 2.06	n/a
	0.1 T	32.25 ± 3.86	81.29 ± 2.10	n/a
	Blend	40.82 ± 6.18	80.77 ± 1.69	n/a
UV-cured leftover	**Pure**	21.39 ± 2.56	76.65 ± 1.40	n/a
	0.4 B	14.87 ± 2.73	70.20 ± 3.03	n/a
	0.1 T	20.15 ± 2.71	62.79 ± 3.80	n/a
	Blend	16.14 ± 2.30	76.86 ± 4.14	n/a

Focusing on the pore size within the 3D-printed objects first, the pore sizes of the pure, 0.4 % beta-carotene, 0.1 % tartrazine, and the blend samples were 13.97 ± 3.13 µm, 15.27 ± 3.31 µm, 18.75 ± 5.76 µm, and 18.36 ± 2.60 µm, respectively, indicating that the pure polyHIPE sample had the smallest pores while the 0.1 % tartrazine sample had the largest pore size. On the other hand, the similarity in the pore sizes of 0.1 % tartrazine sample and the blend sample has been observed. Secondly, pure and 0.4 % beta-carotene samples showed more uniform pores than 0.1 % tartrazine samples based on their standard deviations as this could be seen in Table 2.3, whereas the blend exhibited more uniform pores.
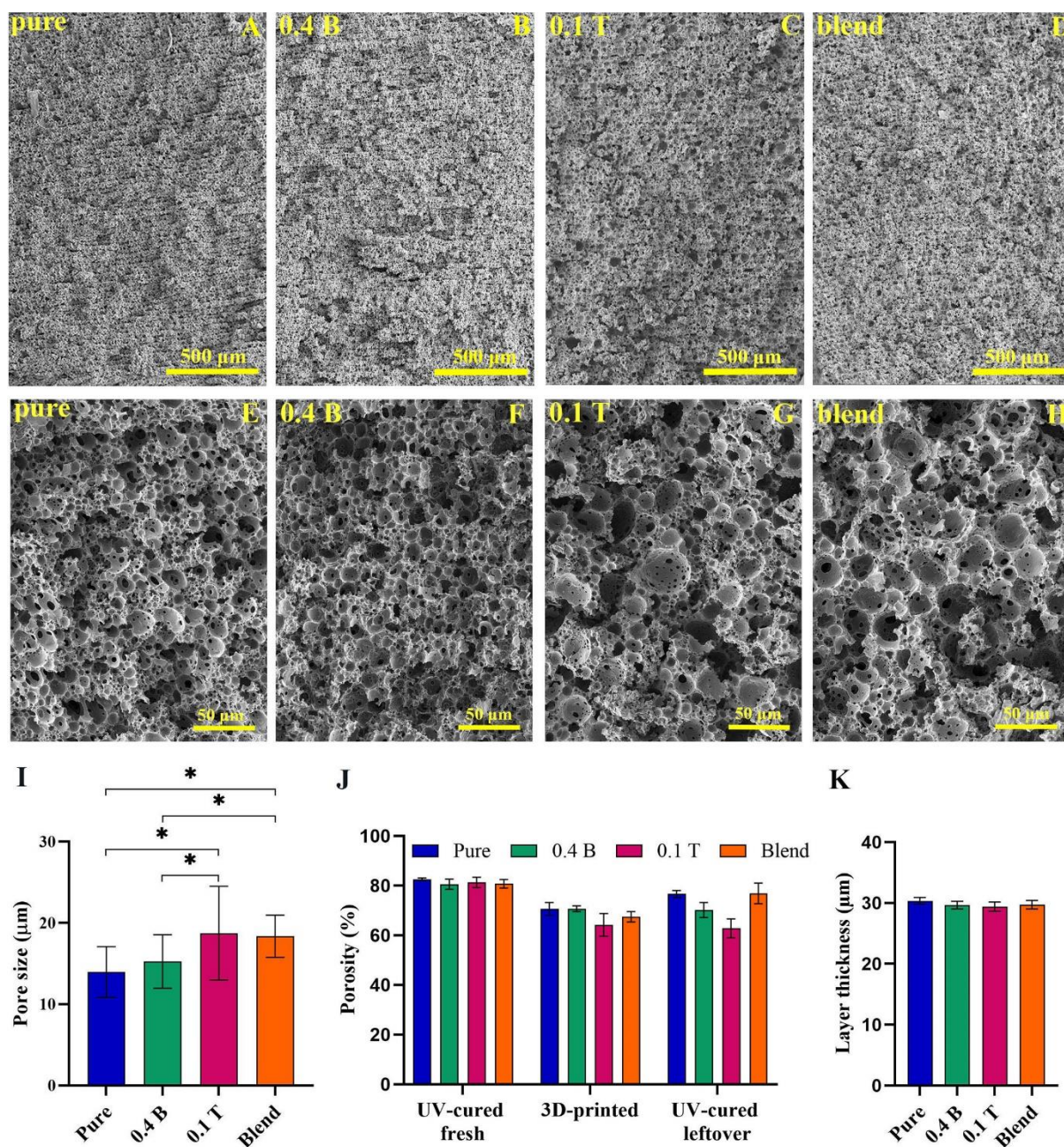
Figure 2.4. Layer-by-layer structure of 3D printed polyHIPE samples, **(A)** pure polyHIPE, **(B)** polyHIPE containing 0.4 % beta-carotene, **(C)** polyHIPE containing 0.1 % tartrazine, **(D)** polyHIPE containing blend (0.4 % beta-carotene and 0.1 % tartrazine). Porous microstructure of 3D printed polyHIPE samples, **(E)** pure polyHIPE, **(F)** polyHIPE containing 0.4 % beta-carotene, **(G)** polyHIPE containing 0.1 % tartrazine, **(H)** polyHIPE containing blend (0.4 % beta-carotene and 0.1 % tartrazine). **(I)** Pore size vs Samples graph, *: significant difference

(p<0.0001). (J) Comparison of the degree of porosity of UV-cured fresh, 3D-printed, and UV-cured leftover samples. (K) Layer thickness vs Samples graph. (n=3)

According to the statistical analysis (Figure 2.4I), the pore size of the 0.1 % tartrazine and the blend samples were compared with the pure and 0.4 % beta-carotene samples, and it was found that there was a statistically significant difference between them. On the other hand, there is no statistically significant difference between the pure and 0.4 % beta-carotene samples, and between 0.1 % tartrazine and the blend samples.
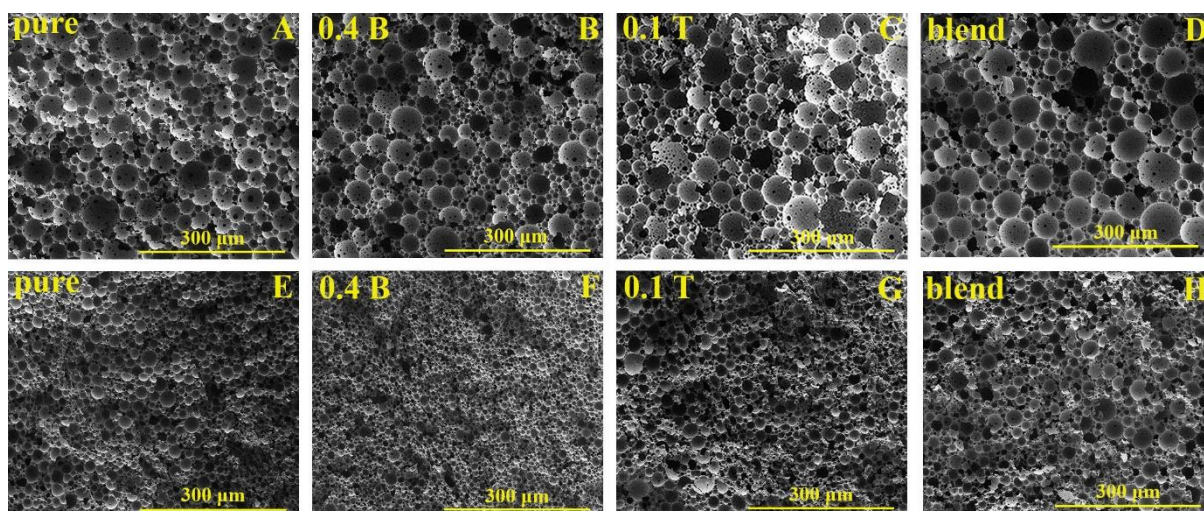
Figure 2.5. Porous microstructure of UV-cured polyHIPE samples from fresh HIPEs, **(A)** pure polyHIPE, **(B)** polyHIPE containing 0.4 % beta-carotene, **(C)** polyHIPE containing 0.1 % tartrazine, **(D)** polyHIPE containing blend (0.4 % beta-carotene and 0.1 % tartrazine) and from leftover HIPEs, **(E)** pure polyHIPE, **(F)** polyHIPE containing 0.4 % beta-carotene, **(G)** polyHIPE containing 0.1 % tartrazine, **(H)** polyHIPE containing blend (0.4 % beta-carotene and 0.1 % tartrazine). (n=3)

The porosity of the 3D-printed samples also showed a similar difference between the pure and beta-carotene-containing samples compared to the tartrazine-containing samples. The porosity drops to ~70% in the first group, while in the second group it drops to ~65%. Important to note is that this drop in porosity implies that the 3D HIPE emulsions do not produce polyHIPEs but

rather lower porosity polyMIPEs (for Medium Internal Phase Emulsions). To discard the potential effect of closed surface porosity of the printed objects on the measurement, the porosity was re-measured on 3D-printed samples with their surface layers removed and no difference was observed.
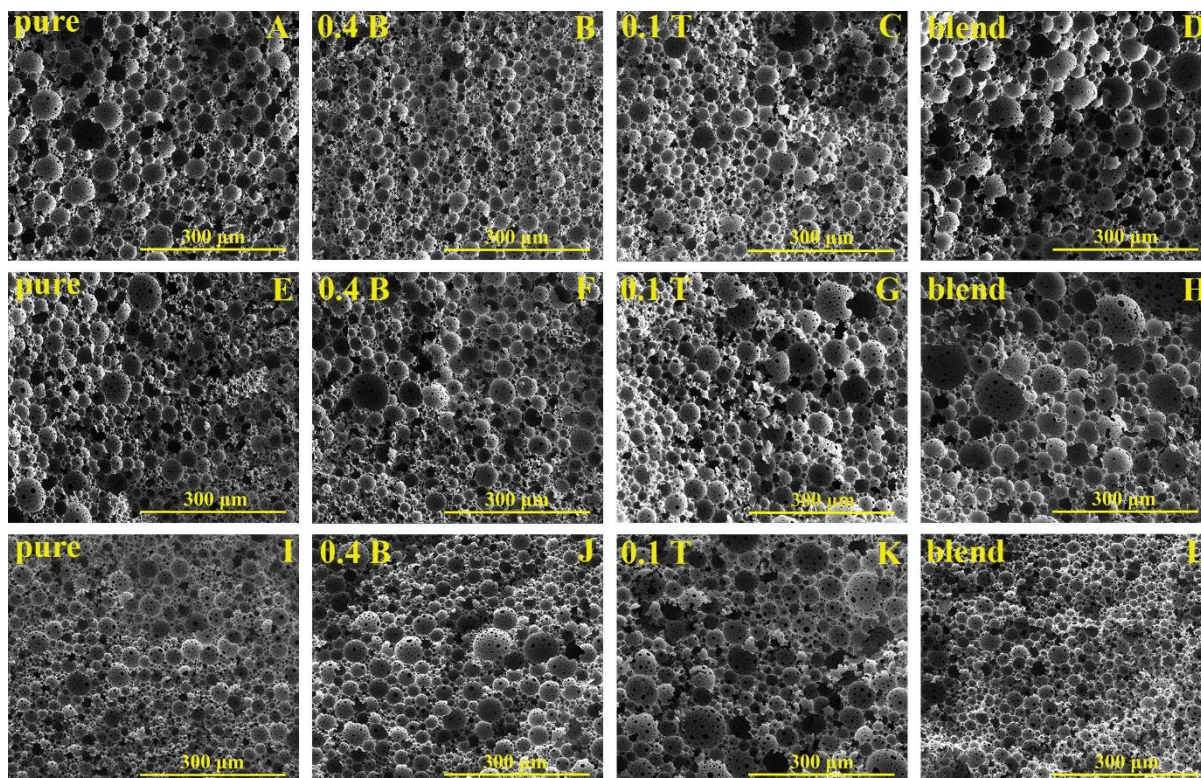
Figure 2.6. Porous microstructure of UV-cured polyHIPE samples after 1 day **(A)** pure polyHIPE, **(B)** polyHIPE containing 0.4 % beta-carotene, **(C)** polyHIPE containing 0.1 % tartrazine, **(D)** polyHIPE containing blend (0.4 % beta-carotene and 0.1 % tartrazine), after 3 days **(E)** pure polyHIPE, **(F)** polyHIPE containing 0.4 % beta-carotene, **(G)** polyHIPE containing 0.1 % tartrazine, **(H)** polyHIPE containing blend (0.4 % beta-carotene and 0.1 % tartrazine), and after 7 days **(I)** pure polyHIPE, **(J)** polyHIPE containing 0.4 % beta-carotene, **(K)** polyHIPE containing 0.1 % tartrazine, **(L)** polyHIPE containing blend (0.4 % beta-carotene and 0.1 % tartrazine). (n=3)

These results can be further compared to the results obtained from UV-cured polyHIPEs/MIPEs fabricated from fresh HIPEs and the emulsion that was left over in the resin

tank after printing. The results can be summarized as follows: the leftover resin produced polyMIPEs with very similar pore size and porosity compared to the 3D-printed objects (in between 15-20 µm and 62-76% depending on the formulation), while the UV-cured fresh polyHIPEs exhibited larger pore sizes (in between 30-40 µm and 80-82% depending on the formulation). These differences can be explained by the different conditions the emulsions are exposed to during printing versus standard UV-curing. During 3D printing, the emulsion gets agitated by the up-and-down movement of the printing platform during the pull-off and curing steps causing a reduction in the pore size during curing.

Table 2.4. Pore sizes (µm) in day 1, day 3, and day 7

Samples	Pore Size (µm)		
	Day 1	Day 3	Day 7
Pure	36.90 ± 5.01	33.96 ± 5.50	32.86 ± 4.67
0.4 B	29.55 ± 5.09	33.44 ± 5.22	35.76 ± 6.88
0.1 T	32.43 ± 5.68	34.79 ± 5.88	42.59 ± 6.94
Blend	40.28 ± 7.11	39.23 ± 7.82	34.26 ± 6.28

Also, interesting to note is that the tartrazine-containing samples showed a higher reduction in porosity than the others. The addition of tartrazine decreased the porosity in addition to the up-and-down movement of the printing platform. Based on these findings, a 7-day emulsion stability test was performed, and the results are presented in Fig. 6 and Table 4. Even though the pore sizes of 0.4 % beta-carotene polyHIPEs and 0.1 % tartrazine polyHIPEs increased as time increased, the blend and pure polyHIPEs showed a slight decrease in their pore sizes as time increased.

2.4.4. Surface Porosity

The outer surface of the cylinders was imaged via SEM to investigate the effects of light absorbers on the surface porosity. The pure and 0.4 % beta-carotene samples showed almost closed surfaces, whereas 0.1 % tartrazine and the blend samples provided porous surfaces. This indicated that oil-soluble (continuous phase) and water-soluble (internal phase) light absorbers have different effects on surface porosity and that only absorbers soluble in the internal phase ensure open surface porosity. This indicates that by including the light absorbers in the aqueous phase, the aqueous phase also absorbs the scattered light, which then reduces the occurrence of the poorly polymerized polymer boundary layer that gives rise to the polymer surface skin.
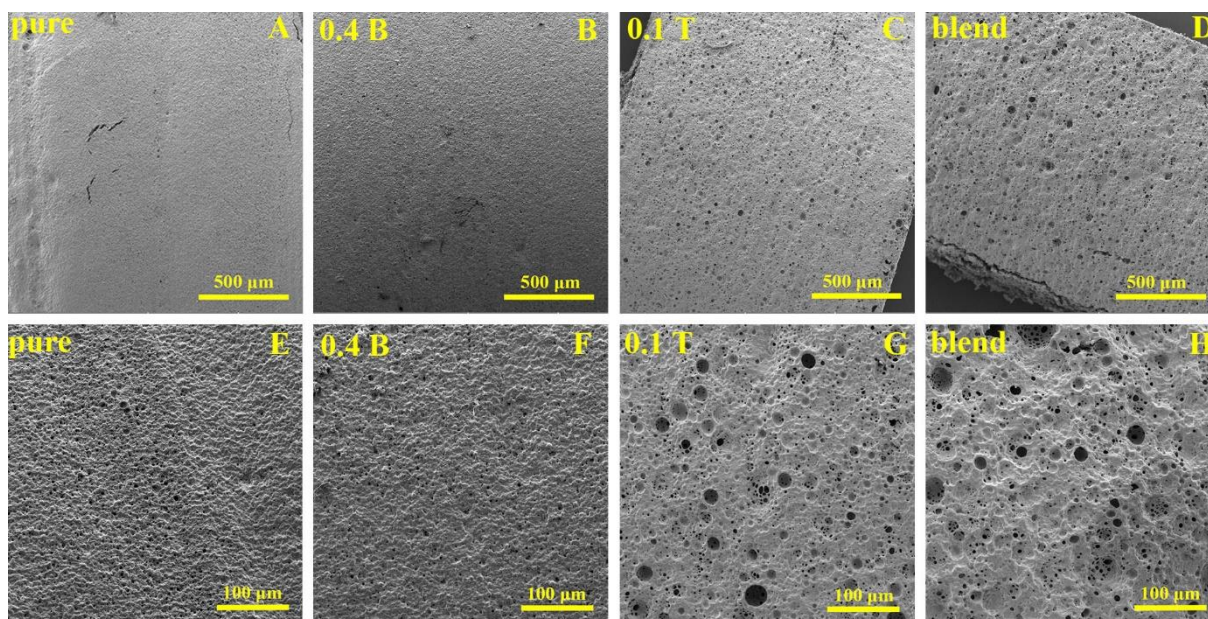
Figure 2.7. The porosity of the outer surface of the 3D printed samples **(A, E)** pure polyHIPE, **(B, F)** polyHIPE contains 0.4 % beta carotene, **(C, G)** polyHIPE contains 0.1 % tartrazine, **(D, H)** polyHIPE contains 0.4 % beta carotene and 0.1 % tartrazine. (n=3)

2.5. Discussion

Current literature indicates that there is a noted increasing interest in the use of porous materials, particularly polyHIPEs, in various applications [60]. Even though polyHIPEs are frequently proposed as materials for 3D cell culture and tissue engineering applications, they

are also usable in different industrial applications by controlling their porous morphology, and physical and mechanical properties [49], [59], [62], [129], [139], [140]. For the further adaptation of the polyHIPE technology in various industrial applications, these materials should also be able to be manufactured in a broad range of user-defined shapes. For this reason, manufacturing polyHIPEs via vat photopolymerization would be a convenient way since this process allows high-resolution fabrication.

Pure HIPEs were over-cured while fabricating cylinders with 5 mm and 10 mm heights and 15°, 30°, and 45° inclines. The reason for this over-curing is light scattering during the 3D printing process, as has been reported in the literature [141], [142]. Light scattering could be reduced by including light absorbers within the resin, thus enabling the manufacture of objects with improved resolution via vat photopolymerization. For example, Tinuvin Carboprotect and Tinuvin 234 have been used as light absorbers to improve the resolution of 3D printed polyHIPEs, as reported by Susec et al. and Sherborne et al., respectively [64], [69].

We achieved the best resolution using the blend light absorber (0.4 % beta-carotene and 0.1 % tartrazine). As highlighted in Table 1, between 0.1 and 1 wt% of beta-carotene and 0.1 and 0.4 wt% of tartrazine were used in the formulations (relative to the organic phase weight, this equates to 0.02 and 0.2 wt% of beta-carotene and 0.02 and 0.08 wt% of tartrazine relative to the total weight, i.e., organic and aqueous phase). Tartrazine dissolves in the aqueous phase while beta-carotene dissolves in the organic phase and given the water/polymer volume is 4:1. Beta-carotene and tartrazine have almost identical molecular weights (this gives the molar concentration of tartrazine in water at 0.1 wt. % (vs. organic phase weight) is 0.47 mM while the concentration of beta-carotene in the organic phase at 0.1 wt% (vs. organic phase weight) is 1.87 mM). Since light absorption is a volume effect, and the penetration depth is dependent on the amount of light absorber in the total irradiated volume, the molar % of beta-carotene/tartrazine per total volume can be used. In addition to these, while tartrazine exhibits a $6.23\times$ higher absorption compared to beta-carotene at the same molar concentration, the observed optimal ratio of 4:1 for their concentrations in the formulations may be influenced by additional factors such as their distribution between the organic and aqueous phases and their molecular interactions within the emulsion.

The use of blend light absorber allowed the 3D printing of a pyramid structure having inclined edges and a buckyball structure (Figure 2.3). Thus, we have manufactured the most complex

structures to date obtained from HIPEs via stereolithography-based additive manufacturing thanks to the inclusion of the blend light absorber. Additionally, these structures could be manufactured with both internal and surface porosity, but interestingly, the pore size within the printed structures was smaller than a structure directly UV-cured from a fresh HIPE (15-20 µm compared to 30-40 µm, Figure 2.5 and Table 2.2), and the total porosity decreased by ~10%. This was likely due to a few different conditions the emulsion is exposed to during printing. Indeed, the print platform moves in a concerted up-and-down movement during printing to pull off the printed layer from the resin tank and move back to the set z-layer thickness of 30 µm for the next photopolymerization cycle. This restricts the pore size within the scaffolds to be smaller than 30 µm since the emulsion droplets need to fit in between the resin tank and the printed structure on the printing platform. Additionally, the agitation associated with the movement of the printing platform induces increased mixing and smaller pores throughout the resin, as indicated by the similar pore size observed in the leftover resin after printing. The overall stability of the resins at room temperature is at least 7 days, with only a slight change in pore size observed during this period (Figure 2.6 and Table 2.3).

An important additional factor is the appearance of a closed polymer layer on the surface of the 3D-printed structures that contain no light absorber. This has been previously reported by Sherborne et al. [69] and is due to a poorly polymerized surface layer that collapses as surface skin onto the 3D-printed objects after washing. This study reported that UV-234 (Tinuvin 234) produces an open surface pore structure. Similarly, our work indicated that the inclusion of tartrazine enables an open surface pore structure (Figure 2.7G-H) while the inclusion of beta-carotene results in a closed surface (Figure 2.7). This tunability of closed/open surface porosity by the inclusion of different light absorbers is likely interesting for various applications; for example, in tissue engineering, open surface porosity is preferred to enable cell ingrowth.

2.6. Conclusions

To conclude, firstly, this study demonstrated that using the blend of beta-carotene and tartrazine as a light absorber considerably improves the 3D printing resolution for producing porous polymer structures. Thus, it allows the fabrication of more complex and detailed objects from HIPEs via stereolithography-based additive manufacturing. The blend of 0.4 wt% beta-

carotene and 0.1 wt% tartrazine relative to the organic phase has been shown to preserve both the surface porosity and internal porosity of the 3D-printed objects. The pore size was reduced in the 3D-printed objects compared to the UV-cured fresh polyHIPEs, from ~30-40 to 15-20 µm. The overall porosity was also reduced, and the 3D-printed porous polymers can be classified as polyMIPEs rather than polyHIPEs. This study illustrated that 3D printing of intricate structures of porous polymers is possible with commercial stereolithography setups, which opens the route towards using this technology for a host of applications.

CHAPTER 3

Investigating the Potential of Electroless Nickel Plating for Fabricating Ultra-Porous Metal-based Lattice Structures Using PolyHIPE Templates
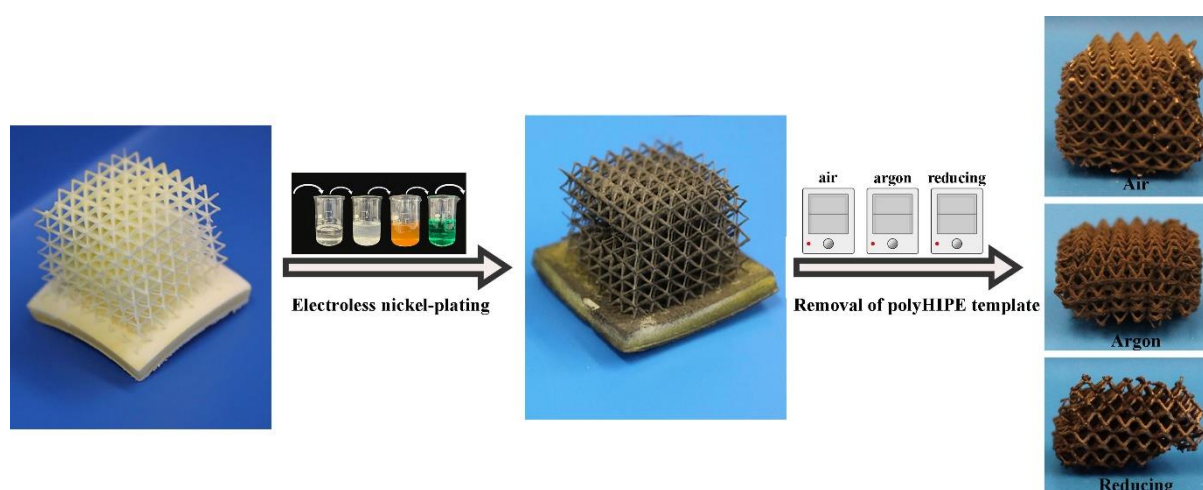
Abstract

The use of polymerized high internal phase emulsions (polyHIPEs) as templates for electroless nickel plating is a promising method for producing ultra-porous metallic lattice structures with consistent wall thickness. These structures have desirable properties such as low density, high specific strength, resilience, and absorbency, making them suitable for various applications including battery electrodes, catalyst supports, and acoustic or vibration damping. This study aimed to optimize and investigate the electroless nickel plating process on polyHIPEs. Initially, a surfactant (hypermer) stabilized water-in-oil emulsion based on 2-ethylhexyl-acrylate and isobornyl-acrylate was used as a 3D printing resin to create polyHIPE structures. Then, the electroless nickel plating process was optimized using polyHIPE discs. The study also examined the effects of air, argon, and reducing atmospheres during the heating process to remove the polyHIPE template using metallized 3D-printed polyHIPE lattice structures. The findings indicated that different atmospheres led to the formation of distinct compounds. While

nickel-coated polyHIPEs were fully oxidized in an air atmosphere, nickel phosphide (Ni_3P) structures occurred in argon and reducing atmospheres along Ni metal. Moreover, in argon and reducing atmospheres, the porous structure of the polyHIPEs was retained as the internal structure was completely carbonized. Overall, the study demonstrated that intricate polyHIPE structures can be used as templates to create ultra-porous metal-based lattices for a wide range of applications.

Keywords: PolyHIPE, 3D printing, stereolithography, emulsion templating, electroless nickel plating

3.1. Introduction

Porous structures have gained significant importance in various fields due to their unique properties, characteristics, and potential applications. On the basis of mimicking the structure of naturally-occurring porous materials, various porous structures have been created, such as foams, honeycombs, and lattice structures [143], [144], [145], [146].

Foams, honeycombs, and lattices are cellular structures. The term "cellular structure" was commonly used to describe porous materials before the emergence of the lattice structure [147], [148]. Lattices offer numerous superior qualities, such as being lightweight, highly durable, capable of absorbing energy, dissipating heat, and minimizing vibration, aspect which have been thoroughly investigated [149].

Lattices have been used in a wide range of industrial applications, including aerospace, automotive, construction, and biomedical engineering due to their exceptional properties [149], [150], [151]. These structures can be designed and optimized for specific properties, such as stiffness, strength, energy absorption, and thermal insulation, making them versatile materials for various applications [152], [153], [154], [155], [156], [157], [158]. Architected lattice materials, which are produced by mimicking the crystal microstructure of metals and alloys on the macroscale, are promising candidates for industrial applications [159], [160], [161]. They

are made of periodic configurations of nodes and struts usable as macroscopic mechanical mimics of bonds and atoms in crystal structures [143], [144].

The properties of a lattice material are governed by both the distribution of voids and solids as well as the solid ingredient [162], [163]. Various ultralight materials have been created in recent years using a variety of techniques such as polymer foams, metallic foams, ultralight nickel microlattices, and aerogels [146], [154], [164], [165], [166], [167], [168], [169]. As their density rises, ordered cellular lattice materials become more rigid and durable [154].

Metallic microlattices have a wide range of potential uses in thermal insulation, battery electrodes, catalyst supports, and acoustic, vibration, or shock energy damping[157], [158], [164]. They possess desirable characteristics such as low density, high specific strength, resilience, and absorbance [146], [154], [164], [170], [171], [172]. Furthermore, metallic lattice structures can be fabricated using various manufacturing techniques, directly from the metal material via investment casting, deformation forming, woven and non-woven metal textiles and powder bed fusion [173]. In addition, they can be fabricated from additive manufactured polymer templates that are metallized *via* electro- or electroless deposition and subsequently removed to achieve the final metallic structure [146].

To produce metal lattices non-porous polymer templates are normally used. Recently, we developed a polymer resin that is inherently porous via using emulsion templating and we reported its use as a resin for vat photopolymerization [69], [71]. In particular, polymerized high internal phase emulsions (polyHIPEs), porous polymers produced by a straightforward emulsion templating process, were used [49]. In this process two immiscible liquids (in our case a hydrophobic methacrylate phase and water) are mixed stabilized by surfactants or colloidal particles to form a continuous (external) phase and internal (droplet) phase. If the internal phase is more than 74% of the total volume, then the emulsion is classified as a high internal phase emulsion (HIPE) [49], [55], [56], [130]. PolyHIPEs are made from HIPEs by further polymerizing the external phase and removing the internal phase [49], [57]. Surfactant stabilized PolyHIPEs typically yield high surface area materials with highly interconnected pores, with adjustable and well-defined porosities. In addition to being employed as polymer-based tissue engineering scaffolds, catalytic supports, or filters, polyHIPEs can also be used as templates to create porous metals, ceramics, carbons, and composites [49], [50], [51], [52], [53], [54], [129], [174].

Traditional manufacturing methods of polyHIPEs such as casting (molding) can only produce geometrically simple designs, and do not offer flexibility in the production of the polyHIPEs [73], [131]. On the other hand, inherently porous and intricate lightweight structures including lattice structures can be fabricated via the combination of emulsion templating with additive manufacturing within a single step [65], [66], [69], [71]. Among additive manufacturing (AM) techniques, vat photopolymerization has the advantage of fabricating the 3D intricate structures directly from the design file with minimum effort. In this AM technique, commercial photocurable resins or emulsion-based resins are used as 3D printing materials [2], [33], [65], [66], [67], [69], [71], [175].

Via this route PolyHIPEs can be used as templates for producing metallic lattice structures using electroless nickel plating, which is a cost-effective and simple technique for fabricating complex shapes with uniform wall thickness [146], [157], [160], [170]. Electroless nickel plating is a widely used process for depositing a nickel-phosphorus alloy coating (2-14% phosphorus content) onto a substrate without the need for an external electrical power source [176], [177]. This plating technique involves a chemical reaction between the substrate and the plating solution, which results in a uniform coating with precise thickness. Electroless plating can be particularly useful in the production of metallic microlattices, where the precise control of wall thickness is critical to their mechanical properties and functionality.

To deposit a metal coating onto a polymer surface using electroless plating, metal nanoparticle catalysts like Pd, Ag, or Au need to be adsorbed on the surface initially. This process activates the metal cations in the plating solution, which reduce into metal atoms and deposition onto the activated surface. Polymer surfaces are usually inert, however, so pre-treatment is needed to introduce functional groups and enhance adhesion between the surface and the catalyst. This improves the affinity between the catalyst and the surface, promoting uniform and adherent metal deposition during electroless plating [178].

In this study, the use of additively manufactured polyHIPEs strut structures as templates for electroless nickel plating and their further heat treatment in different atmospheres such as air, argon, and reducing atmospheres was investigated for the first time. The heat treatment in air is intended to remove the polyHIPE polymer substrate, while the argon and reducing atmospheres aim to carbonize the polyHIPE. The first step involved 3D printing polyHIPE discs using a commercial stereolithography-based 3D printer (Elegoo Mars 3 Pro) and

optimizing the electroless nickel plating process by varying the coating time. Then, inherently porous lattice structures were 3D printed from high internal phase emulsions and nickel-coated. The effects of various atmospheres during the heating process on the final nickel lattice structure were explored.

3.2. Experimental

3.2.1. Materials

2-ethylhexyl acrylate (EHA), isobornyl acrylate (IBOA), trimethylolpropane triacrylate (TMPTA), a photoinitiator; diphenyl (2,4,6- trimethyl benzoyl)-phosphine oxide/2-hydroxy-2-methyl propiophenone (blend), beta carotene (synthetic, ≥93% (UV), powder), and tartrazine (dye content ≥85%), 3-(trimethoxysilyl)propyl methacrylate (TMPSM), tin (II) chloride ($SnCl_2$), palladium (II) chloride ($PdCl_2$), boric acid (H_3BO_3), and ~37% hydrochloric acid (HCl) were all purchased from Sigma Aldrich. The surfactant Hypermer B246-SO-M was donated by Croda. Electroless nickel plating solutions (Part A and Part B) were purchased from Caswell UK.

3.2.2. Preparation of High Internal Phase Emulsions

39.70 wt% 2-ethylhexyl acrylate (EHA), 39.70 wt% isobornyl acrylate (IBOA), 15.90 wt% trimethylolpropane triacrylate (TMPTA) (crosslinker), and 4.70 wt% Hypermer B246-SO-M (surfactant) were mixed to form the continuous organic phase (Table 3.1). The surfactant was dissolved in the mixture by heating it until it was completely dissolved at 50°C. Beta-carotene and tartrazine which were optimized in our previous work were added at 0.02 wt% and 0.06 wt% with respect to the continuous organic phase, respectively, to act as light absorbers [71]. The photoinitiator was then added to the continuous phase at 5 wt%. Finally, 80 vol.% of distilled water, dH_2O, as the internal phase was added dropwise while stirring the mixture at 300 rpm to form an emulsion using a SciQuip-Pro 40 stirrer.

Table 3.1. EHA, IBOA, TMPTA, hypermer, beta-carotene, and tartrazine ratio (wt%)

Organic phase				Light absorbers	
EHA (wt%)	IBOA (wt%)	TMPTA (wt%)	Hypermer (wt%)	Beta-carotene[a] (wt%)	Tartrazine[a] (wt%)
39.70	39.70	15.90	4.70	0.02	0.06

[a]Beta-carotene and tartrazine concentration with respect to the organic phase

3.2.3. 3D printing of polyHIPE discs and lattice structures

PolyHIPE structures were 3D printed using a stereolithography-based commercial 3D printer (Elegoo Mars 3pro). This 3D printer uses a 4K monochrome LCD screen with a resolution of 4098×2560 pixels and an XY resolution of 35 µm. The printer also features a chip-on-board lens with integrated UV LED lights paired with a Fresnel lens to deliver an even beam of 405 nm as a light source [179].

Computer-aided design (CAD) was used to prepare a 10 mm diameter $\times$ 2.5 mm height disc (SolidWorks 2018) (Figure 3.1A). The cubic vertex centroid lattice structure (to be mentioned as "lattice structure" or "lattice" in the text) was obtained from thingiverse.com [180]. Autodesk Fusion 360 was used to add a base to the lattice structure (Figure 3.5A). Both designs were formatted as .stl files and then sliced using CHITUBOX Basic.

10 mm diameter $\times$ 2.5 mm height discs and 18 mm $\times$ 18 mm $\times$ 20 mm lattice structures including 20 mm $\times$ 20 mm $\times$ 3 mm of the base were 3D printed with a layer thickness of 30 µm (Figure 3.1A and Figure 3.5B, C). The internal pore size of the 3D-printed polyHIPEs was 14.36 ± 5.78 µm (Figure 3.1B). The 3D printing parameters including exposure time, bottom layer count, and bottom exposure time etc. were presented in Table 3.2. To ensure a proper attachment of the structures to the printing platform, the bottom layers should have a higher exposure time than the general exposure time. The exposure time was optimized for each design to prevent overcuring. The overall 3D printing duration was ~20 minutes for 30 discs whereas 18 lattices were 3D printed in ~3 hours in one batch.

After 3D printing was completed, 3D printed structures were washed with methanol to remove any materials eluting from the polyHIPE (e.g. uncured resin), and then dried in an oven at 65 °C for 24 hours.
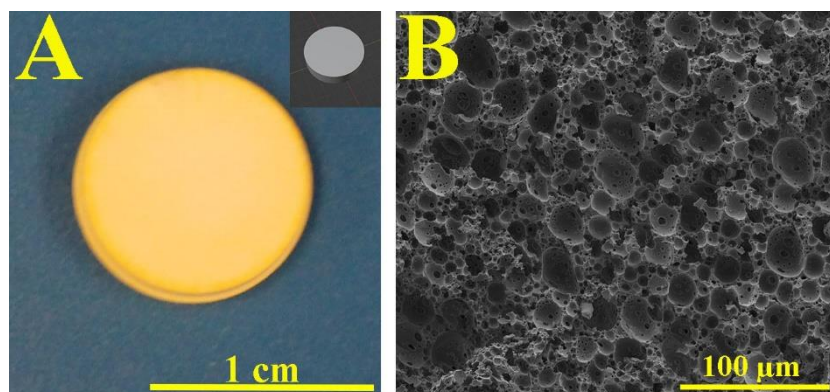
Figure 3.1. (A) 3D printed polyHIPE disc and the 3D model of the disc and **(B)** porous internal structure of the 3D printed polyHIPE.

Table 3.2. 3D printing parameters used to produce discs and lattices

Layer height (μm)	Bottom layer count	Exposure time (sec)		Bottom exposure time (sec)	Transition layer count	Bottom lift distance/Lifting distance (mm)
		Disc	*Lattice*			
30	5	10	8	40	5	5

Bottom lift speed (mm/min)	Lifting speed (mm/min)	Bottom retract speed/ Retract speed (mm/min)	Rest time before/after lift (sec)	Rest time after retract (sec)
60	70	50	0	0.5

3.2.4. Metallization of 3D printed polyHIPE discs and lattice structures

The nickel-plating protocol including pre-treatments that was published by Sun et al. was used by optimizing it for polyHIPEs [178]. All steps as a schematic diagram were illustrated in Figure 3.2.

Before the metallization process, surface functionalization is needed to make the polyHIPEs hydrophilic and surface activation is required to enable the deposition of nickel to the substrate. Firstly, polyHIPEs were immersed in 3-(trimethoxysilyl)propyl methacrylate silane (TMPSM) at 40°C for 15 min to enhance their hydrophilicity and then dried in an oven at 65°C until they were fully dried (~72 hours for discs and ~48 hours for lattices). Secondly, the silane-treated polyHIPEs were immersed in $SnCl_2$ and $PdCl_2$ solutions at 40°C for 20 min and 10 min, respectively. $SnCl_2$ solution was prepared mixing 0.8 wt% $SnCl_2$, 100 ml dH_2O, and 5 drops HCl. To prepare 100 ml $PdCl_2$ solution, 0.06 wt% $PdCl_2$, 2 wt% H_3BO_3, 100 ml dH_2O and 8 drops HCl were mixed. The pH of the $SnCl_2$ and $PdCl_2$ solutions was 1.2 and 1.7, respectively. 100 ml $SnCl_2$ and $PdCl_2$ solutions were used to treat 6 polyHIPE discs and 3 polyHIPE lattices to prevent any contamination.

Finally, an electroless nickel plating solution was prepared using Caswell solutions at the following concentrations, 5 vol.% Part A, 15 vol.% Part B, and 80 vol.% dH_2O [181]. Surface-activated polyHIPE discs were then immersed in the electroless nickel plating solution at 90°C for 5 min, 15 min, 30 min, and 1 h. For the polyHIPE lattices, 30 min plating time was applied. The concentrations used to prepare the solutions were presented in Table 3.3.

Table 3.3. Concentrations of pre-treatment and electroless nickel plating solutions.

Silane	$SnCl_2$ solution			$PdCl_2$ solution				Electroless nickel plating solution (Caswell)		
TMPSM	$SnCl_2$	HCl	dH_2O	$PdCl_2$	H_3BO_3	HCl	dH_2O	Part		dH_2O
								A	B	

100%	0.8 wt%	5 drops	100 ml	0.06 wt%	2 wt%	8 drops	100 ml	5 vol%	15 vol%	80 vol%
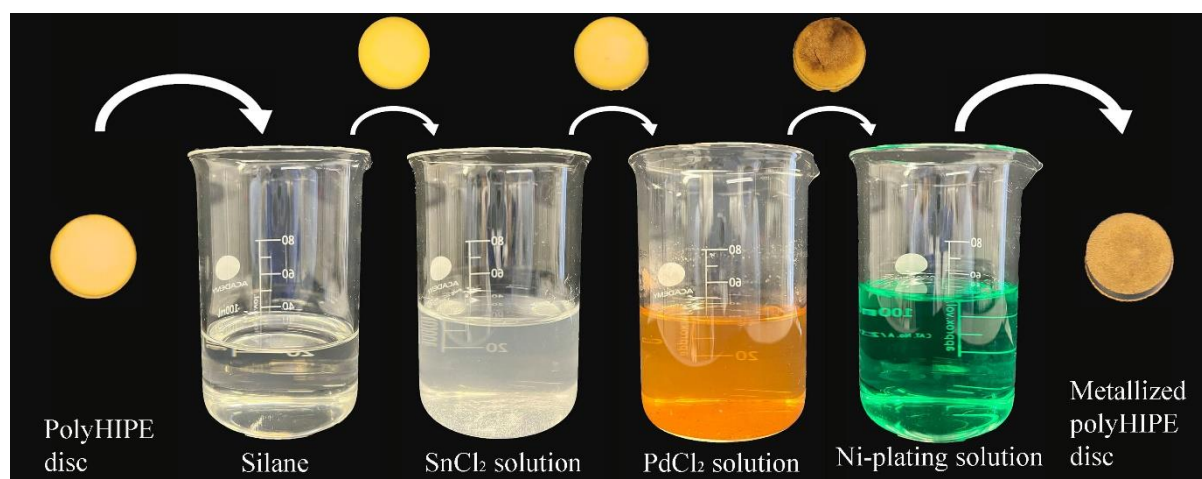
Figure 3.2. Schematic diagram of the electroless nickel plating process.

3.2.5 Incineration or Carbonization of the polyHIPE Template

The PolyHIPE templates used to produce metallized polyHIPE lattice structures were incinerated or carbonized in a high-temperature oven (Elite tube furnace, Elite Furnaces, UK). Different atmospheres, such as air, argon (Ar), and reducing (5% H_2/N_2), were used to study the incineration or carbonization mechanism of PolyHIPEs under various conditions. The temperature was increased to 700°C with a heating rate of 10°C/min. After reaching 700°C, the materials were held for a dwell time of 1 hour.

3.3. Characterization

3.3.1. Mercury Intrusion Porosimetry

The porosity of the polyHIPE discs was measured using a mercury intrusion porosimeter (AutoPore V, Micrometrics) before the metallization process. The highest applied pressure and the contact angle of mercury were 60000 psi (414 MPa) and 130°, respectively.

3.3.2. Attenuated Total Reflectance-Fourier Transform Infrared (ATR-FTIR) Spectroscopy

PolyHIPE discs were cut into 300 µm thickness pieces for the ATR analysis once they were silane-treated (PerkinElmer FT-IR Spectrometer Frontier). ATR measurements were obtained from 550 to 4000 cm^{-1} wavenumber at transmittance mode with a resolution of 4 cm^{-1} and 32 scans per sample.

3.3.3. X-Ray Diffraction (XRD)

X-Ray diffraction was used to analyze the crystallographic and phase structure of the metallized polyHIPEs discs and lattice structures. XRD was carried out using a PANalytical Aeris, operating at the reduced fluorescence measurement method (Cu tube 30kV 40mA, ¼° divergence slit, a 0.15 mm Ni filter, 0.02 Rad soller slits). The data were collected at diffraction angles (2θs) from 0° to 100° with a step size of 0.02°.

3.3.4. Scanning Electron Microscopy / Energy Dispersive X-Ray Analysis (SEM / EDX)

A FEI Inspect F SEM was used to investigate the internal structure of the non-metallized and metallized polyHIPEs and the surface of the metallized polyHIPEs. To increase the conductivity of the internal structure of the polyHIPEs, samples were gold-coated before imaging. An accelerating voltage of 5 kV was used for imaging. Pore sizes and nickel thicknesses were measured using ImageJ. Additionally, a statistical correction factor ($2/\sqrt{3}$) was applied to the pore size measurements to compensate for the underestimation of the diameter caused by uneven sectioning [182].

Elemental analysis of the Sn and Pd treated and metallized samples was done using SEM (Inspect F, FEI) with an energy dispersive analyzer with 20 kV power.

3.3.5. Thermogravimetric Analysis (TGA)

The thermal behavior of the non-metallized and metallized polyHIPEs (~5 mg and ~12 mg, respectively) was determined using thermogravimetric analysis (TGA, Pyris 1, PerkinElmer). Samples were heated in a nitrogen atmosphere from 30°C to 1000°C at a heating rate of

20°C/min. The weight loss % and increasing temperature relationship of the samples were recorded to identify the thermal characteristic of the polyHIPE samples.

3.3.6. Mechanical Testing

Compression testing was performed to evaluate the mechanical properties of the metallized polyHIPE discs (10 mm diameter $\times$ 2.5 mm height). A Mecmesin Multitest 2.5-dV mechanical testing machine equipped with a 250 N load cell was used at a rate of 1 mm/min. The data were obtained using Vector Pro software. The stiffness was determined from the initial linear slope of the stress-strain plot (n=6).

3.4. Results and Discussion

3.4.1. Pre-treatment of polyHIPEs

FTIR/ATR spectra of the polyHIPEs before and after the silane treatment were presented in Figure 3.3A. Five new peaks were observed to appear at 815 cm^{-1}, 940 cm^{-1} 1084 cm^{-1}, 1296 cm^{-1}, and 1637 cm^{-1}. The peak at 815 cm^{-1} was allocated to the bending vibration of C-H, while the peak at 940 cm^{-1} was designated to the stretching vibration of Si-O(H) [183]. Additionally, the peak at 1084 cm^{-1} and 1296 cm^{-1} were attributed to the stretching vibration of C-O, and the peak at 1637 cm^{-1} was ascribed to the stretching vibration of C=C [183], [184]. The occurrence of the new peaks indicated that 3-(trimethoxysilyl)propyl methacrylate silane was attached successfully on the polyHIPE surface.
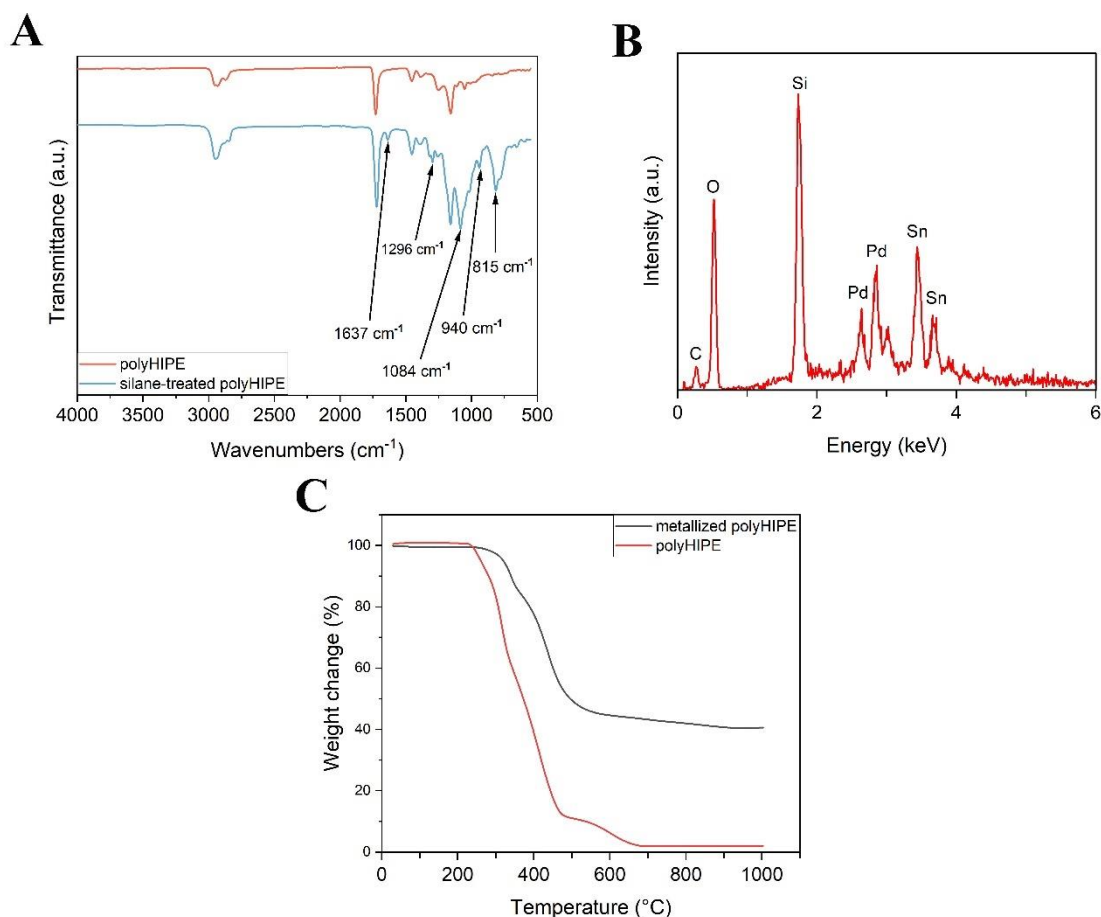
Figure 3.3. **(A)** FTIR/ATR graph of the silane-treated polyHIPEs, **(B)** EDX analysis of the Sn and Pd-treated polyHIPEs, and **(C)** TGA analysis of the non-metallized and metallized polyHIPEs.

Figure 3.3B showed the EDX analysis of the polyHIPE samples that were treated with silane, $SnCl_2$, and $PdCl_2$. The presence of C and O peaks was attributed to polyHIPE. The successful attachment of the silane was confirmed by the appearance of the Si peak. Moreover, the detection of Sn and Pd peaks in the EDX spectrum indicated that $SnCl_2$ and $PdCl_2$ were effectively attached to the surface of polyHIPEs.

The TGA analysis of both the non-metallized and metallized polyHIPEs was shown in Figure 3.3C. The analysis indicated that the degradation of polyHIPE was completed at 500°C, and the decomposition occurred between 500°C-700°C. The residual ash content was approximately 2%. Overall, the TGA graph, showed that the polyHIPE was completely

incinerated at 700°C, which is significantly lower than the melting point of the nickel (1453°C) [154]. Due to this reason, the metallized lattice structures were heated up to 700°C to remove the polyHIPE template.

3.4.2. Metallization of polyHIPE discs

Digital images of polyHIPE discs that were metallized for 5 min, 15 min, 30 min, and 1 h were shown in Figure 3.4A-D, respectively, and their corresponding SEM micrographs of the bottom of each sample were presented in Figure 3.4E-H. As expected, they exhibited a metallic appearance. Even though a 5 min metallized sample (Figure 3.4E) appeared porous, however, at 1 h the sample had no visible porosity (Figure 3.4H).

The EDX analysis presented in Figure 3.4I, along with the XRD analysis shown in Figure 3.4J, provided further evidence of successful nickel plating. The presence of peaks for Nickel (Ni), Phosphorus (P), and Oxygen (O) was observed in all the sample categories during EDX analysis. The Ni and P peaks were indicative of successful nickel coating, while the O peak could be due to the possible oxidation of the metallized samples.

XRD analysis reveals that Ni (111) peaks were present at $2\theta=44.5°$ in all the metallized samples [178]. However, a small broad feature attributed to the polyHIPE was only detected in the 5 min metallized sample at $2\theta=17°$. These findings suggest that full coating on polyHIPEs was achieved as the metallization duration increased. The crystallite size as calculated by the Scherrer equation and the degree of crystallinity of the 5 min, 15 min, 30 min, and 1 h metallized samples were 41.3 nm, 20.7 nm, 41.2 nm, 11.7 nm and 49.66%, 78.17%, 84.53%, 89.80%, respectively.
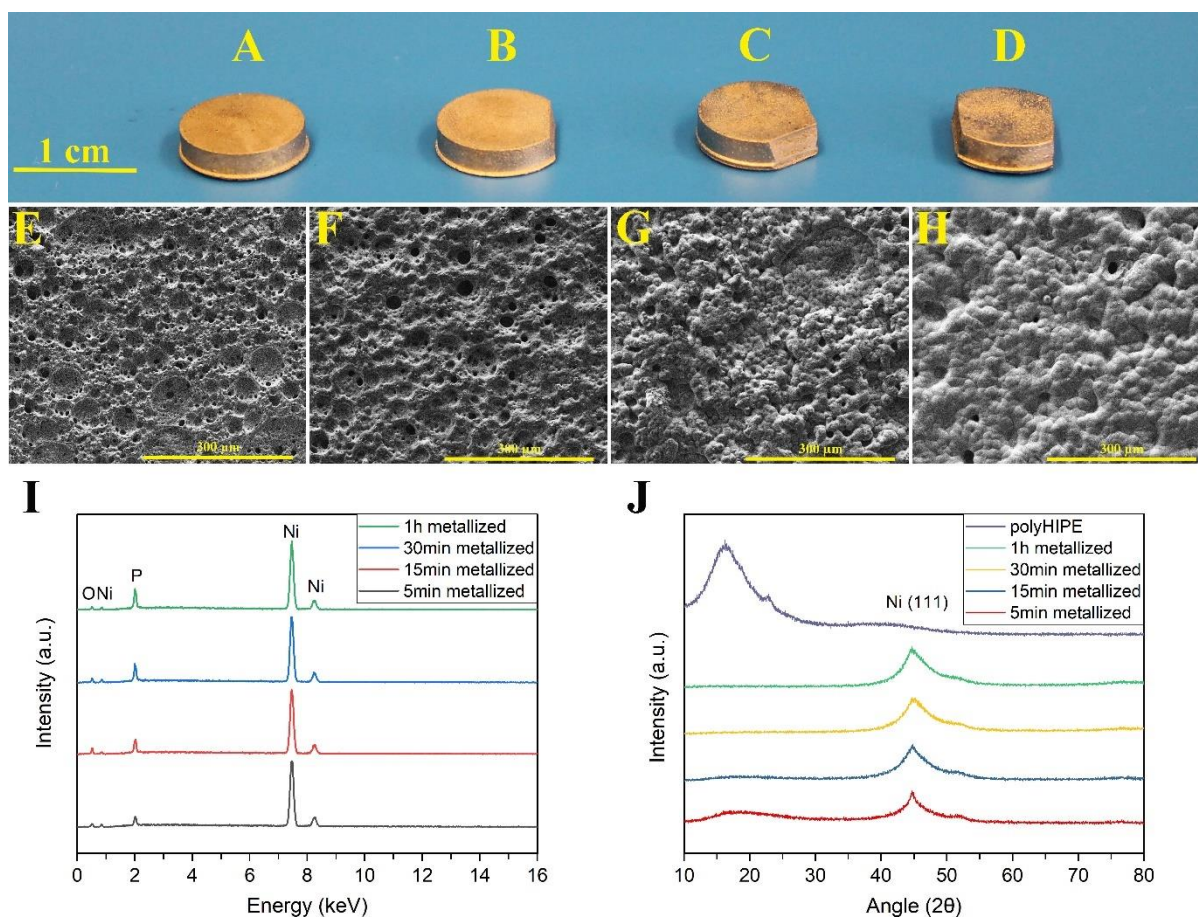
Figure 3.4. Metallized polyHIPE discs and their SEM micrographs, **(A, E)** 5 min, **(B, F)** 15 min, **(C, G)** 30 min, and **(D, H)** 1 h. **(I)** EDX and **(J)** XRD analysis of the metallized polyHIPE discs.

Furthermore, cross-section SEM micrographs of metallized samples for various time durations (5 min, 15 min, 30 min, and 1h) were presented in Figure 3.5A-D. These micrographs showed the nickel layer on the surfaces of the samples. However, as the nickel layer was not thick enough to be seen, higher magnification SEM images of the samples for each time duration, along with corresponding EDX mapping analysis that exhibited the presence of Ni, were illustrated in Figure 3.5E-H, I-L.

The thickness of a nickel layer deposited on polyHIPEs increases with deposition time between $1.66 \pm 0.54 \, \mu m$ for 5 mins and $10.20 \pm 0.98 \, \mu m$ for 1 hour deposition (Table 3.4). The overall porosity of the nickel coated samples was around 50%, while the non-metallized polyHIPE had a higher overall porosity of 74.96%. This indicates that nickel deposition process does deposit

a thin film on the surface of the macrostructure, instead of conformally coating the internal structure of the polyHIPEs. Indeed, this is mainly confirmed by the SEM cross-sections and EDX mapping presented in Figure 3.5 and indicates that the growing nickel coating reduces the surface porosity of the polyHIPEs and increasingly acts as a barrier for fluid or gas flow in the internal structure by sealing off the surface pores. The results of the EDX mapping analysis shows that still some nickel diffusion occurred into the internal structure because of the surface porosity (Figure 3.5I-L). This finding supports the idea that when pores are sufficiently large and interconnected, metal diffusion can occur, resulting in fully metallized pores. Previous literature indicated the possibility of metallizing the internal structure of polyHIPEs, and the EDX mapping results of this study provided further evidence to support this idea [185], [186].
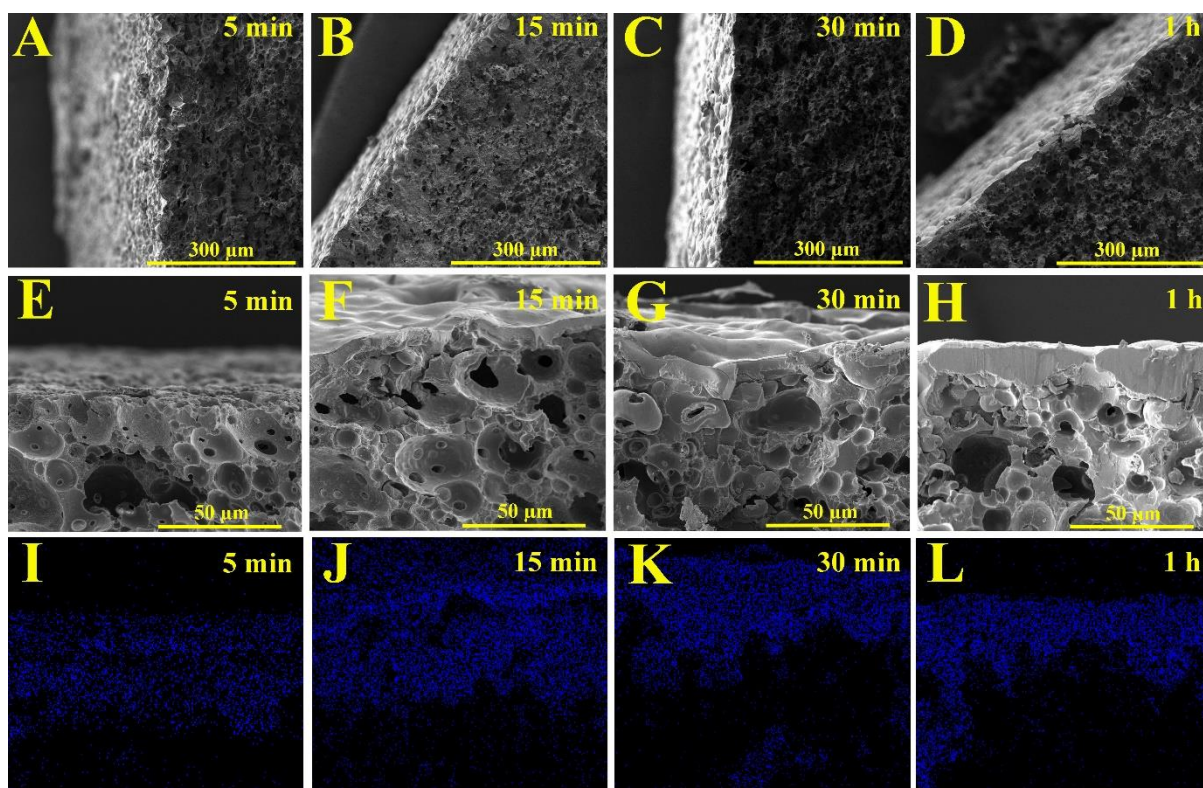
Figure 3.5. Cross-section SEM images of the metallized polyHIPE discs, **(A)** 5 min, **(B)** 15 min, **(C)** 30 min, and **(D)** 1 h in lower magnification. Cross-section SEM images of the metallized polyHIPE discs and their corresponding EDX analysis, **(E, I)** 5 min, **(F, J)** 15 min, **(G, K)** 30 min, and **(H, L)** 1 h in higher magnification.

In addition to these, the weight change (%) of the metallized samples increased in between 9.88 ± 7.09% for 5 mins deposition to 37.76 ± 8.20% for 1 hour deposition and this increase leads to an overall increase in density. Table 3.4 presents the density and stiffness under compression of the printed disks with the increasing nickel-plating time. As expected, the density of the metallized samples increased with the plating time. The non-metallized polyHIPE had a density of 1.08 g/cm^3, while the metallized samples had densities ranging from 1.18 g/cm^3 for 5 mins to 1.47 g/cm^3 for 1 hour deposition.

The non-metallized polyHIPE disc had stiffness of 1.12 ± 0.31 MPa, whereas the stiffness of the 5 min metallized sample increased to 5.04 ± 2.11 MPa. After this initial increase the stiffness of the disks did not change significantly with thicker nickel coating (from 4.60 ± 1.20 MPa for 15 mins to 3.87 ± 0.75 MPa for 1 hour coating). This indicates strongly that only the outer surface of the polyHIPE disc is coated (as a nickel shell to the polyHIPE disc) and there is very limited coating of the internal polyHIPE structure.

Table 3.4. Porosity (%), Ni layer thickness (µm), weight change (%), density (g/cm^3), and Stiffness (MPa) values of the non-metallized and metallized polyHIPE discs.

Samples	Porosity (%)	Ni thickness (µm)	Weight change (%)	Density (g/cm³)	Stiffness (MPa)
polyHIPE	74.96	n/a	n/a	1.08	1.12 ± 0.31
5 min metallized	52.77	1.66 ± 0.54	9.88 ± 7.09	1.18	5.04 ± 2.11
15 min metallized	47.72	3.20 ± 0.54	19.44 ± 9.33	1.20	4.60 ± 1.20
30 min metallized	51.05	4.20 ± 1.24	28.32 ± 3.94	1.35	4.20 ± 1.44
1 h metallized	49.63	10.20 ± 0.98	37.76 ± 8.20	1.47	3.87 ± 0.75

3.4.3. Metallization of polyHIPE lattice structures
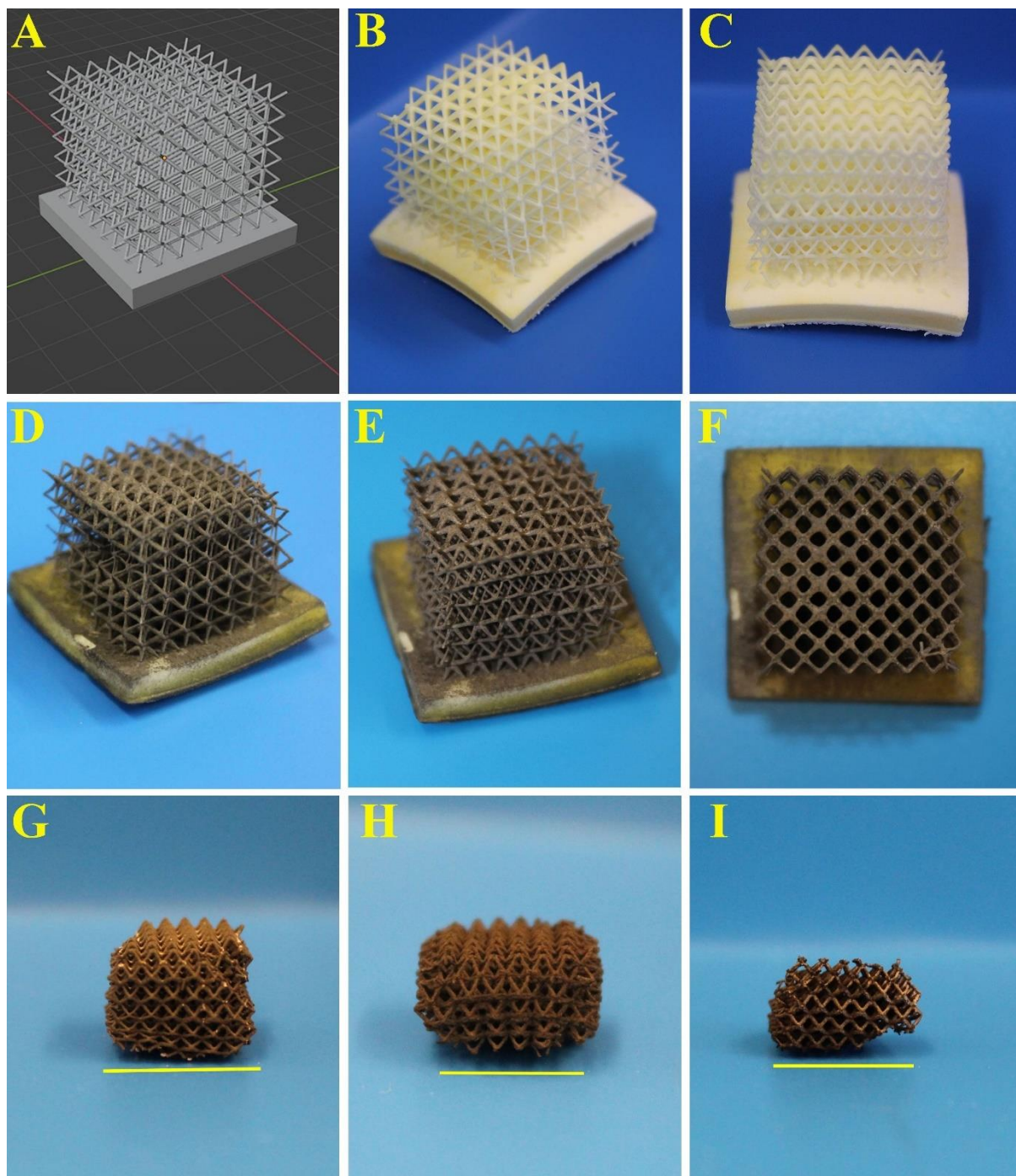
Figure 3.6. (A) 3D design of the lattice structure, **(B, C)** 3D printed lattice structure from different perspectives, **(D-F)** nickel-plated lattice structure from different perspectives, and the lattice structure after the removal of the polyHIPE template in the **(G)** air, **(H)** argon, and **(I)**

reducing atmospheres. (Lattice size in B, C, D, E, and F is $18 \times 18 \times 20$ mm and scale bars in G, H, and I are 10 mm).

Figure 3.6A-C illustrated the 3D design of the lattice structure and the 3D printed lattice structure from different perspectives, respectively. The lattice structure had a void size of 1.34 ± 0.26 mm and a strut thickness of 0.27 ± 0.05 mm. It was observed that the 3D-printed design and structure were similar to each other in terms of printing resolution. Figure 3.6D-F showed the metallized lattice structure from different perspectives, revealing a uniform nickel plating without any deformation in the structure. This highlights that electroless nickel plating provides a uniform coating on intricate structures.

The lattice structures were heated in air, argon, and reducing atmospheres to either remove the polyHIPE template via incineration (in air) or to carbonize the polyHIPE (in argon or reducing atmospheres) after metallization, and the results were presented in Figure 3.6G-I. As expected, some shrinkage occurred in the lattices after the heating of the polyHIPE template. It was observed that different atmospheres caused similar shrinkages. Specifically, the air, argon, and reducing atmospheres caused 86.11 ± 1.17 vol.%, 85.81 ± 4.10 vol.%, and 86.15 ± 4.15 vol.% shrinkages in the structure, respectively. The lattice structures heated in the air had more consistent shrinkage than those heated in argon and reducing atmospheres, as indicated by their standard deviations in shrinkage.

SEM micrographs of the lattice structures heated in air, argon, and reducing atmospheres were presented in Figure 3.7, respectively. Figure 3.7A, D, and G showed images taken from the top of the lattice structures, while the cross-section images were presented in Figure 3.7B, E, and H. Finally, one representative strut for each category at higher magnification was exhibited in Figure 3.7C, F, and I. The average strut thickness after heating was 0.16 ± 0.03 mm, 0.22 ± 0.05 mm, and 0.19 ± 0.04 mm for the air, argon, and reducing atmospheres, respectively. On the other hand, the strut thickness of the metallized lattice structure was 0.29 ± 0.08 mm. After the removal of the polyHIPE template, the struts of the lattices shrank by an average of 44.83%, 24.14%, and 34.48% in air, argon, and reducing atmospheres, respectively.
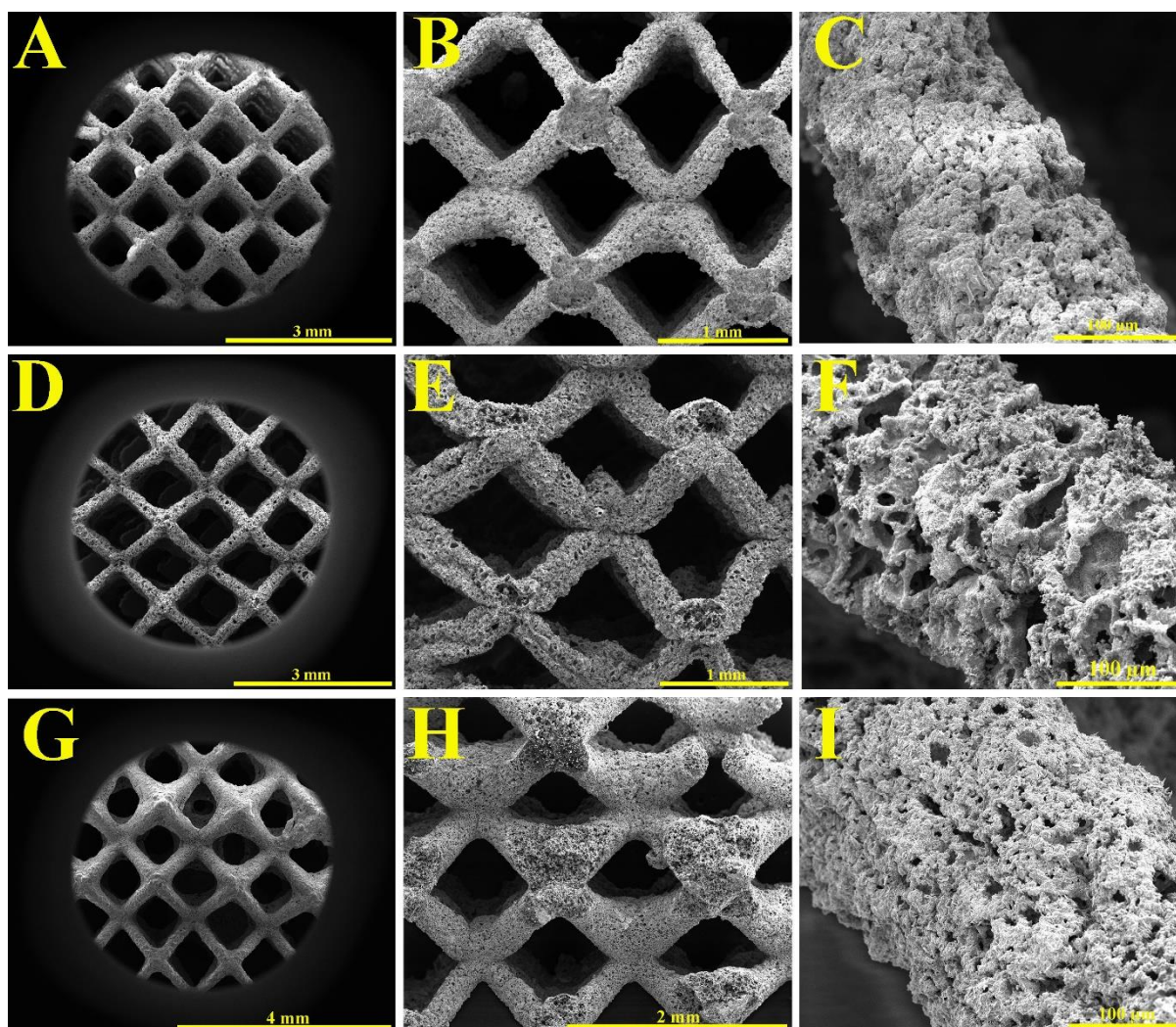
Figure 3.7. (A, D, G) The SEM micrographs from the top, **(B, E, H)** the cross-section, and **(C, F, I)** the strut in higher magnification of the lattice structures heated in air, argon, and reducing atmospheres, respectively.

The results indicated that the choice of atmosphere during the heating process had a significant effect on the shrinkage of the metallic polyHIPE lattice structures. Incineration in air led to a complete combustion and consistent shrinkage in both the macrostructure and struts due to the presence of oxygen, leading to more uniform and consistent shrinkage. In contrast, carbonization in argon or reducing atmospheres led to less shrinkage in the struts but significant shrinkage in the macrostructure. However, in inert or reducing atmospheres, there was no combustion, and we observed still an internal porous carbon scaffold within the struts. In air atmosphere, the nickel struts are completely empty. Interestingly, the macrostructure still

shrank isotropically, without destroying the 3D strut structure. Also, it is interesting to observe from the SEM figures (Figure 3.7 C, F, and I) is that all three nickel coatings are highly porous.
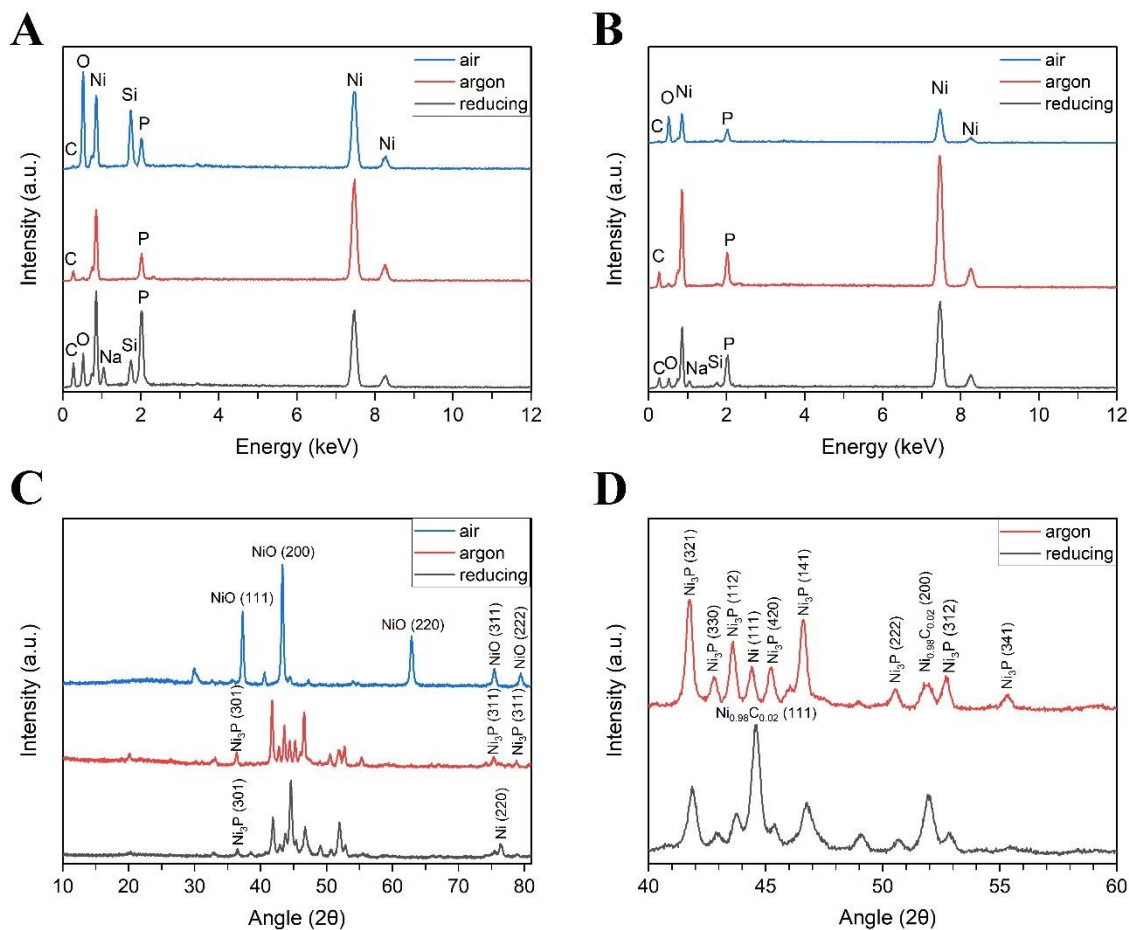
Figure 3.8. (A) EDX analysis of the lattice surfaces and **(B)** EDX analysis of the strut from the cross-section of the lattices. **(C)** XRD analysis of the lattices and **(D)** the zoomed-in XRD analysis graph.

Figure 3.8 displayed the EDX and XRD analyses of the lattice structures after heating. Figure 3.8A and B showed the EDX analysis performed on the surface of the lattice structures and the struts, respectively. The presence of nickel (Ni) peaks in all three conditions confirmed the effective nickel plating on both the lattice surface and the struts. These results possibly demonstrated the feasibility of uniformly coating intricate polyHIPE structures using the electroless plating technique. Moreover, the formation of phosphorus (P) and sodium (Na)

peaks could be attributed to the electroless nickel plating solution, whereas the silicon (Si) peak was observed due to the application of silane to enhance the hydrophilicity of the polyHIPEs.

The XRD analysis of the lattices and the zoomed-in XRD analysis to observe the peaks clearly were presented in Figure 3.8C and D, respectively. Concerning the XRD analysis, in air-heated lattices, only NiO peaks were present, indicating that the lattice structure was fully oxidized in an air atmosphere (NiO: PDF-4+ ICDD 04-006-6925). Meanwhile, in argon-heated lattices, metallic nickel (Ni), Nickel Phosphide (Ni_3P) and nickel carbide ($Ni_{0.98}C_{0.02}$) peaks were observed (Ni_3P: PDF-4+ ICDD 01-089-4748, Ni: PDF-4+ ICDD 04-010-6148, $Ni_{0.98}C_{0.02}$: PDF-4+ ICDD 01-074-5561). Furthermore, very similar compounds (Ni and Ni_3P) were formed in the reducing atmosphere-heated lattices (Ni_3P: PDF-4+ ICDD 01-089-4748, Ni: PDF-4+ ICDD 04-010-6148, $Ni_{0.98}C_{0.02}$: PDF-4+ ICDD 01-074-5561). No carbon related peaks were observed indicating that the carbon phase is highly amorphous. The XRD identifies both metallic nickel and nickel phosphide (Ni_3P) under inert and reducing atmospheres.

During the electroless nickel plating process, a variety of nickel-phosphorus alloys are deposited on the substrate according to the phosphorus concentration [177]. The metallurgical characteristics of the alloys are determined by the amount of phosphorus, which can range from 2-14%. [177]. The previous work on the nickel coating of polyHIPEs showed the formation of different forms of nickel phosphides ($N_{12}P_5$, Ni_2P, and Ni_3P) [186]. However, the solid-state reaction occurs at temperatures of 600ºC or higher, and Ni_3P is specifically created when there is an excess of nickel [187]. Due to the treatment temperature of 700ºC and the higher concentration of nickel relative to phosphorus (Figure 3.4I) in our experimental conditions, Ni_3P was anticipated to form. Interestingly, Ni_3P is known as a high-performance catalytic phase [188]. The formation of this compound indicates that these structures can be good candidates for the catalytic applications.

The final observation indicated that all three types of lattices became brittle after the heat treatment, with the lattice heated in a reducing atmosphere being the most brittle.

In addition to these, Scherrer analysis was performed on the aforementioned peaks, revealing an average crystallite size of 27.96 nm (NiO), 31.92 nm (Ni_3P), and 26.92 nm (Ni_3P) in air, argon, and reducing atmospheres, respectively.
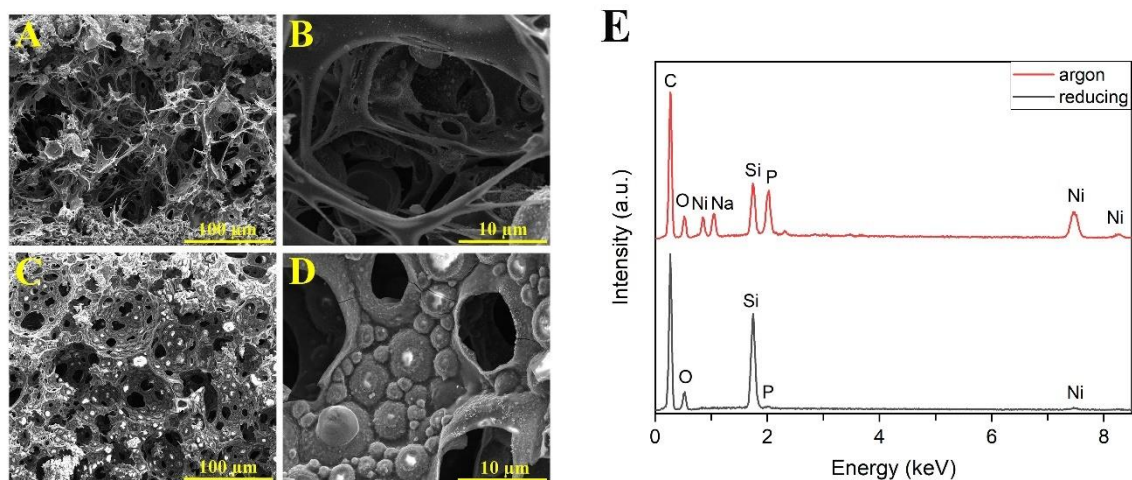
Figure 3.9. The internal porous structure of the lattice structures burned in **(A, B)** argon and **(C, D)** reducing atmospheres. **(E)** EDX analysis of the internal porous structures.

As mentioned, the lattice structures heated in argon and reducing atmospheres have an amorphous carbon network remnant, within the struts as illustrated in Figure 3.9A-B and C-D, respectively. EDX analysis was carried out in high-magnification SEM micrographs (Figure 3.9B, D). The findings revealed that the carbon (C) peak had the highest intensity, indicating the presence of the internal porous carbon structure in argon and reducing atmospheres (Figure 3.9E). Moreover, the analysis detected the formation of nickel (Ni) and phosphorus (P) peaks, demonstrating the occurrence of some nickel/nickel phosphide nanoparticles in the internal structure.

3.5. Conclusions

Electroless nickel-plating was examined and optimized to create ultra-porous metallized structures on polymerized high internal phase emulsions (polyHIPEs). To achieve this, 3D-printed discs were fabricated using high internal phase emulsions (HIPEs) and metallized for various durations (5 min, 15 min, 30 min, and 1 h) with the electroless nickel-plating technique. The process was investigated using XRD, SEM, and EDX analyses. Subsequently, 3D-printed polyHIPE lattice structures were uniformly coated with nickel. To either remove or carbonize the polyHIPE templates, the metallized lattice structures were heated in air, argon, and reducing

atmospheres. The nickel coating remained intact after the polyHIPE templates were removed. Heating polyHIPEs in different atmospheres led to the formation of various compounds. Metallic polyHIPEs heated in an air atmosphere were entirely oxidized, while nickel metal and nickel phosphide (Ni_3P) hybrid structures formed in argon and reducing atmospheres. Additionally, the internal structure of the polyHIPEs was fully carbonized while preserving the porous structure in argon and reducing atmospheres.

CHAPTER 4

Inherently porous carboHIPE lattice structures derived from 3D-Printed PolyHIPEs
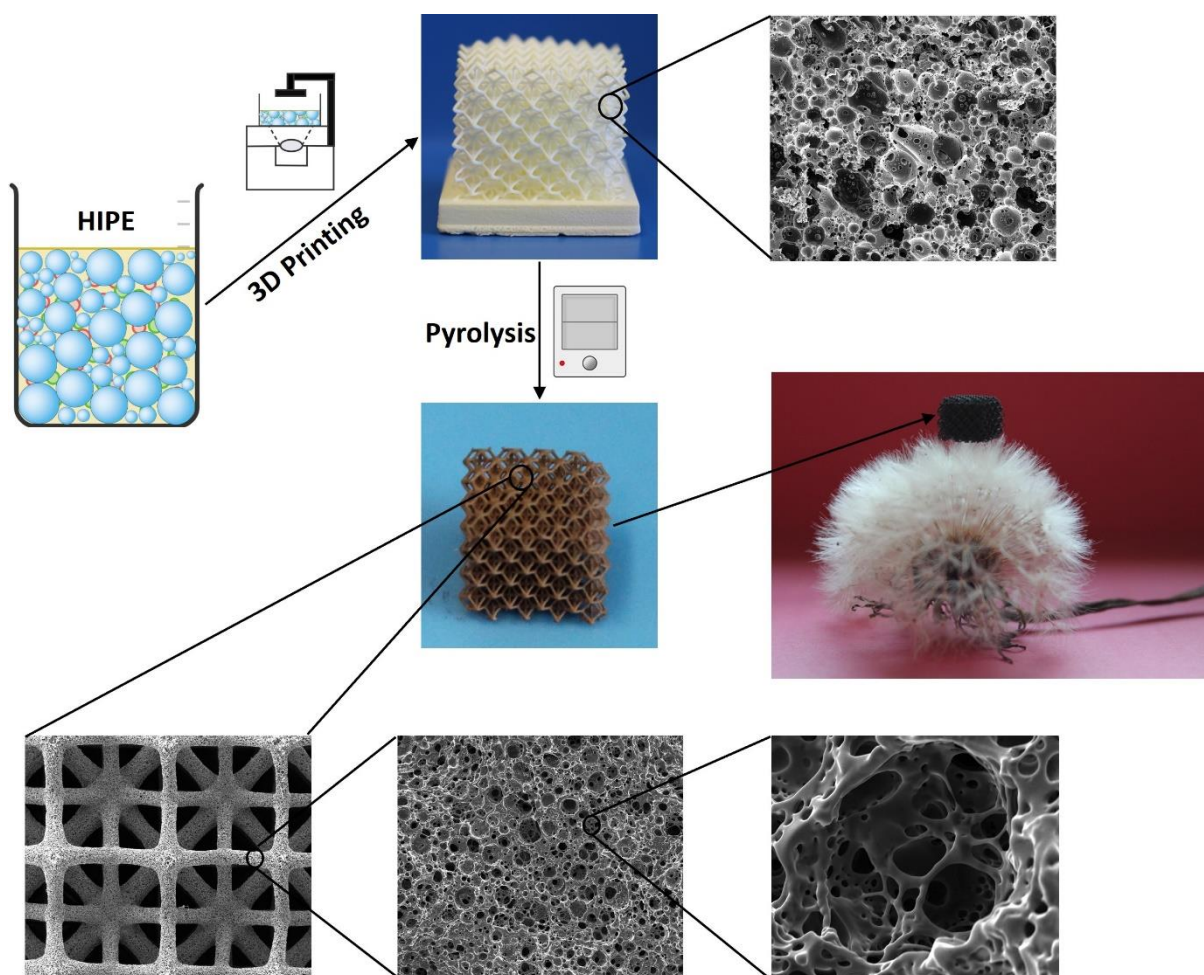
Abstract

Porous carbons have drawn significant scientific interest, mainly due to carbon's chemical stability, affordability, and exceptional surface area. These materials find applications in diverse areas such as energy storage devices, water contaminant adsorption, and gas separation. Emulsion templating is a promising method to fabricate hierarchically porous carbon materials

with interconnected pores at various scales and high surface areas. Combining this technique with additive manufacturing, in particular vat photopolymerization, offers opportunities for creating intricate, inherently porous materials with hierarchical porosity, including complex carbon lattice structures.

This study investigated the use of 3D-printed polyHIPE lattice structures to fabricate inherently porous carboHIPE lattices. Surfactant-stabilized water-in-oil emulsions, based on 2-ethylhexyl-acrylate and isobornyl-acrylate as a 3D printing resin, were used to produce polyHIPE lattices with three distinct porosities (80%, 85%, and 87.5%). The inherently porous lattice-shaped polyHIPEs were pyrolyzed at various temperatures (500ºC, 600ºC, 700ºC, and 800ºC) to fabricate carboHIPE lattices. Raman spectra indicated successful carbonization, while XRD analysis validated the carbon structure. Moreover, mechanical testing results demonstrated a higher Young's modulus in carboHIPEs compared to polyHIPEs, with carboHIPE lattices exhibiting lower Young's modulus compared to discs. Overall, this comprehensive exploration contributes insights into the design and performance of hierarchically porous carbon materials fabricated by using 3D-printed polyHIPE lattices.

Keywords: vat photopolymerization, emulsion templating, polyHIPEs, porous carbon, lattice

4.1. Introduction

In recent decades, there has been growing interest in the production of porous polymer structures due to their versatility in design and relatively cost-effective manufacturing process [49], [56], [129]. The research focus in porous polymers has primarily been on creating polymers with adjustable physical properties, well-defined porosities ranging from micrometer to millimeter sizes, and high surface areas. This has opened up various potential applications, including filter materials, catalyst supports, and scaffold materials for tissue engineering and 3D cell culture [49]. Porous polymers can also serve as templates for manufacturing porous metals, ceramics, carbons, and composites. Moreover, by mimicking the configurations found

in naturally occurring porous materials, diverse porous arrangements have been created, including foams, honeycombs, and lattices. [143], [144], [145], [146].

Porous materials possessing substantial surface areas, particularly within the category of porous carbons, have attracted considerable scientific attention [189]. This interest primarily stems from carbon's chemical stability, affordability, and remarkable surface area. Porous carbons can be used in various applications, including their use as electrodes in energy storage devices like lithium-ion batteries [190] and supercapacitors [191], as adsorbents for water contaminants [192], [193], and materials for gas separation [194].

Numerous conventional methods have been devised for creating carbon-based materials, including carbonization and activation processes [195], [196]. Carbonization involves high-temperature decomposition of carbon precursors under inert conditions, leading to porous carbon materials [197], [198]. Various techniques, including pyrolysis [199], hydrothermal carbonization (HTC) [200], chemical vapor deposition (CVD) [201], ball milling [202], and arc discharge [203], are employed, influencing the resulting structure, morphology, and composition of the porous carbons. Activation processes, chemical and physical, play a vital role in restoring porosity, with chemical activation introducing nano porous carbon structures [204].

Nonetheless, conventional techniques produce porous carbons with restricted adjustability in terms of porous structure and pore sizes. In contrast, emulsion-based approaches, such as emulsion templating, emulsion polymerization/microencapsulation, and emulsion freeze drying, are emerging as promising methods to fabricate hierarchically porous carbon materials with interconnected pores at various scales and high surface areas [195], [205].

Emulsion templating is a manufacturing technique used to create porous interconnected polymeric materials, with a particular focus on polymerized high internal phase emulsions, commonly referred to as PolyHIPEs [49], [129]. In this process, two immiscible liquids, one forming the external (continuous) phase and the other the internal (droplet) phase, are mixed and stabilized through the addition of surfactants [57], [206] or colloidal particles [130], [207], [208]. An emulsion is classified as a high internal phase emulsion (HIPE) when the internal phase makes up more than 74% of the total volume, which represents the maximum volume that can be occupied by uniform spheres [209]. The production of PolyHIPEs involves further polymerization of the external phase and subsequent removal of the internal phase.

Emulsion-templated polymers exhibit significant potential as precursors for customizable carbon foams [124], [210], [211]. They allow for precise control over the emulsion droplets used as templates, thereby enhancing control over structural characteristics. Additionally, they maintain a monolithic structure and have the advantage of originating from liquid precursors, enabling them to be shaped into virtually any form. By subjecting polyHIPEs to carbonization, emulsion-templated carbon foams, referred to as carboHIPEs, can be created. [211], [212], [213].

Various carbon precursors derived from polyHIPEs have been reported, including lignin [214], polyacrylonitrile [215], resorcinol-formaldehyde [216], and tannins [217]. So far, extensive investigations have focused on styrene-co-divinylbenzene (ST-co-DVB) copolymers and DVB-based polymers for creating porous carbons through emulsion templating followed by pyrolysis [124], [189], [212], [213], [218], [219], [220], [221], [222], [223], [224]. Nonetheless, to fabricate carboHIPEs from ST-co-DVB / DVB-based polyHIPEs, additional stabilization is required due to their relatively limited thermal stability [225].

Broadening the scope of porous materials can be achieved through the fabrication of inherently porous complex structures using polyHIPEs. The combination of additive manufacturing and emulsion templating opens up opportunities for creating inherently porous materials in intricate forms with hierarchical porosity. Among various additive manufacturing (AM) techniques, vat photopolymerization stands out for its ability to directly fabricate 3D intricate structures from design files with minimal effort. Recently, a polymer resin with inherent porosity through emulsion templating was developed in our group [65], [66], [69], and we have reported its use as a resin for vat photopolymerization based commercial 3D printers [71]. Additionally, in a previous study, we successfully demonstrated the creation of intricate hierarchical porous architectural designs using HIPEs through additive manufacturing [72]. This approach enables the utilization of PolyHIPEs as templates for creating inherently porous carbon lattice structures.

In this study, we employed a surfactant-stabilized water-in-oil emulsion, based on 2-ethylhexyl-acrylate and isobornyl-acrylate, as a 3D printing resin. This resin was utilized to produce polyHIPE lattices with three distinct porosities (80%, 85%, and 87.5%) via vat photopolymerization-based 3D printing using an Elegoo Saturn 2 8K 3D printer. Following this, inherently porous lattice-shaped polyHIPEs were subjected to pyrolysis at various

processing temperatures (500ºC, 600ºC, 700ºC, and 800ºC). The macrostructure of the bare polyHIPEs remained intact after pyrolysis. Subsequently, we conducted a detailed characterization of the resulting carboHIPEs derived from the acrylate-based polyHIPEs. Finally, the mechanical properties of the carboHIPEs fabricated under different conditions were assessed.

4.2. Experimental

4.2.1. Materials

2-ethylhexyl acrylate (EHA), isobornyl acrylate (IBOA), trimethylolpropane triacrylate (TMPTA), a photoinitiator; diphenyl (2,4,6- trimethyl benzoyl)-phosphine oxide/2-hydroxy-2-methyl propiophenone (blend), beta carotene (synthetic, ≥93% (UV), powder), and tartrazine (dye content ≥85 %) were all purchased from Sigma Aldrich. The surfactant Hypermer B246-SO-M was received from Croda.

4.2.2. Preparation of High Internal Phase Emulsions

A continuous organic phase was prepared by mixing 39.70 wt% of 2-ethylhexyl acrylate (EHA), 39.70 wt% of isobornyl acrylate (IBOA), 15.90 wt% of trimethylolpropane triacrylate (TMPTA) as the crosslinker, and 4.70 wt% of Hypermer B246-SO-M as the surfactant (Table A20). To dissolve the surfactant completely, the mixture was heated to 50°C. Beta-carotene and tartrazine, previously reported in our prior research, were incorporated at concentrations of 0.02 wt% and 0.06 wt%, respectively, within the continuous organic phase, as light-absorbers. [71]. The photoinitiator was then added at 5 wt% into the continuous phase. To create an emulsion, distilled water (dH$_2$O) was added drop by drop while stirring the mixture at 300 rpm using a SciQuip-Pro 40 stirrer. HIPEs were prepared using 80 vol.%, 85 vol.%, and 87.5 vol.% of dH$_2$O to create polyHIPEs with 3 different porosities.

4.2.3. 3D printing of polyHIPE lattices and cylinders

PolyHIPE structures were manufactured using a commercial 3D printer, the Elegoo Saturn 2 8K, which employs digital light processing technology. This 3D printer is equipped with an 8K monochrome LCD screen boasting a resolution of 7680×4320 pixels and a XY resolution of 28.5 µm [226]. It is further enhanced with a chip-on-board lens combined with integrated UV LED lights and a Fresnel lens, which collaboratively provide a consistent 405 nm light source for printing. The Fresnel collimating light source comprises 48 highly integrated UV LED lights that, in conjunction with the FCL system and Fresnel lens, emit a uniform 405 nm wavelength light, resulting in exceptional printing precision and a smoother surface finish.

The lattice structure consisting of tetrahedral octahedral vertex centroid unit cell configuration (to be mentioned as "lattice structure" or "lattice" in the text) was obtained from thingiverse.com [180]. Autodesk Fusion 360 was used to add a base to the lattice structure (Figure A9) and prepare cylinders having 25 mm diameter $\times$ 12.5 mm height were prepared. Both designs were formatted as .stl files and then sliced using CHITUBOX Basic.

Cylinders and 24 mm $\times$ 24 mm $\times$ 20 mm lattice structures including 25 mm $\times$ 25 mm $\times$ 3 mm of the base were 3D printed with a layer thickness of 60 µm (Figure 4.1A-C). The pore sizes of the 3D-printed 80%, 85%, and 87.5% porous polyHIPEs were 21.20 ± 6.11 µm, 26.26 ± 7.33 µm, and 34.63 ± 13.15 µm, respectively (Figure A11). The 3D printing parameters including exposure time, bottom layer count, and bottom exposure time etc. were presented in Table A21. It is essential for the initial layers to have a longer exposure time compared to the standard exposure time to ensure proper adhesion of the structures to the printing platform. The entire 3D printing process took approximately 3 hours to produce 15 lattices in a single batch.

Following the completion of the 3D printing process, the printed structures were rinsed with methanol to remove any materials eluting from the polyHIPE, such as uncured resin. They were then placed in an oven at 65ºC for a 24-hour period for drying.

4.2.4. Carbonization of 3D printed polyHIPE lattices and cylinders

The PolyHIPE lattices to produce inherently porous carboHIPE lattices were pyrolyzed under N_2 atmosphere in a high-temperature oven (Elite tube furnace, Elite Furnaces, UK). 4 different processing temperatures, 500°C, 600°C, 700°C, and 800°C were used to investigate the

carbonization mechanism of PolyHIPEs under various temperatures as determined by their TGA analysis, where the decomposition initiates at 500°C (Figure A10). Furthermore, 85% porous 25 mm diameter × 12.5 mm height cylinders were pyrolyzed in the same conditions to investigate the processing temperatures on the mechanical properties of carboHIPEs. The temperature was raised to the processing temperature at a rate of 5°C/min, and it was held at that temperature for a period of 2 hours.

4.3. Characterization

4.3.1. Mercury Intrusion Porosimetry

The degree of porosity and the bulk/skeletal densities of the polyHIPE and carboHIPE lattices were measured using a mercury intrusion porosimeter (AutoPore V, Micrometrics). The highest applied pressure and the contact angle of mercury were 60000 psi (414 MPa) and 130°, respectively.

4.3.2. Scanning Electron Microscopy (SEM)

An FEI Inspect F scanning electron microscope (SEM) was employed to visualize both the macrostructure and microstructure of carboHIPEs. Imaging was performed with an accelerating voltage of 5 kV. Pore sizes were quantified using ImageJ. 70 pores measured from each category and the images used for pore size measurements were presented in supporting information (Figures A11-A14). To address potential underestimation of pore diameters resulting from uneven sectioning, a statistical correction factor $(2/\sqrt{3})$ was applied to the pore size measurements [182].

4.3.3. Raman Spectroscopy

The carboHIPE samples were analyzed by Raman spectroscopy (Renishaw InVia) using a 20 mW, 514.5 nm laser and a 50× objective, between Raman shifts of 100 cm^{-1} and 4000 cm^{-1}. The exposure time was 10 s, with 8 accumulations collected per sample. Baseline correction and data normalization was applied to the spectra in Origin Pro 2023. Additionally, polyHIPE samples were also examined as controls.

4.3.4. X-ray Diffractometer (XRD)

The 85% porous carboHIPE samples were analyzed by XRD using a PANalytical Aeris, operating at the 10 min scan measurement method (Cu tube 30 kV 40 mA, ¼° divergence slit, a 0.15 mm Ni filter, 0.02 Rad soller slits). The measurements were taken over at diffraction angles (2θs) from 0° to 100° with a step size of 0.02°.

4.3.5. Mechanical Testing

Compression testing was performed to evaluate the mechanical properties of the carboHIPE discs (with dimensions of approximately 9 mm in diameter and 4 mm in height after carbonization) (n=3). A Mecmesin Multitest 2.5-dV mechanical testing machine equipped with a 250 N load cell was used at a rate of 1 mm/min. The data were collected using Vector Pro software.

In addition, 25 mm diameter × 12.5 mm height polyHIPE cylinders were tested, and their stiffness was used for comparisons (n=3). Furthermore, compression testing was conducted on 80%, 85%, and 87.5% porous carboHIPE lattice structures fabricated at 800°C (n=4).

4.3.6. Statistical Analysis

Statistical analysis was conducted using Origin Pro 2023. To determine significant differences, one-way ANOVA with Tukey's multiple comparison analysis was employed. Differences were considered significant when the p-value was less than or equal to 0.05. The specific number of replicates used in this study can be found in both the Materials and Methods section and the figure legend.

4.4. Results and Discussion

4.4.1. Examination of the macro- and microstructure of inherently porous carboHIPE lattices

3D-printed inherently porous polyHIPE lattice structures and their respective carboHIPE versions, subjected to various carbonization temperatures, specifically 500°C, 600°C, 700°C,

and 800°C were presented in Figure 4.1. These images provide visual representation and serve as a basis for the examination of these materials as the macrostructure is one of the main focuses in this study. The samples were named according to their nominal porosity (80%, 85%, and 87.5%), representing the internal phase amount used during HIPEs preparation.

Figure 4.1A demonstrated a porous lattice structure exhibiting 80% porosity. Figure 4.1B illustrated lattice structure with an 85% porosity while Figure 4.1C presented the polyHIPE lattice with 87.5% porosity. The carboHIPEs derived from 80% polyHIPE lattices at 500°C, 600°C, 700°C, and 800°C, were displayed in Figure 4.1D, G, J, M, respectively. Similarly, 85% porous carboHIPEs pyrolyzed at 500°C, 600°C, 700°C, and 800°C were presented in Figure 4.1E, H, K, N, respectively. Likewise, Figure 4.1F, I, L, O exhibited 87.5% porous carboHIPEs pyrolyzed at 500°C, 600°C, 700°C, and 800°C, respectively. This comprehensive collection of images, labeled from Figure 4.1D-O, provides insight into the alterations of the porous lattice structures resulting from different carbonization temperatures.
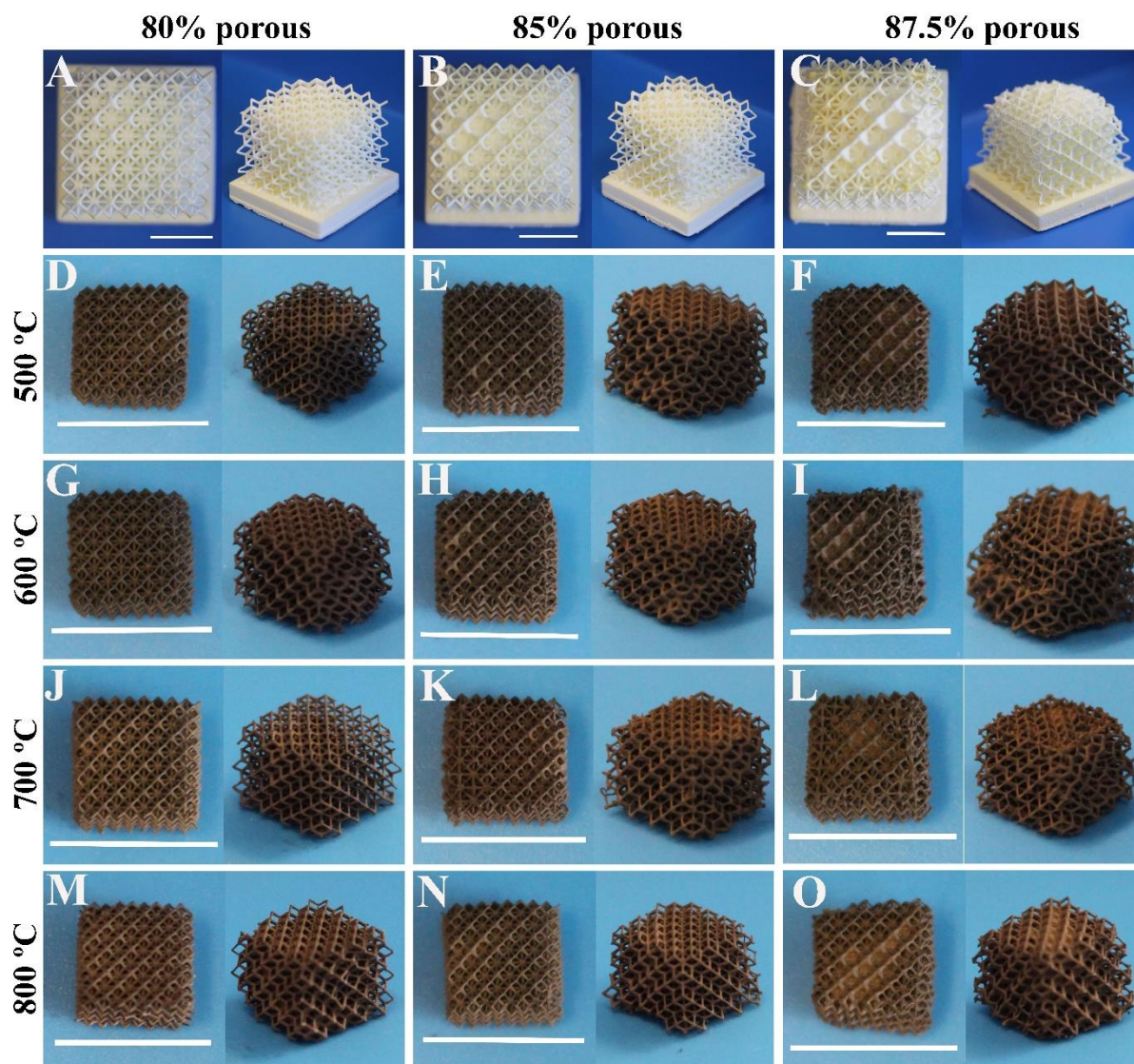
Figure 4.1. Digital images of 3D-printed polyHIPE and carboHIPE lattices fabricated from various perspectives. 80% inherently porous **(A)** polyHIPE lattices and carboHIPE lattices pyrolyzed at **(D)** 500℃, **(G)** 600℃, **(J)** 700℃, and **(M)** 800℃. 85% inherently porous **(B)** polyHIPE lattices and carboHIPE lattices pyrolyzed at **(E)** 500℃, **(H)** 600℃, **(K)** 700℃, and **(N)** 800℃. 87.5% inherently porous **(C)** polyHIPE and carboHIPE lattices pyrolyzed at **(F)** 500℃, **(I)** 600℃, **(L)** 700℃, and **(O)** 800℃. Scale bars are 10 mm in all images.

In addition to the visual inspection of shrinkage, the quantified data calculated shrinkage rates were presented in Table 4.1. The data in this table supplements the visuals in Figure 4.1, providing a deeper insight into how the material behaves and changes during pyrolysis.

Table 4.1. Porosity (%), Density (g/cm^3), Shrinkage (vol. %), and Pore size (µm) values of the 80%, 85%, and 87.5% porous polyHIPE lattices and carboHIPE lattices fabricated at 500ºC, 600ºC, 700ºC, and 800ºC.

Samples		Porosity (%)	Density (g/cm^3)		Shrinkage (vol. %)	Pore size (µm)
			Bulk	Skeletal		
80 % porous	polyHIPE	64.02	0.36	1.01	n/a	21.20 ± 6.11
	500ºC	75.09	0.48	1.28	97.19 ± 0.10	15.12 ± 5.12
	600ºC	59.13	0.41	1.47	97.39 ± 0.06	15.24 ± 5.14
	700ºC	70.59	0.34	1.58	97.60 ± 0.03	16.63 ± 5.56
	800ºC	68.61	0.19	0.60	97.47 ± 0.04	14.47 ± 4.50
85 % porous	polyHIPE	76.96	0.22	0.97	n/a	26.26 ± 7.33
	500ºC	59.89	0.35	0.87	97.44 ± 0.04	14.66 ± 5.06
	600ºC	74.45	0.25	0.98	97.39 ± 0.07	13.91 ± 4.56
	700ºC	64.09	0.26	0.71	97.54 ± 0.02	12.49 ± 3.56
	800ºC	79.43	0.14	0.68	97.70 ± 0.03	13.12 ± 3.65
87.5 % porous	polyHIPE	65.92	0.17	0.50	n/a	34.63 ± 13.15
	500ºC	55.38	0.22	0.50	97.37 ± 0.08	13.04 ± 3.27
	600ºC	73.48	0.24	0.89	97.19 ± 0.09	12.07 ± 2.98
	700ºC	69.98	0.25	0.82	97.69 ± 0.01	12.21 ± 3.40
	800ºC	71.04	0.14	0.48	97.19 ± 0.03	11.66 ± 2.82

The volumetric shrinkage in all examined conditions is approximately 97%. Interestingly, despite this significant shrinkage, the macrostructure was maintained during isotropic contraction, preserving the integrity of the 3D strut network. Neither the degree of porosity nor the pyrolysis temperature exhibited a difference in the shrinkage behavior. Based on their standard deviations, a remarkable consistency in the shrinkage process is observed in all experimental conditions.

Nevertheless, some distortion was observed in the 87.5% porous carboHIPEs. This distortion primarily arises from the lower printing resolution, attributed to the high amount of internal phase content (with a 1:7 ratio of external to internal phase), in contrast to the other two porosities. The 80% porous carboHIPEs feature a 1:4 ratio of external to internal phase, while the 85% porous carboHIPEs employ a 1:5.67 ratio of external to internal phase. Furthermore, some instances of overcuring were noted in the 85% and 87.5% porous 3D-printed polyHIPEs.

In the previous research, it was successfully demonstrated that the cubic vertex centroid lattice structure could be 3D printed without encountering overcuring issues by employing 80% porous HIPEs [72]. As the internal phase ratio increases, the printing resolution decreases, as illustrated in Figure 4.1A-C. When compared to 80% porous polyHIPE lattice, some overcured parts emerged in 85% and 87.5% porous ones.

Figure 4.2 presented the SEM images of all carboHIPE lattices. Figure 4.2A, D, G, and J demonstrated 80% porous carboHIPEs pyrolyzed at 500°C, 600°C, 700°C, and 800°C, respectively. Similarly, 85% porous carboHIPEs pyrolyzed at the same temperatures were illustrated in Figures 4.2B, E, H, and K, while Figure 4.2C, F, I, and L exhibited 87.5% porous carboHIPEs fabricated under the same temperature conditions. Notably, there were no observable distortions in the SEM images, providing evidence that the distortion observed in the 87.5% porous lattices (Figure 4.1F, I, L, and O) is due to their lower 3D printing resolution. Furthermore, detailed views of the unit cells and the porous structure of the carboHIPE lattices were presented in the insets.
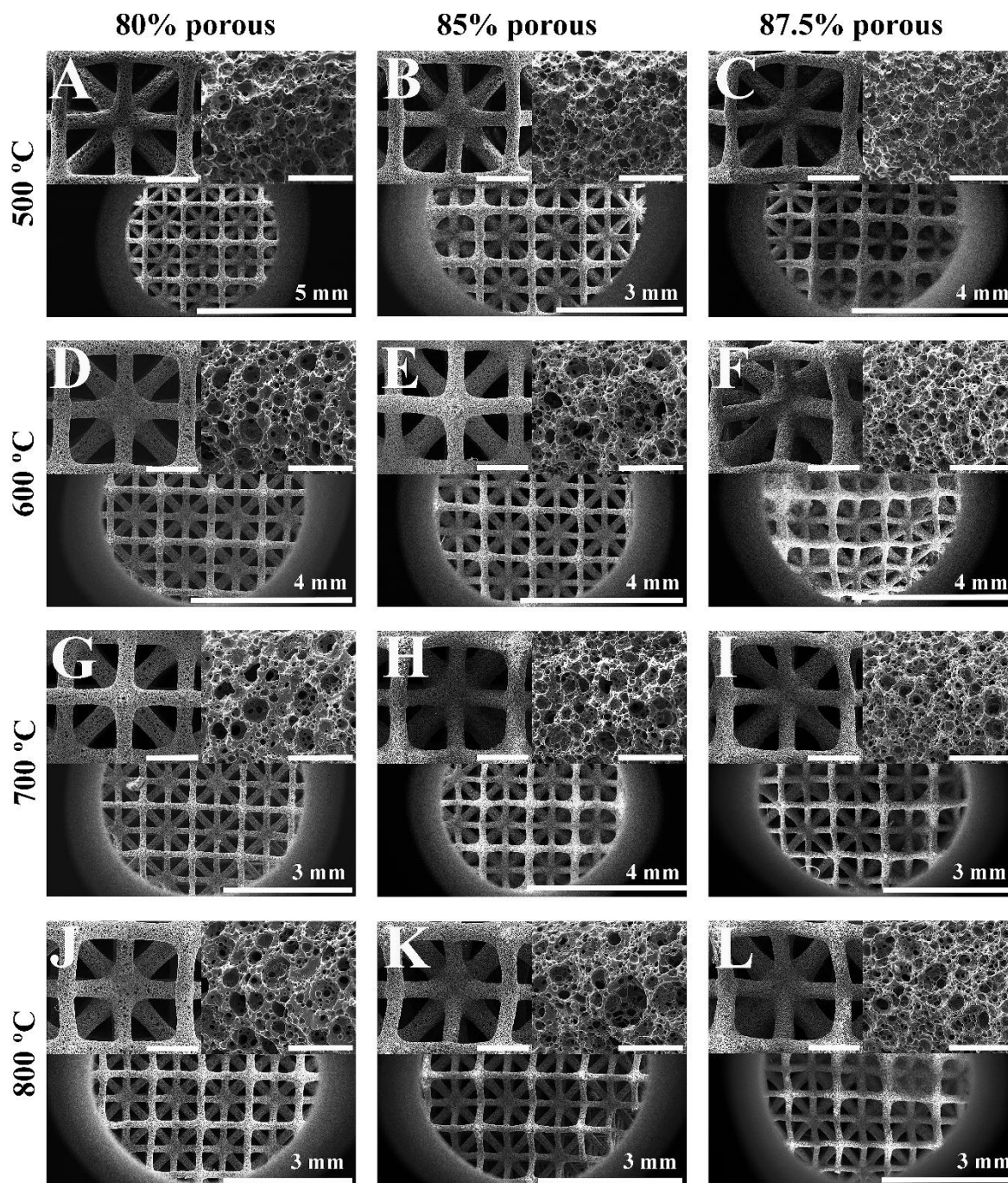
Figure 4.2. SEM images of carboHIPE lattices at various magnifications. 80% inherently porous carboHIPE lattices pyrolyzed at **(A)** 500ºC, **(D)** 600ºC, **(G)** 700ºC, and **(J)** 800ºC. 85% inherently porous carboHIPE lattices pyrolyzed at **(B)** 500ºC, **(E)** 600ºC, **(H)** 700ºC, and **(K)** 800ºC. 87.5% inherently porous carboHIPE lattices pyrolyzed at **(C)** 500ºC, **(F)** 600ºC, **(I)** 700ºC, and **(L)** 800ºC. Scale bars are 50 µm in the right insets and 500 µm in the left insets.

The pore sizes measure 21.20 ± 6.11 µm, 26.26 ± 7.33 µm, and 34.63 ± 13.15 µm in 80% , 85%, 87.5% porous polyHIPEs. More porous polyHIPEs exhibited larger pores. The pore sizes of carboHIPEs range between 11.66 and 16.63 µm, with higher porous samples exhibiting more shrinkage in the pores. Additionally, the degree of porosity stands at ~64.02% in 80% porous polyHIPEs, ~76.96 % in 85% porous polyHIPEs, and ~65.92% in 87.5% porous polyHIPEs. Interestingly, a notable difference exists between nominal porosity and measured porosity, which can be attributed to the decreasing stability of HIPEs during the 3D printing process [71]. On the other hand, the porosity of the carboHIPEs is between 59.13 and 75.09% in 80% porous carboHIPEs, 59.89 and 79.43% in 85% porous carboHIPEs and 55.38 and 73.48% in 87.5% porous carboHIPEs. Furthermore, there is no significant difference in porosity between polyHIPEs and carboHIPEs, indicating that porosity remains consistent throughout the pyrolysis process. In addition, bulk densities of polyHIPEs and carboHIPEs range from 0.14 to 0.48 g cm^{-3}. While there is no direct correlation between density and pyrolysis temperature, it is noteworthy that the highest temperature resulted in the lowest density. As expected, a higher degree of porosity led to lower density, as indicated in Table 4.1.

4.4.2. Carbonization mechanism of acrylate-based polyHIPEs

To investigate the degree of graphitization of carboHIPEs, Raman spectra analyses were performed, and the corresponding data for 80%, 85%, and 87% porous carboHIPEs were presented in Figure 4.3A, B, and C respectively. All samples demonstrated characteristic D and G bands at ~1349 cm^{-1} and ~1599 cm^{-1}, respectively. These peaks are indicative of the production of pyrolytic carbon and indicate the success of carbonization (Figure A15). It was observed that, with the increase in the pyrolysis temperature, the intensity ratios of D and G exhibited an increase across all three distinct porosities (from ~0.6 to ~0.80). This is associated with the relatively lower carbonization temperature. During pyrolysis, the D/G ratio increases with the processing temperature until graphitization initiates at higher temperatures, and during graphitization, the D/G ratio decreases [228]. On the other hand, carboHIPEs which are derived from styrene-co-divinylbenzene (ST-co-DVB)-based polyHIPEs at 800 ℃ exhibited higher D/G ratios (~0.9 - ~1.00) in the literature [189], [224]. Furthermore, as anticipated, although

porosity did not have a significant influence on these observed trends, the highest porous samples displayed the lowest D/G ratios.
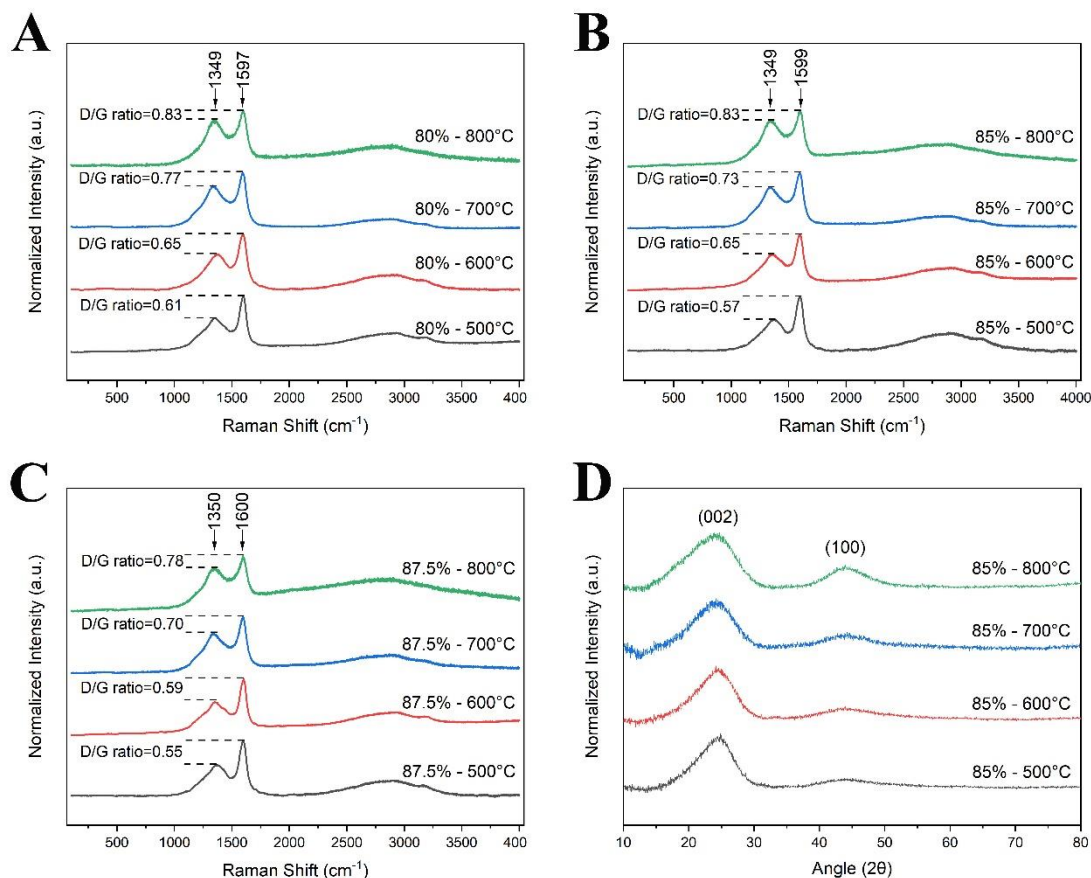
Figure 4.3. Raman spectra of **(A)** 80%, **(B)** 85%, and **(C)** 87.5% porous carboHIPEs and **(D)** XRD analysis of 85% porous carboHIPEs fabricated at 500ºC, 600ºC, 700ºC, and 800ºC.

To validate the carbon structure, XRD analysis was conducted on 85% porous carboHIPE samples manufactured at 500ºC, 600ºC, 700ºC, and 800ºC. The corresponding data was illustrated in Figure 4.3D. The obtained XRD pattern exhibits characteristic peaks at 24º and 44º, corresponding to the (002) and (100) diffraction modes of pyrolytic carbon, respectively [229]. In addition, the difference in the peak positions compared to those of polyHIPE serves as evidence of successful carbonization (Figure A15).

4.4.3. Mechanical Properties of carboHIPEs

The final analysis aimed to assess the mechanical properties of carboHIPEs. Initially, to examine the impact of pyrolysis temperature on the mechanical properties, 85% porous carboHIPE discs fabricated at 500°C, 600°C, 700°C, and 800°C were mechanically tested via compression. As observed in Figure 4.4A-D structural cracks sometimes emerged in the carboHIPE cylinders during the pyrolysis process due to shrinkage contrary to carboHIPE lattices. The representative stress-strain curve and a graph illustrating the statistical differences between the categories were presented in Figure 4.4E. As expected, the polyHIPE samples exhibited the lowest stiffness (0.62 ± 0.02 MPa), with Young's modulus increasing by 7 to 10 times in carboHIPEs (from 4.62 ± 0.06 to 6.25 ± 0.75 MPa). Although the Young's modulus rises with processing temperature, no statistically significant difference was observed beyond 500°C.

Based on the initial compression testing results and Raman spectra, carboHIPE lattices with 80%, 85%, and 87.5% porous configurations were fabricated at 800°C for a detailed investigation into their mechanical properties.

The representative stress-strain curve and specific strength and modulus values of the lattice structures were presented in Figure 4.4F-G, respectively. Young's modulus was determined by analyzing the gradient up to the first peak, and for specific strength calculations, the maximum stress at the first peak was utilized [230]. To calculate the specific strength and modulus, first, the densities of each lattice were calculated based on their volumes, which were derived from the outer dimensions of the lattices.

According to the results, the carboHIPE lattices with 80% and 87.5% porosity demonstrated Young's modulus values of 1.25 ± 0.30 MPa and 1.15 ± 0.21 MPa respectively, while the carboHIPE lattices with 85% porosity exhibited the highest Young's modulus (1.28 ± 0.43 MPa). Similarly, the 85% porous carboHIPE lattices had the highest specific modulus (10.17 ± 3.41 MPa g^{-1} cm^3). In contrast, the carboHIPE lattices with 80% and 87.5% porosity showed similar specific modulus values, 8.03 ± 1.92 and 8.03 ± 1.55 MPa g^{-1} cm^3, respectively. Furthermore, the carboHIPE lattices with 80%, 85%, and 87.5% porosity exhibited specific strengths of 1.06 ± 0.55, 1.07 ± 0.69, and 0.73 ± 0.41 MPa g^{-1} cm^3, respectively. In addition,

the 85% and 87.5% porous categories exhibited fewer sharp peaks and downs in their stress/strain graphs compared to 80% porous lattices (Figure A16).

In comparison to carboHIPE discs, as expected, carboHIPE lattices exhibited lower Young's modulus due to their thin and brittle strut structure, in contrast to the monolithic disc structure. Additionally, the Ashby diagram, comparing this work against other materials, showed that they fall into the foams category (Figure A17).
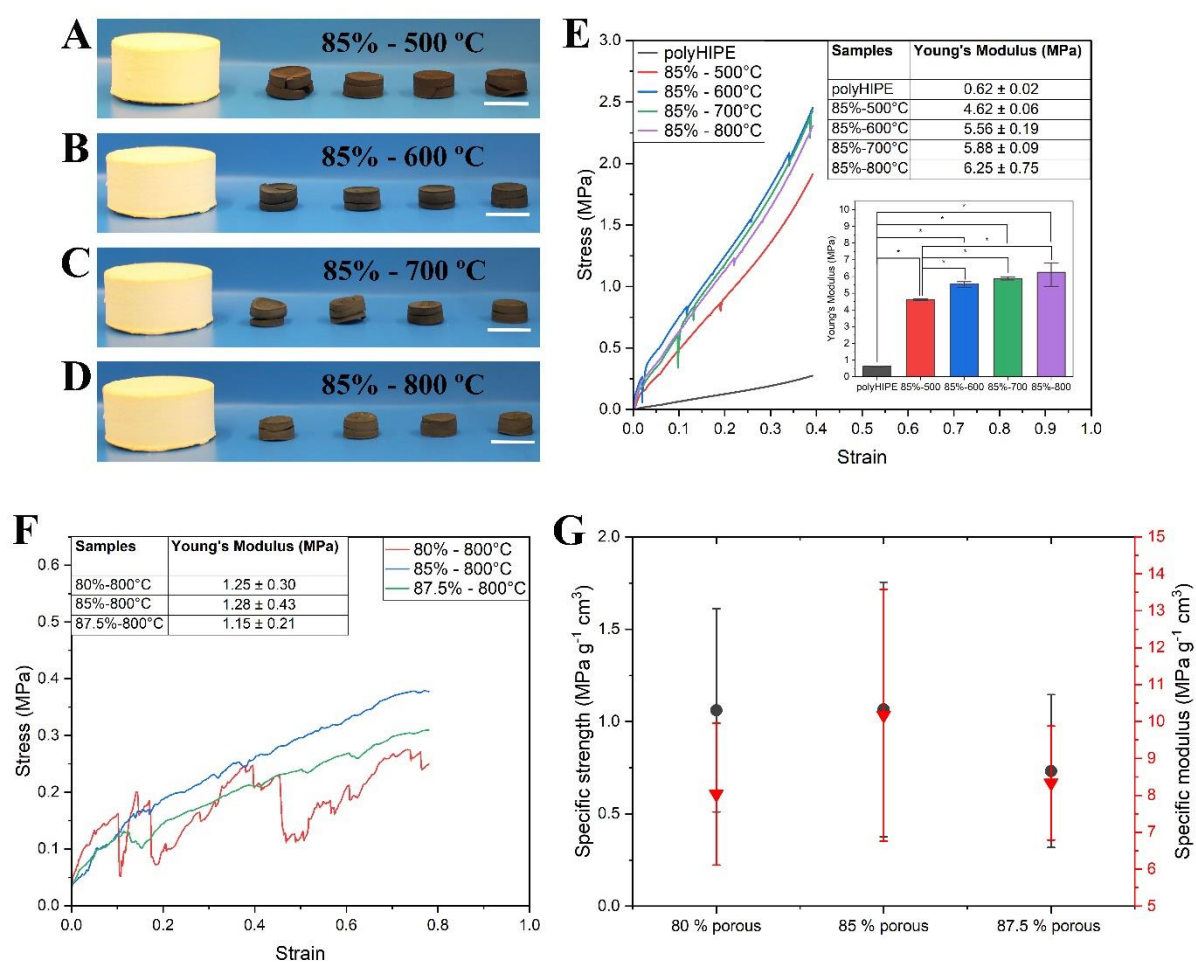
Figure 4.4. Digital photos of 85% porous polyHIPE cylinders and carboHIPE discs fabricated at **(A)** 500ºC, **(B)** 600ºC, **(C)** 700ºC, and **(D)** 800ºC. Scale bars are 10 mm in A-D. **(E)** Compression testing results of 85% porous carboHIPE discs (*: $p \leq 0.05$) (n=3). **(F)** Compression testing results and representative stress-strain curves of 80%, 85%, and 87.5% porous carboHIPE lattices pyrolyzed at 800ºC (n=4). **(G)** Specific strength and modulus values of 80%, 85%, and 87.5% porous carboHIPE lattices pyrolyzed at 800ºC.

4.5. Conclusions

In conclusion, this study systematically investigated the macro- and microstructure, shrinkage behavior, pore characteristics, carbonization mechanism, and mechanical properties of 3D-printed inherently porous polyHIPE and carboHIPE lattices. The examination of lattice structures at different carbonization temperatures showed consistent volumetric isotropic contraction. However, distortions were observed in 87.5% porous carboHIPEs due to lower printing resolution due to high internal phase content (1:7 ratio of external to internal phase). Quantified data on shrinkage rates complemented visual inspections, showing approximately 97% volumetric shrinkage with remarkable consistency across all conditions. SEM images displayed well-defined structures with varying pore sizes. Raman spectra indicated successful carbonization, with increasing D/G ratios with increasing carbonization temperatures. XRD analysis further validated the carbon structure. While mechanical testing indicated a higher Young's modulus in carboHIPE discs compared to polyHIPE cylinders, the carboHIPE lattices demonstrated lower Young's modulus compared to monolithic carboHIPE discs. Notably, the 85% porous carboHIPE lattices exhibited the highest Young's modulus and specific modulus values compared to 80% and 87.5% porous carboHIPE lattices.

CHAPTER 5

Overall Conclusions and Future Work

In summary, the use of HIPEs as printing resins and their use to fabricate highly porous complex metal-based and carbon structures were comprehensively investigated in this thesis.

The primary focus of the study was to enhance 3D printing resolution for porous polymer structures by utilizing a blend of beta-carotene and tartrazine as light absorbers to create inherently porous intricate polyHIPE structures. The resulting 3D-printed objects exhibited preserved surface and internal porosity, with a substantial reduction in pore size from approximately 30-40 to 15-20 µm, and an overall porosity of less than 74% leading to the classification of these structures as polyMIPEs rather than polyHIPEs. Notably, this research demonstrated the feasibility of utilizing commercial vat photopolymerization-based setups for 3D printing intricate porous polymer structures, thereby expanding the potential applications of inherently porous polyMIPEs/HIPEs.

The electroless nickel plating of 3D-printed polyHIPE lattice structures was further investigated by optimizing the process to produce highly porous metal-based lattice structures. Successful metal coating of 3D-printed polyHIPE lattice structures was achieved, with the nickel coating remaining intact after the removal of the polyHIPE templates. The heating process in different atmospheres resulted in the formation of distinct compounds, highlighting the versatility of polyHIPE structures as templates for various applications. The study demonstrated the potential of electroless nickel plating in producing porous metallic/metal-based lattice structures with consistent wall thickness.

Concluding with the exploration of inherently carboHIPE lattices derived from 3D-printed polyHIPEs, the research provided a systematic investigation into macro- and microstructures, shrinkage behavior, pore characteristics, carbonization mechanisms, and mechanical properties. In conclusion, this holistic study significantly advances our understanding of the design and performance of porous carbon materials fabricated through the combination of emulsion templating and additive manufacturing techniques.

Looking ahead, to expand the usage of HIPEs as printing resins, various types of materials, including PCL, PGS, and PGS-M, can be used to prepare them. To enhance their suitability as printing resins, optimization is crucial, with a significant focus on improving their stability, particularly given that stability loss is a key issue during the printing process. Moreover, fabricating polyHIPEs with larger pores holds the potential to enhance metal penetration throughout the structure. This can be achieved by employing particle-stabilized HIPEs instead of surfactant-stabilized ones. However, a limitation arises concerning their stability; achieving intricate structures using particle-stabilized HIPEs requires significant efforts to enhance their stability. This thesis, while more centered on the general investigation of the use of HIPEs for vat photopolymerization and their potential for producing highly porous metal-based and carbon structures, opens avenues for future research in the dynamic field of porous materials.

Dear reader, in this extensive research area, many uncharted territories await exploration. If this thesis has sparked your curiosity, I encourage you to chart your path and immerse yourself in the remarkable world of polyHIPEs.

Thank you for accompanying me on this three-year journey.

APPENDIX

Chapter 2 Appendix
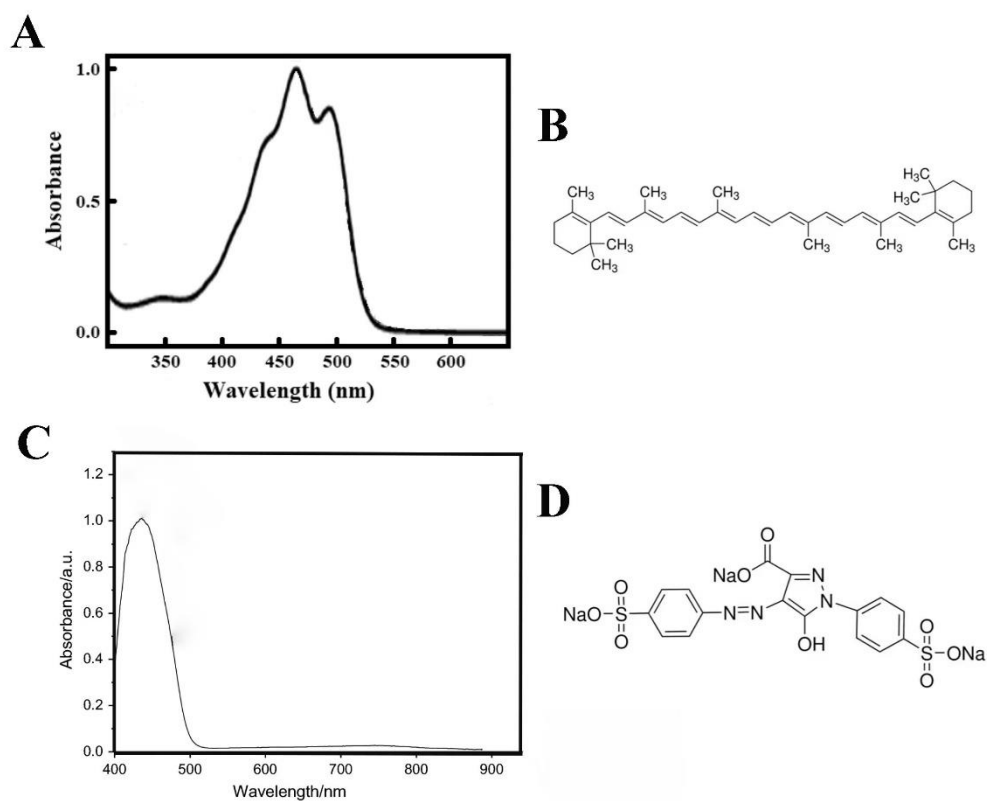
Figure A1. The absorbance spectra and molecular structures of **(A-B)** beta-carotene and **(C-D)** tartrazine. **(A)** adapted from [230] Copyright 2022, **(B)** adapted from [231], **(C)** adapted from [232] Copyright 2018, **(D)** adapted from [233].
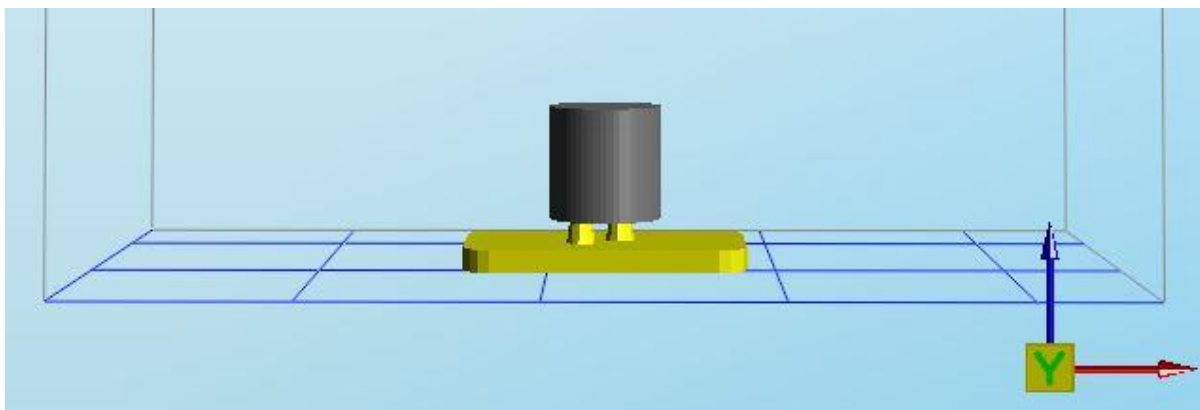
Figure A2. The 3D model of 5×5 mm cylinder

Table A1. Printing parameters to 3D print 5×5 mm cylinders from pure HIPE

From layer	To layer	Exposure time (sec)	Lifting height (mm)	Lifting speed (mm/min)	Down speed (mm/min)	Delay time (sec)
1	1	35	5	10	40	0.3
2	32	27	5	10	40	0.3
33	66	22	5	10	40	0.3
67	125	17	5	15	40	0.3
126	175	13	5	15	40	0.3
176	200	9	5	15	40	0.3
201	225	6	5	15	40	0.3
226	233	4	5	15	40	0.3

Table A2. Printing parameters to 3D print 5×5 mm cylinders from HIPE that contained 0.4% beta-carotene

From layer	To layer	Exposure time (sec)	Lifting height (mm)	Lifting speed (mm/min)	Down speed (mm/min)	Delay time (sec)
1	1	40	5	10	40	0.3
2	32	37	5	10	40	0.3
33	66	35	5	10	40	0.3
67	125	32	5	15	40	0.3
126	175	30	5	15	40	0.3
176	200	25	5	15	40	0.3
201	225	20	5	15	40	0.3
226	233	15	5	15	40	0.3

Table A3. Printing parameters to 3D print 5×5 mm cylinders from HIPE that contained 0.1% tartrazine

From layer	To layer	Exposure time (sec)	Lifting height (mm)	Lifting speed (mm/min)	Down speed (mm/min)	Delay time (sec)
1	1	40	5	10	40	0.3
2	32	39	5	10	40	0.3
33	66	37	5	10	40	0.3

From layer	To layer	Exposure time (sec)	Lifting height (mm)	Lifting speed (mm/min)	Down speed (mm/min)	Delay time (sec)
67	125	34	5	15	40	0.3
126	175	32	5	15	40	0.3
176	200	27	5	15	40	0.3
201	225	22	5	15	40	0.3
226	233	17	5	15	40	0.3

Table A4. Printing parameters to 3D print 5×5 mm cylinders from HIPE that contained blend (0.4% beta-carotene and 0.1% tartrazine)

From layer	To layer	Exposure time (sec)	Lifting height (mm)	Lifting speed (mm/min)	Down speed (mm/min)	Delay time (sec)
1	1	40	5	10	40	0.3
2	32	37	5	10	40	0.3
33	66	35	5	10	40	0.3
67	125	32	5	15	40	0.3
126	175	30	5	15	40	0.3
176	200	25	5	15	40	0.3
201	225	20	5	15	40	0.3
226	233	15	5	15	40	0.3

Figure A3. The 3D model of 5×5 mm cylinders having 15°, 30°, and 45° inclines

Table A5. Printing parameters to 3D print 5×5 mm cylinders having 15°, 30°, and 45° inclines from pure HIPE

From layer	To layer	Exposure time (sec)	Lifting height (mm)	Lifting speed (mm/min)	Down speed (mm/min)	Delay time (sec)
1	1	35	5	10	40	0.3
2	32	27	5	10	40	0.3
33	66	22	5	10	40	0.3
67	125	17	5	15	40	0.3
126	175	13	5	15	40	0.3
176	200	9	5	15	40	0.3
201	225	6	5	15	40	0.3
226	233	4	5	15	40	0.3

Table A6. Printing parameters to 3D print 5×5 mm cylinders having 15°, 30°, and 45° inclines from HIPE that contained 0.4% beta-carotene

From layer	To layer	Exposure time (sec)	Lifting height (mm)	Lifting speed (mm/min)	Down speed (mm/min)	Delay time (sec)
1	1	45	5	10	40	0.3
2	32	40	5	10	40	0.3
33	66	35	5	10	40	0.3
67	125	32	5	15	40	0.3
126	175	28	5	15	40	0.3
176	200	24	5	15	40	0.3
201	225	19	5	15	40	0.3
226	233	15	5	15	40	0.3

Table A7. Printing parameters to 3D print 5×5 mm cylinders having 15°, 30°, and 45° inclines from HIPE that contained 0.1% tartrazine

From layer	To layer	Exposure time (sec)	Lifting height (mm)	Lifting speed (mm/min)	Down speed (mm/min)	Delay time (sec)
1	1	60	5	10	40	0.3
2	76	57	5	10	40	0.3
77	150	55	5	10	40	0.3

| 151 | 225 | 53 | 5 | 15 | 40 | 0.3 |
| 226 | 233 | 50 | 5 | 15 | 40 | 0.3 |

Table A8. Printing parameters to 3D print 5×5 mm cylinders having 15°, 30°, and 45° inclines from HIPE that contained blend (0.4% beta-carotene and 0.1% tartrazine)

From layer	To layer	Exposure time (sec)	Lifting height (mm)	Lifting speed (mm/min)	Down speed (mm/min)	Delay time (sec)
1	1	45	5	10	40	0.3
2	32	42	5	10	40	0.3
33	66	38	5	10	40	0.3
67	125	34	5	15	40	0.3
126	175	29	5	15	40	0.3
176	200	26	5	15	40	0.3
201	225	22	5	15	40	0.3
226	233	18	5	15	40	0.3
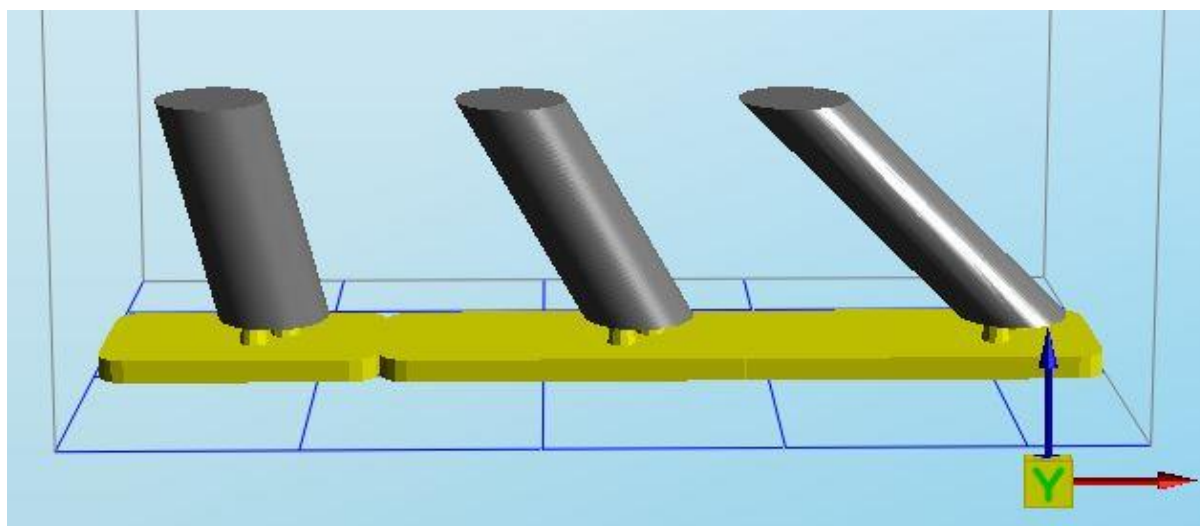
Figure A4. The 3D model of 5×10 mm cylinders having 15°, 30°, and 45° inclines

Table A9. Printing parameters to 3D print 5×10 mm cylinders having 15°, 30°, and 45° inclines from pure HIPE

From layer	To layer	Exposure time (sec)	Lifting height (mm)	Lifting speed (mm/min)	Down speed (mm/min)	Delay time (sec)
1	1	35	5	10	40	0.3
2	32	27	5	10	40	0.3
33	76	22	5	10	40	0.3
77	150	17	5	15	40	0.3
151	225	13	5	15	40	0.3
226	300	9	5	15	40	0.3
301	370	6	5	15	40	0.3
371	411	4	5	15	40	0.3

Table A10. Printing parameters to 3D print 5×5 mm cylinders having 15°, 30°, and 45° inclines from HIPE that contained 0.4% beta-carotene

From layer	To layer	Exposure time (sec)	Lifting height (mm)	Lifting speed (mm/min)	Down speed (mm/min)	Delay time (sec)
1	1	45	5	10	40	0.3
2	32	42	5	10	40	0.3
33	76	38	5	10	40	0.3
77	150	35	5	15	40	0.3
151	225	32	5	15	40	0.3
226	300	28	5	15	40	0.3
301	370	24	5	15	40	0.3
371	411	20	5	15	40	0.3

Table A11. Printing parameters to 3D print 5×5 mm cylinders having 15°, 30°, and 45° inclines from HIPE that contained blend (0.4% beta-carotene and 0.1% tartrazine)

From layer	To layer	Exposure time (sec)	Lifting height (mm)	Lifting speed (mm/min)	Down speed (mm/min)	Delay time (sec)
1	1	45	5	10	40	0.3
2	32	42	5	10	40	0.3
33	76	38	5	10	40	0.3

77	150	35	5	15	40	0.3
151	225	32	5	15	40	0.3
226	300	28	5	15	40	0.3
301	370	24	5	15	40	0.3
371	411	20	5	15	40	0.3

Figure A5. The 3D model of calibration object including 5 mm high posts of 3 mm, 2 mm, 1 mm, and 0.5 mm diameters

Table A12. Printing parameters to 3D print calibration object including 5 mm high posts of 3 mm, 2 mm, 1 mm, and 0.5 mm diameters from pure HIPE

From layer	To layer	Exposure time (sec)	Lifting height (mm)	Lifting speed (mm/min)	Down speed (mm/min)	Delay time (sec)
1	1	35	5	10	40	0.3
2	32	27	5	10	40	0.3
33	64	22	5	10	40	0.3

65	100	17	5	15	40	0.3
101	125	13	5	15	40	0.3
126	150	9	5	15	40	0.3
151	163	6	5	15	40	0.3

Table A13. Printing parameters to 3D print calibration object including 5 mm high posts of 3 mm, 2 mm, 1 mm, and 0.5 mm diameters from HIPE that contained 0.4% beta-carotene

From layer	To layer	Exposure time (sec)	Lifting height (mm)	Lifting speed (mm/min)	Down speed (mm/min)	Delay time (sec)
1	1	40	5	10	40	0.3
2	32	37	5	10	40	0.3
33	64	35	5	10	40	0.3
65	100	32	5	15	40	0.3
101	125	30	5	15	40	0.3
126	150	25	5	15	40	0.3
151	163	20	5	15	40	0.3

Table A14. Printing parameters to 3D print calibration object including 5 mm high posts of 3 mm, 2 mm, 1 mm, and 0.5 mm diameters from HIPE that contained 0.1% tartrazine

From layer	To layer	Exposure time (sec)	Lifting height (mm)	Lifting speed (mm/min)	Down speed (mm/min)	Delay time (sec)
1	1	42	5	10	40	0.3
2	32	39	5	10	40	0.3
33	64	37	5	10	40	0.3
65	100	34	5	15	40	0.3
101	125	32	5	15	40	0.3
126	150	27	5	15	40	0.3
151	163	22	5	15	40	0.3

Table A15. Printing parameters to 3D print calibration object including 5 mm high posts of 3 mm, 2 mm, 1 mm, and 0.5 mm diameters from HIPE that contained blend (0.4% beta-carotene and 0.1% tartrazine)

From layer	To layer	Exposure time (sec)	Lifting height (mm)	Lifting speed (mm/min)	Down speed (mm/min)	Delay time (sec)
1	1	40	5	10	40	0.3
2	32	37	5	10	40	0.3
33	64	35	5	10	40	0.3
65	100	32	5	15	40	0.3
101	125	30	5	15	40	0.3

| 126 | 150 | 25 | 5 | 15 | 40 | 0.3 |
| 151 | 163 | 20 | 5 | 15 | 40 | 0.3 |

Figure A6. The 3D model of pyramid structure

Table A16. *Printing parameters to 3D print pyramid structure from pure HIPE that contained blend (0.4% beta-carotene and 0.1% tartrazine)*

From layer	To layer	Exposure time (sec)	Lifting height (mm)	Lifting speed (mm/min)	Down speed (mm/min)	Delay time (sec)
1	1	40	5	10	40	0.3
2	32	37	5	10	40	0.3
33	66	35	5	10	40	0.3
67	125	32	5	15	40	0.3
126	200	30	5	15	40	0.3

201	275	25	5	15	40	0.3
276	310	20	5	15	40	0.3
311	341	15	5	15	40	0.3
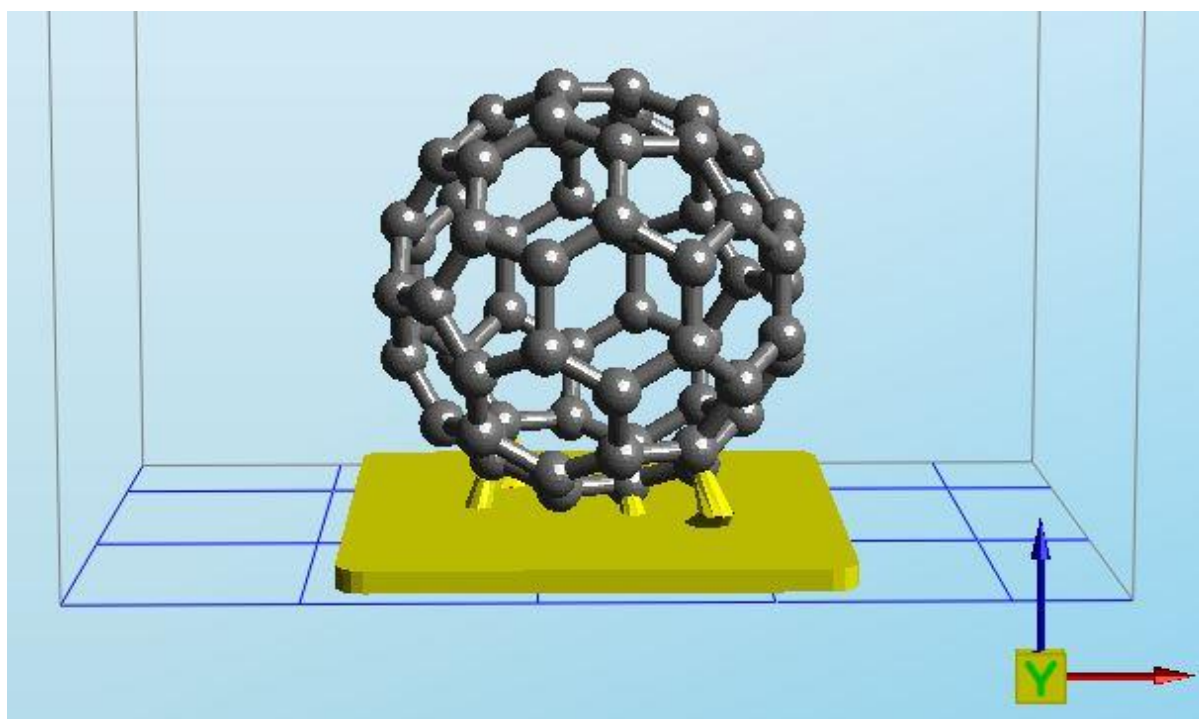
Figure A7. The 3D model of buckyball structure

Table A17. Printing parameters to 3D print buckyball structure from pure HIPE that contained blend (0.4% beta-carotene and 0.1% tartrazine)

From layer	To layer	Exposure time (sec)	Lifting height (mm)	Lifting speed (mm/min)	Down speed	Delay time
1	1	50	5	10	40	0.3
2	32	47	5	10	40	0.3

33	66	43	5	10	40	0.3
67	250	40	5	10	40	0.3
251	350	37	5	10	40	0.3
351	420	33	5	10	40	0.3
421	500	29	5	10	40	0.3
501	570	25	5	15	40	0.3
571	600	22	5	15	40	0.3
601	680	20	5	15	40	0.3
681	712	17	5	15	40	0.3

Table A18. Print times of 3D model for each HIPE category

3D model	Print time (pure)	Print time (0.4% beta-carotene)	Print time (0.1% tartrazine)	Print time (blend)
5×5 mm cylinders	2 h 59 min	3 h 55 min	4 h 2 min	3 h 55 min
5×5 mm cylinders having 15°, 30°, and 45° inclines	2 h 59 min	3 h 55 min	3 h 35 min	4 h 2 min
5×10 mm cylinders				

having 15°, 30°, and 45° inclines	4 h 55 min	6 h 55 min	9 h 5 min	6 h 55 min
Calibration object	2 h 13 min	2 h 52 min	2 h 57 min	2 h 52 min
Pyramid	-	-	-	5 h 27 min
Buckyball	-	-	-	13 h 19 min
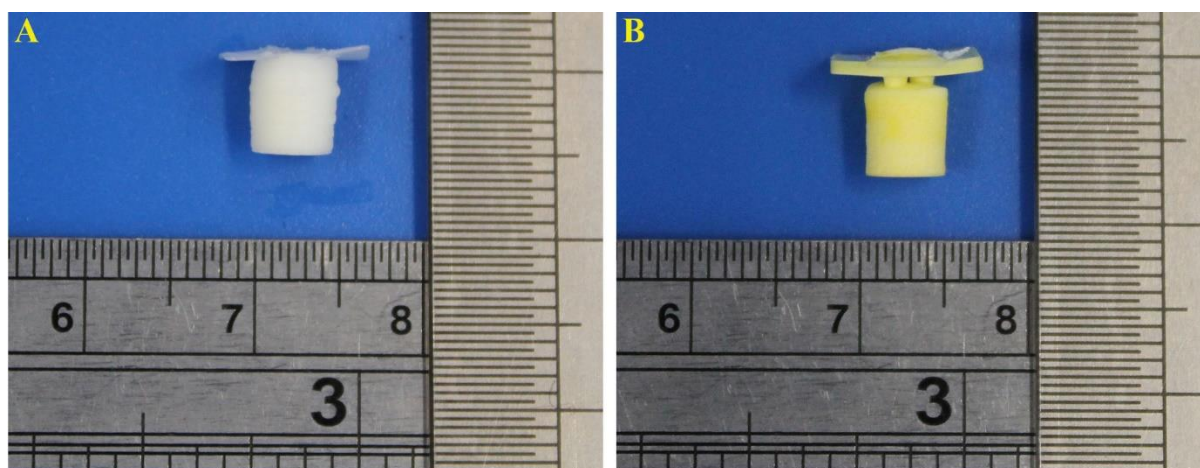
Figure A8. The comparison of the **(A)** pure and **(B)** blend samples in terms of overcuring

Table A19. Diameter and height values of the pure and blend samples before and after drying

Samples	Before drying		After drying	
	d (mm)	h (mm)	d (mm)	h (mm)
Pure	4.78 ± 0.11	5.17 ± 0.04	4.67 ± 0.18	4.94 ± 0.12
Blend	4.82 ± 0.09	4.93 ± 0.04	4.72 ± 0.06	4.86 ± 0.06

Chapter 4 Appendix

Table A20. EHA, IBOA, TMPTA, hypermer, beta-carotene, and tartrazine ratio (wt%)

Organic phase				Light absorbers	
EHA *(wt%)*	*IBOA* *(wt%)*	*TMPTA* *(wt%)*	*Hypermer* *(wt%)*	*Beta-carotene[a]* *(wt%)*	Tartrazine[a] *(wt%)*
39.70	39.70	15.90	4.70	0.02	0.06

[a]Beta-carotene and tartrazine concentration with respect to the organic phase

Figure A9. 3D designs of **(A)** tetrahedral octahedral vertex centroid lattice from different perspectives and **(B)** the cylinder with 50 mm diameter × 25 mm height.

Table A21. 3D printing parameters used to produce discs and lattices

Layer height (µm)	Bottom layer count	Exposure time (sec)		Bottom exposure time (sec)	Transition layer count
		lattices	discs		
60	10	10	8	40	8
Bottom lift distance/Lifting distance (mm)	**Rest time before/after lift (sec)**	**Rest time after retract (sec)**		**Bottom lift speed/Lifting speed (mm/min)**	**Bottom retract speed/Retract speed (mm/min)**
3	0	0.5		65	180
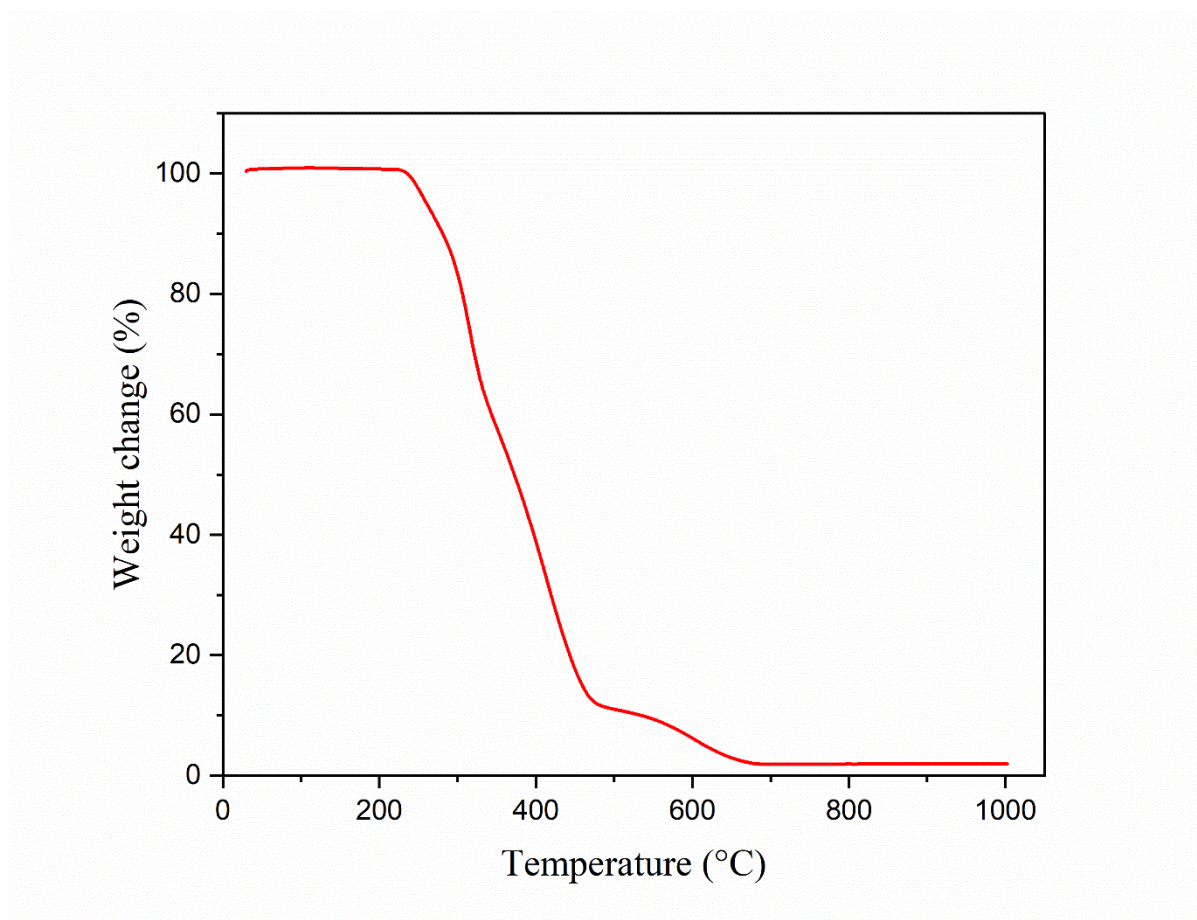
Figure A10. The TGA curve of the 80% porous polyHIPE, which were prepared from the materials presented in Table A20.
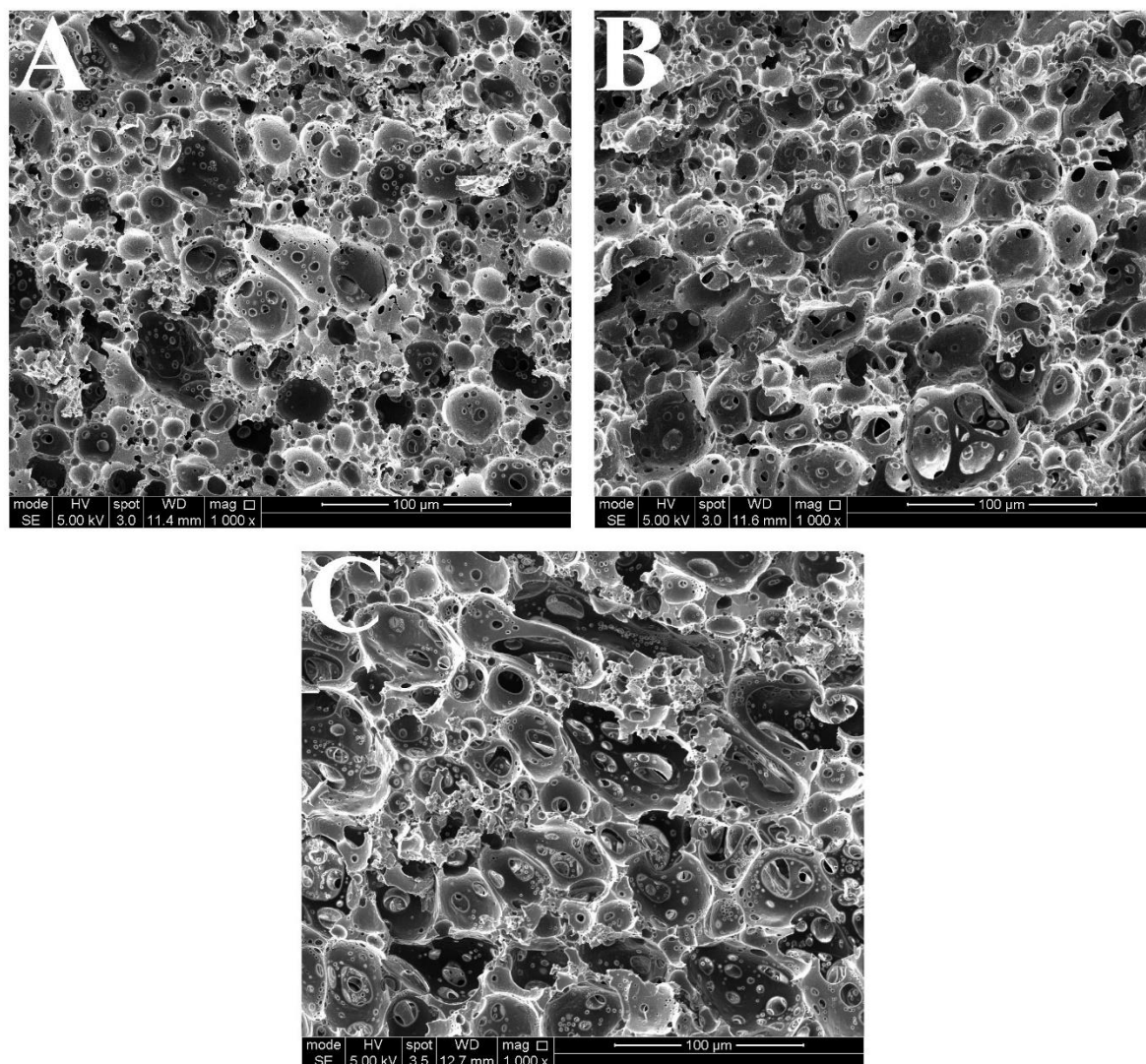
Figure A11. The SEM images of **(A)** 80%, **(B)** 85%, and **(C)** 87.5% porous polyHIPEs, which were used to measure pore sizes.
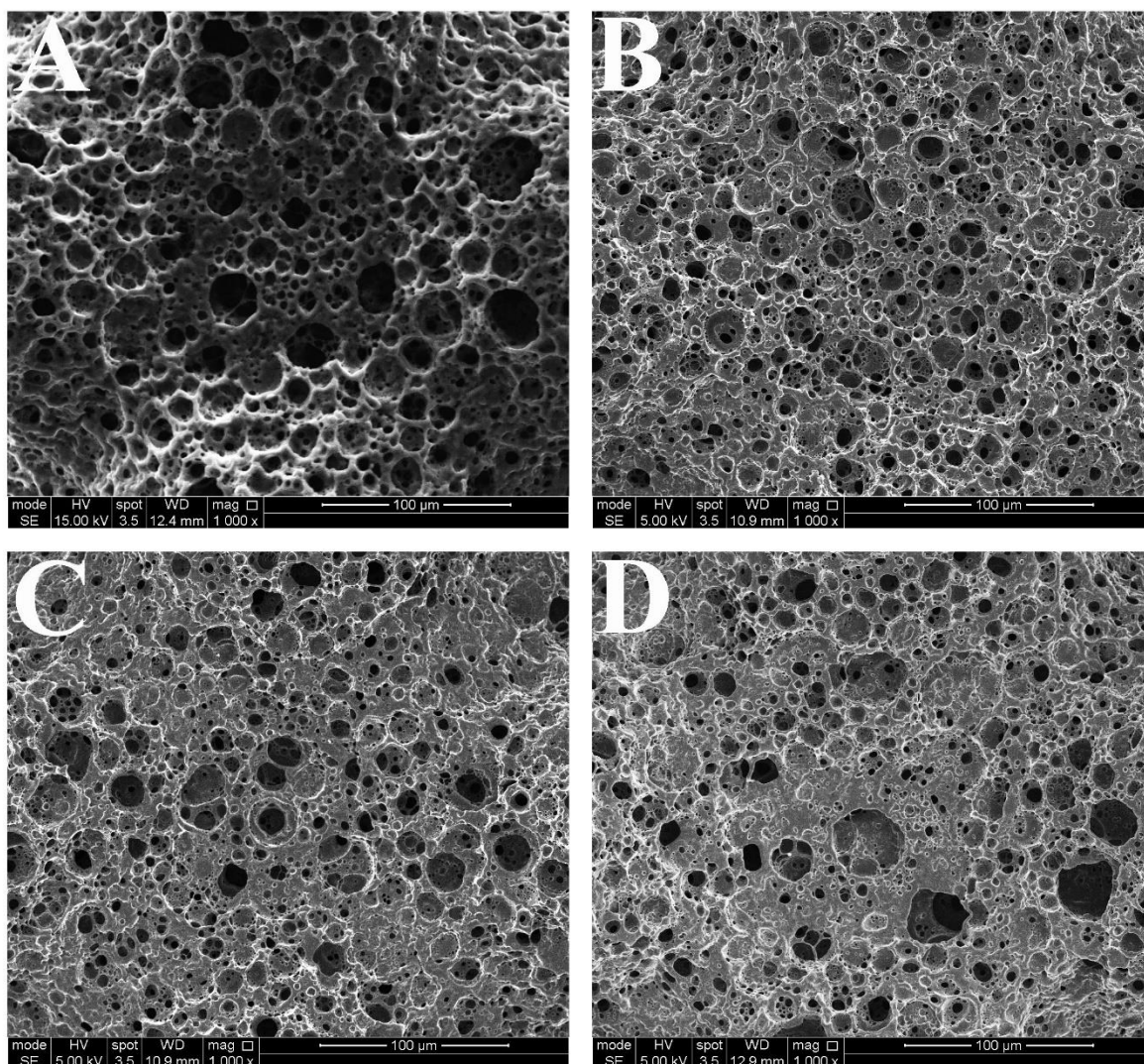
Figure A12. The SEM images of 80% porous carboHIPEs fabricated at **(A)** 500 ºC, **(B)** 600 ºC, **(C)** 700 ºC, and **(D)** 800 ºC, which were used to measure pore sizes.
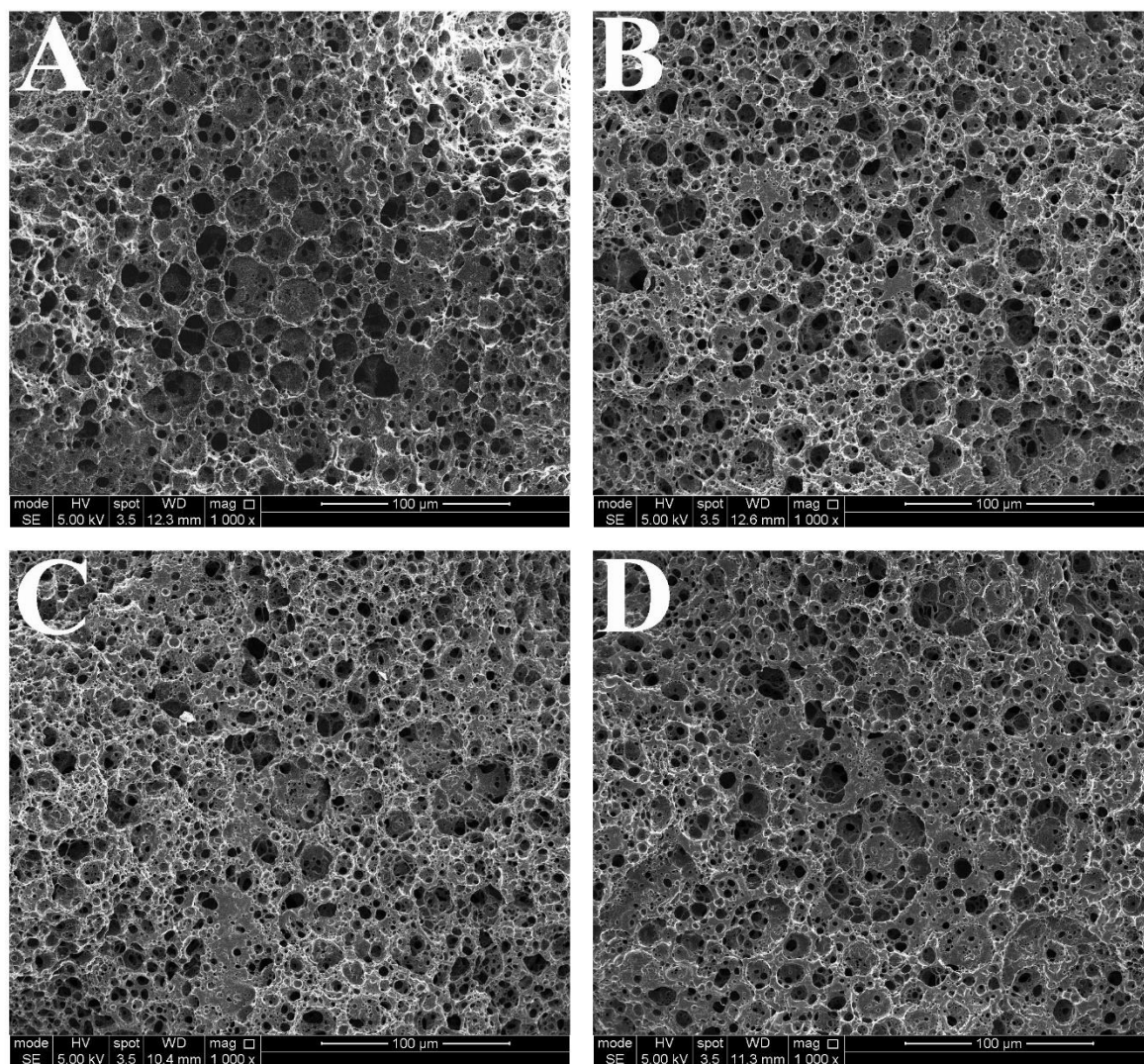
Figure A13. The SEM images of 85% porous carboHIPEs fabricated at **(A)** 500 ºC, **(B)** 600 ºC, **(C)** 700 ºC, and **(D)** 800 ºC, which were used to measure pore sizes.
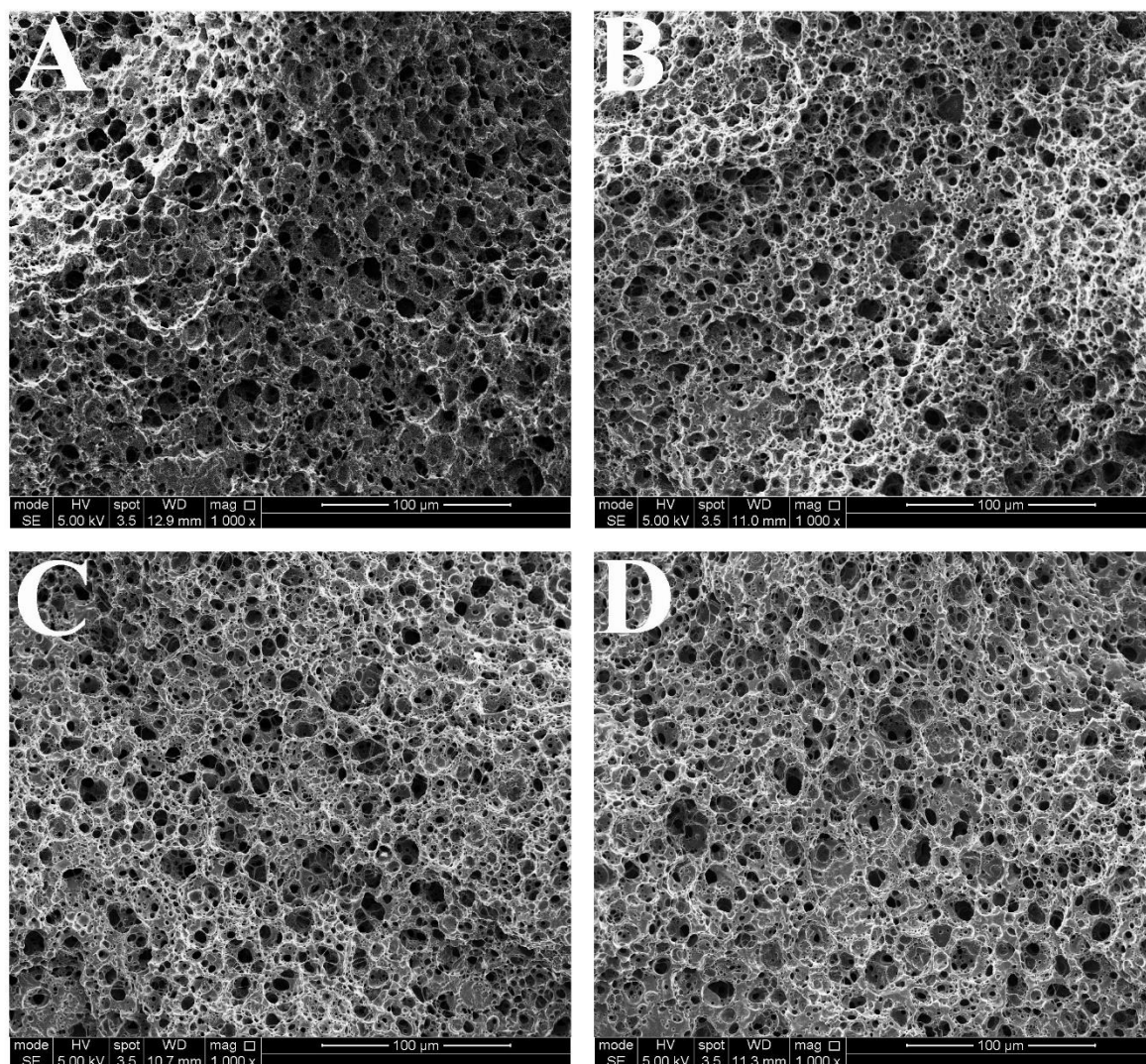
Figure A14. The SEM images of 87.5% porous carboHIPEs fabricated at **(A)** 500 ℃, **(B)** 600 ℃, **(C)** 700 ℃, and **(D)** 800 ℃, which were used to measure pore sizes.
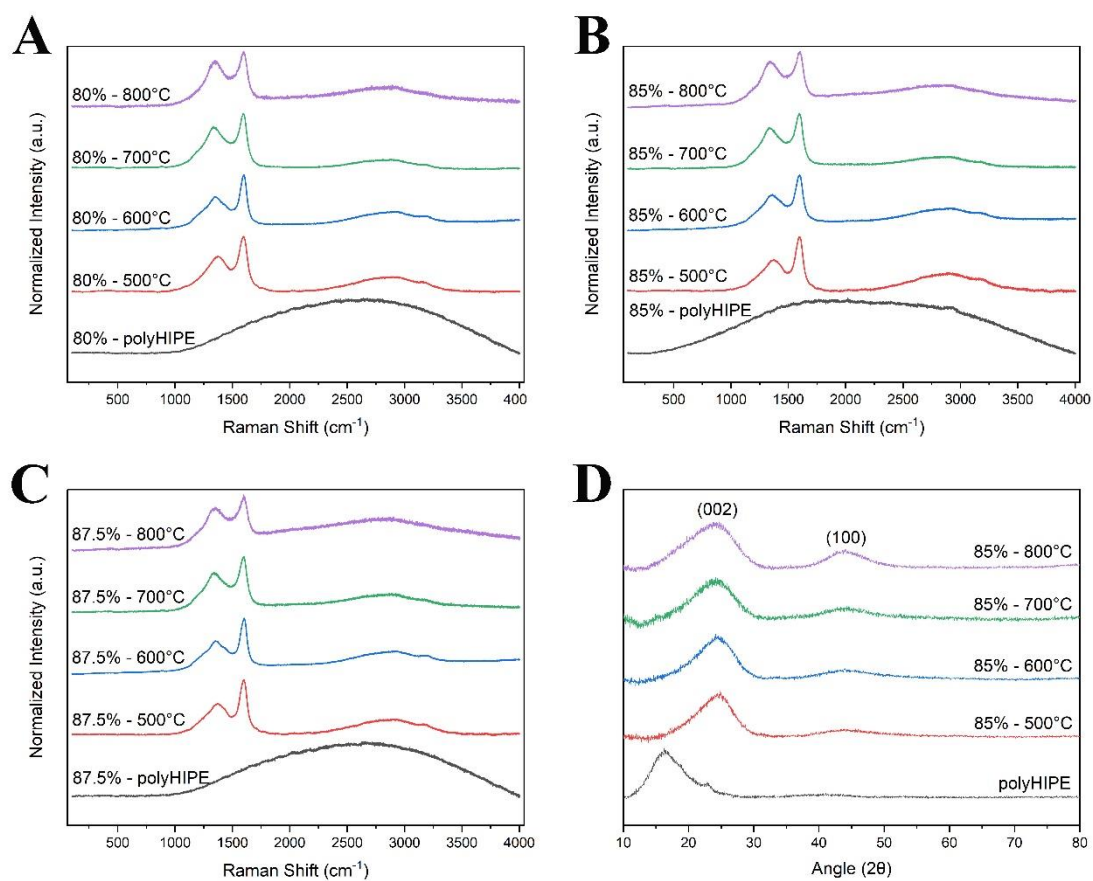
Figure A15. Raman spectra of **(A)** 80%, **(B)** 85%, and **(C)** 87.5% porous polyHIPEs and carboHIPEs fabricated at 500 °C, 600 °C, 700 °C, and 800 °C. **(D)** XRD analysis of 85% porous polyHIPE and carboHIPEs fabricated at 500 °C, 600 °C, 700 °C, and 800 °C.
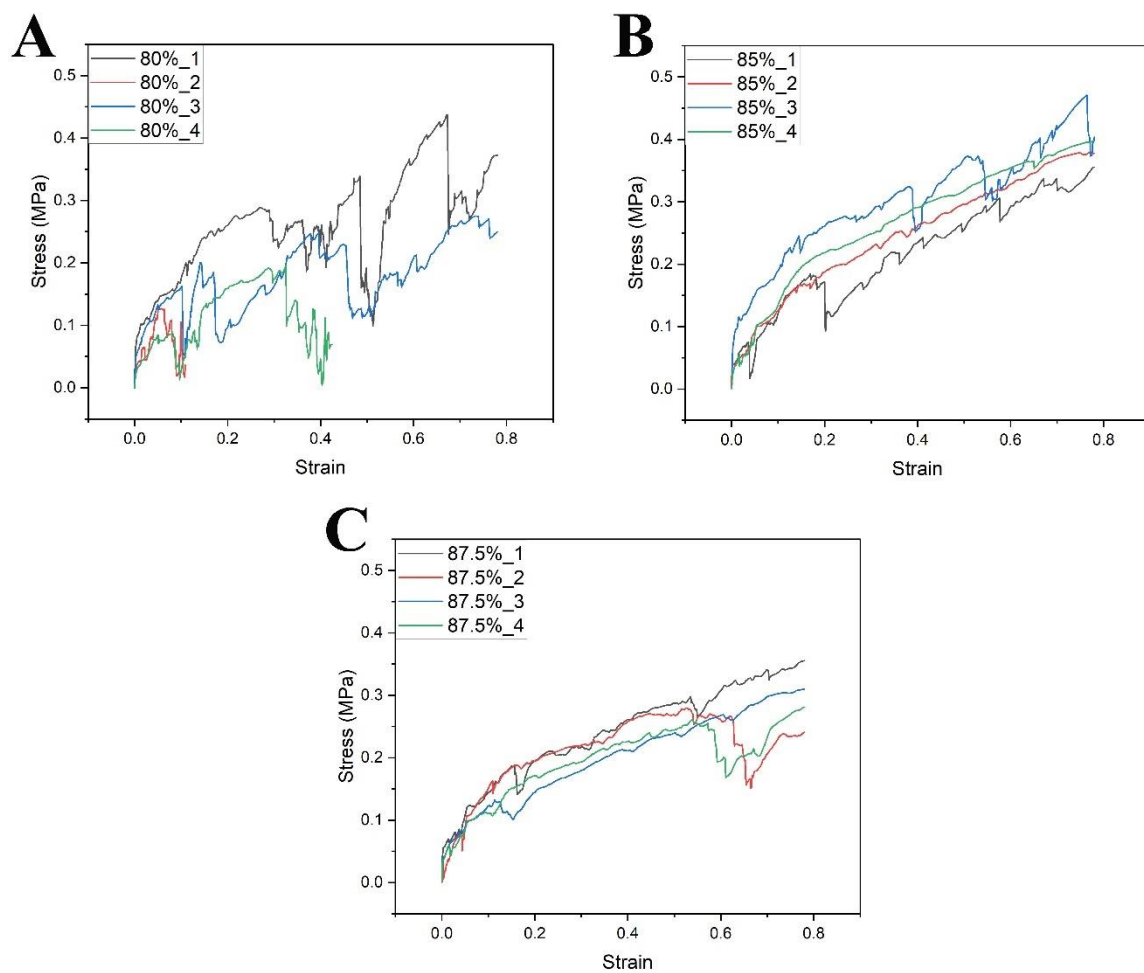
Figure A16. Stress-Strain curves of **(A)** 80%, **(B)** 85%, and **(C)** 87.5% porous carboHIPEs fabricated at 800 ℃, showing all replicates.
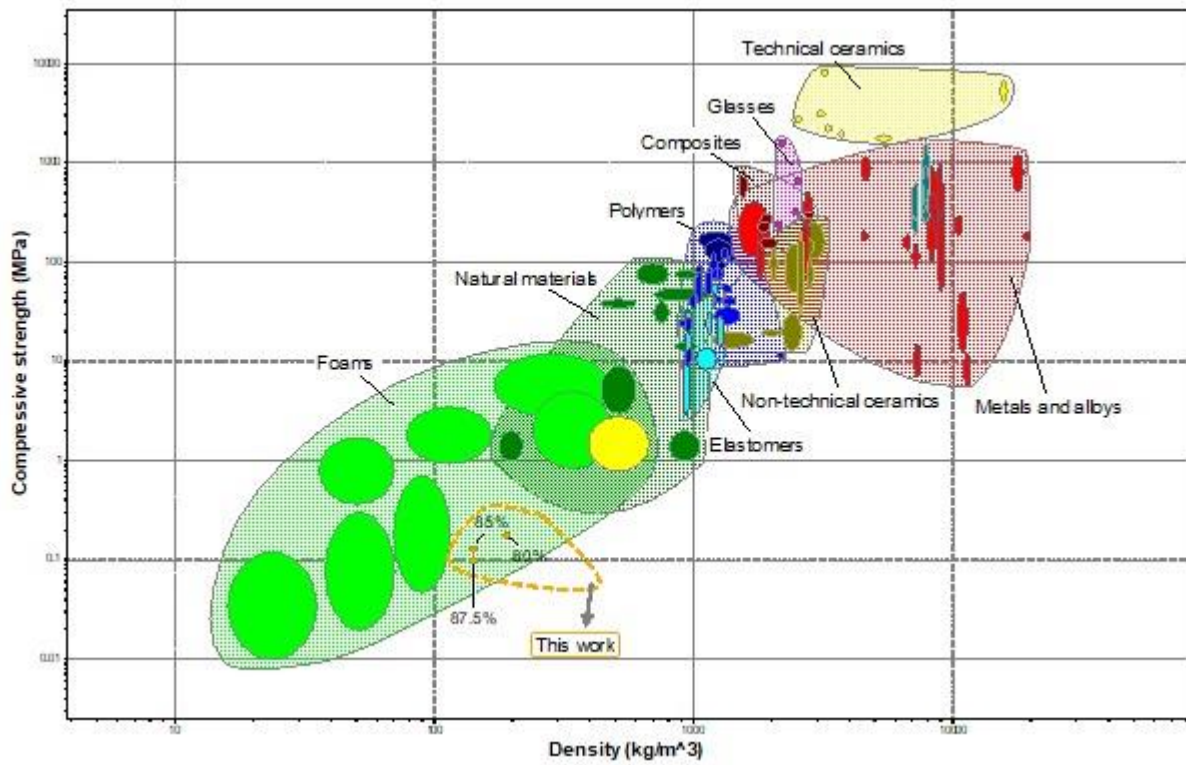
Figure A17. Ashby diagram comparing the mechanical performance of inherently porous carboHIPE lattices against other materials.

REFERENCES

[1] J. Gardan, "Additive manufacturing technologies : State of the art and trends," *Additive Manufacturing Handbook*, 149–168, **2017**, doi: 10.1201/9781315119106-10.

[2] M. Pagac *et al.*, "A review of vat photopolymerization technology: Materials, applications, challenges, and future trends of 3d printing," *Polymers*, 13, 4, 1–20, **2021**. doi: 10.3390/polym13040598.

[3] I. Gibson, D. Rosen, and B. Stucker, "Additive manufacturing technologies," *Cham, Switzerland: Springer*, 17, **2021**, doi: 10.1007/978-1-4939-2113-3.

[4] H. Kodama, "Automatic method for fabricating a three-dimensional plastic model with photo-hardening polymer," *Review of Scientific Instruments*, 52, 11, 1770–1773, **1981**, doi: 10.1063/1.1136492.

[5] C. W. Hull "Apparatus for Production of Three-Dimensional Objects by Stereolithography," *United States Patent, Appl., No. 638905*, **1984**.

[6] S. S. Crump "Apparatus and method for creating three-dimensional objects," *U.S. Patent No 5,121,329*, **1992**.

[7] "ISO/ASTM 52900 (en), Additive manufacturing — General principles — Terminology." Available from: https://www.iso.org/obp/ui/#iso:std:iso-astm:52900:dis:ed-2:v1:en [Last accessed: 10/12/2023].

[8] P. M. Bhatt, A. M. Kabir, M. Peralta, H. A. Bruck, and S. K. Gupta, "A robotic cell for performing sheet lamination-based additive manufacturing," *Addit Manuf*, 27, 278–289, **2019**, doi: 10.1016/j.addma.2019.02.002.

[9] I. Gibson, D. W. Rosen, and B. Stucker, "Sheet Lamination Processes," *Additive manufacturing technologies: rapid prototyping to direct digital manufacturing*, 223–252, **2010**, doi: 10.1007/978-1-4419-1120-9_8.

[10] B. E. Carroll, T. A. Palmer, and A. M. Beese, "Anisotropic tensile behavior of Ti-6Al-4V components fabricated with directed energy deposition additive manufacturing," *Acta Mater*, 87, 309–320, **2015**, doi: 10.1016/j.actamat.2014.12.054.

[11] A. Saboori, D. Gallo, S. Biamino, P. Fino, M. Lombardi, "An overview of additive manufacturing of titanium components by directed energy deposition: microstructure and mechanical properties," *Appl Sci, 7*, 9, 883, **2017**, doi: 10.3390/app7090883.

[12] D. S. Shim, G. Y. Baek, J. S. Seo, G. Y. Shin, K. P. Kim, and K. Y. Lee, "Effect of layer thickness setting on deposition characteristics in direct energy deposition (DED) process," *Opt Laser Technol*, 86, 69–78, **2016**, doi: 10.1016/j.optlastec.2016.07.001.

[13] Y. Bai, C. Wall, H. Pham, A. Esker, and C. B. Williams, "Characterizing Binder-Powder Interaction in Binder Jetting Additive Manufacturing Via Sessile Drop Goniometry," *J Manuf Sci Eng*, 141, 1, **2019**, doi: 10.1115/1.4041624.

[14]   P. K. Gokuldoss, S. Kolla, and J. Eckert, "Additive Manufacturing Processes: Selective Laser Melting, Electron Beam Melting and Binder Jetting-Selection Guidelines," *Materials*, 10, 6, 672, **2017**, doi: 10.3390/ma10060672.

[15]   Y. L. Yap, C. Wang, S. L. Sing, V. Dikshit, W. Y. Yeong, and J. Wei, "Material jetting additive manufacturing: An experimental study using designed metrological benchmarks," *Precis Eng*, 50, 275–285, **2017**, doi: 10.1016/j.precisioneng.2017.05.015.

[16]   H. F. Zhou *et al.*, "Compressive Strength of Thin-Walled Cellular Core by Inkjet-Based Additive Manufacturing," *1ˢᵗ International Conference on Progress in Additive Manufacturing*, **2014**, doi:10.3850/978-981-09-0446-3_077.

[17]   V. Dikshit, A. P. Nagalingam, Y. L. Yap, S. L. Sing, W. Y. Yeong, and J. Wei, "Investigation of quasi-static indentation response of inkjet printed sandwich structures under various indenter geometries," *Materials*, 10, 3, 290, **2017**, doi: 10.3390/ma10030290.

[18]   W. Y. Yeong, C. K. Chua, K. F. Leong, M. Chandrasekaran, and M. W. Lee, "Development of scaffolds for tissue engineering using a 3D inkjet model maker," *Virtual Modelling and Rapid Manufacturing: Advanced Research in Virtual and Rapid Prototyping*, 115-118, **2005**.

[19]   A. D. Kudzal, B. A. McWilliams, J. Taggart-Scarff, and M. Knezevic, "Fabrication of a low alloy ultra-high strength (>1500 MPa yield) steel using powder bed fusion additive manufacturing," *Mater Sci Eng A*, 770, 138512, **2020**, doi: 10.1016/j.msea.2019.138512.

[20]   L. Kaserer, S. Bergmueller, J. Braun, and G. Leichtfried, "Vacuum laser powder bed fusion-track consolidation, powder denudation, and future potential", *Int J Adv Manuf Technol,* 110, 3339–3346 **2020**, doi: 10.1007/s00170-020-06071-6.

[21]   D. Herzog, V. Seyda, E. Wycisk, and C. Emmelmann, "Additive manufacturing of metals," *Acta Mater*, 117, 371–392, **2016**, doi: 10.1016/j.actamat.2016.07.019.

[22]   Y. Cui *et al.*, "Manufacturing of a nanosized TiB strengthened Ti-based alloy via electron beam powder bed fusion," *Addit Manuf*, 36, 101472, **2020**, doi: 10.1016/j.addma.2020.101472.

[23]   F. Huber, M. Rasch, and M. Schmidt, "Laser powder bed fusion (Pbf-lb/m) process strategies for in-situ alloy formation with high-melting elements," *Metals*, 11, 2, 336, **2021**, doi: 10.3390/met11020336.

[24]   M. A. Saccone, "Vat photopolymerization additive manufacturing of functional materials: from batteries to metals and alloys," *California Institute of Technology ProQuest Dissertations Publishing*, **2022**, doi:10.7907/v3cn-8h28.

[25]   K. Narita, M. A. Saccone, Y. Sun, and J. R. Greer, "Additive manufacturing of 3D batteries: a perspective," *J Mater Res*, 37, 9, 1535–1546, **2022**, doi: 10.1557/S43578-022-00562-w.

[26]   M. Somireddy and A. Czekanski, "Anisotropic material behavior of 3D printed composite structures – Material extrusion additive manufacturing," *Mater Des*, 195, **2020**, doi: 10.1016/j.matdes.2020.108953.

[27] G. D. Goh, Y. L. Yap, H. K. J. Tan, S. L. Sing, G. L. Goh, and W. Y. Yeong, "Process-Structure-Properties in Polymer Additive Manufacturing via Material Extrusion: A Review," *Crit Rev Solid State Mater Sci*, 45, 2, 113–133, **2020**, doi: 10.1080/10408436.2018.1549977.

[28] Q. Sun, G. M. Rizvi, C. T. Bellehumeur, and P. Gu, "Effect of processing conditions on the bonding quality of FDM polymer filaments," *Rapid Prototyp J*, 14, 2, 72–80, **2008**, doi: 10.1108/13552540810862028.

[29] I. Gibson, D. Rosen, and B. Stucker, "Vat Photopolymerization Processes," *Additive manufacturing technologies: 3D printing, rapid prototyping, and direct digital manufacturing*, 63–106, **2015**, doi: 10.1007/978-1-4939-2113-3_4.

[30] R. V. Pazhamannil and P. Govindan, "Current state and future scope of additive manufacturing technologies via vat photopolymerization," *Mater Today Proc*, 43, 130–136, **2021**, doi: 10.1016/j.matpr.2020.11.225.

[31] M. N. Cooke, J. P. Fisher, D. Dean, C. Rimnac, and A. G. Mikos, "Use of Stereolithography to Manufacture Critical-Sized 3D Biodegradable Scaffolds for Bone Ingrowth," *J Biomed Mater Res B Appl Biomater*, 64, 2, 65–69, **2003**, doi: 10.1002/jbm.b.10485.

[32] S. A. Skoog, P. L. Goering, and R. J. Narayan, "Stereolithography in tissue engineering," *J Mater Sci Mater Med*, 25, 3, 845–856, **2014**, doi: 10.1007/s10856-013-5107-y.

[33] G. Taormina, C. Sciancalepore, M. Messori, and F. Bondioli, "3D printing processes for photocurable polymeric materials: technologies, materials, and future trends," *J Appl Biomater Functional Mater*, 16, 3, 151–160, **2018**, doi: 10.1177/2280800018764770.

[34] P. J. Bártolo, "Stereolithographic processes in Stereolithography: Materials, Processes and Applications," *Boston, MA: Springer US*, 1–36, **2011**, doi: 10.1007/978-0-387-92904-0_1.

[35] B. Redwood, B.; Schoöffer, F.; Garet, The 3D Printing Handbook: "Technologies, design and applications." *3D Hubs, Amsterdam, The Netherlands*, **2017**.

[36] B. E. Kelly, I. Bhattacharya, H. Heidari, M. Shusteff, C. M. Spadaccini, and H. K. Taylor, "Volumetric additive manufacturing via tomographic reconstruction," *Science*, 363, 6431, 1075–1079, **2019**, doi: 10.1126/science.aau7114.

[37] J. R. Tumbleston *et al.*, "Continuous liquid interface production of 3D objects," *Science*, 347, 6228, 1349–1352, **2015**, doi: 10.1126/science.aaa2397.

[38] G. Lipkowitz *et al.*, "Injection continuous liquid interface production of 3D objects," *Sci Adv*, 8, 39, **2022**, doi: 10.1126/sciadv.abq3917.

[39] L. Jiaying Tan, W. Zhu, K. Zhou, L. J. Tan, W. Zhu, and K. Zhou, "Recent Progress on Polymer Materials for Additive Manufacturing," *Adv Funct Mater*, 30, 43, 2003062, 2020, doi: 10.1002/adfm.202003062.

[40] Y. Shi, J. Chen, Y. Wang, Z. Li, and S. Huang, "Study of the selective laser sintering of polycarbonate and postprocess for parts reinforcement," *Proc Inst Mech Eng L: J Mater: Des Appl*, 221, 1, 37–42, **2007**, doi: 10.1243/14644207jmda65.

[41] E. D. Bain, E. J. Garboczi, J. E. Seppala, T. C. Parker, and K. B. Migler, "AMB2018-04: Benchmark Physical Property Measurements for Powder Bed Fusion Additive Manufacturing of Polyamide 12," *Integr Mater Manuf Innov*, 8, 3, 335–361, **2019**, doi: 10.1007/S40192-019-00146-3.

[42] M. Schmid, R. Kleijnen, M. Vetterli, and K. Wegener, "Influence of the Origin of Polyamide 12 Powder on the Laser Sintering Process and Laser Sintered Parts," *Appl Sci*, 7, 5, 462, **2017**, doi: 10.3390/app7050462.

[43] S. E. Bakarich, R. Gorkin, M. In Het Panhuis, and G. M. Spinks, "4D Printing with Mechanically Robust, Thermally Actuating Hydrogels," *Macromol Rapid Commun*, 36, 12, 1211–1217, **2015**, doi: 10.1002/marc.201500079.

[44] J. M. McCracken *et al.*, "Cellular Microcultures: Programming Mechanical and Physicochemical Properties of 3D Hydrogel Cellular Microcultures via Direct Ink Writing," *Adv Healthc Mater*, 5, 9, 990, **2016**, doi: 10.1002/adhm.201670043.

[45] B. G. Compton, J. A. Lewis, B. G. Compton, and A. Lewis, "3D-Printing of Lightweight Cellular Composites," *Adv Mater*, 26, 34, 5930–5935, **2014**, doi: 10.1002/adma.201401804.

[46] C. Mendes-Felipe, J. Oliveira, I. Etxebarria, J. L. Vilas-Vilela, and S. Lanceros-Mendez, "State-of-the-Art and Future Challenges of UV Curable Polymer-Based Smart Materials for Printing Technologies," *Adv Mater Technol*, 4, 3, 1800618, **2019**, doi: 10.1002/admt.201800618.

[47] L. Li and L. J. Lee, "Effects of inhibitors and retarders on low temperature free radical crosslinking polymerization between styrene and vinyl ester resin," *Polym Eng Sci*, 41, 1, 53–65, **2001**, doi: 10.1002/pen.10708.

[48] Z. Guo and C. Zhou, "Recent advances in ink-based additive manufacturing for porous structures," *Addit Manuf*, 48, 102405, **2021**, doi: 10.1016/j.addma.2021.102405.

[49] M. S. Silverstein, "PolyHIPEs: Recent advances in emulsion-templated porous polymers," *Prog Polym Sci*, 39, 1, 199–234, **2014**, doi: 10.1016/j.progpolymsci.2013.07.003.

[50] D. Ozdil and H. M. Aydin, "Polymers for medical and tissue engineering applications," *J Chem Technol Biotechnol*, 89, 12, 1793–1810, **2014**, doi: 10.1002/jctb.4505.

[51] F. Yang, G. Zhao, C. Zhou, and D. Lin, "Phase change materials (PCM) based cold source for selective freezing 3D printing of porous materials," *International J Adv Manuf Technol*, 95, 5–8, 2145–2155, **2018**, doi: 10.1007/s00170-017-1295-9.

[52] N. Vanderesse, I. Ky, F. Quevedo González, N. Nuño, and P. Bocher, "Image analysis characterization of periodic porous materials produced by additive manufacturing," *Mater Des*, 92, 767–778, **2016**, doi: 10.1016/j.matdes.2015.12.062.

[53] Z. Liu, J. Zhan, M. Fard, and J. L. Davy, "Acoustic properties of a porous polycarbonate material produced by additive manufacturing," *Mater Lett*, 181, 296–299, **2016**, doi: 10.1016/j.matlet.2016.06.045.

[54] L. Qian and H. Zhang, "Porogen Incorporation and Phase Inversion," *Porous Polym*, 79–117, **2011**, doi: 10.1002/9780470929445.ch3.

[55] K. J. Lissant and K. G. Mayhan, "A study of medium and high internal phase ratio water/polymer emulsions," *J Colloid Interface Sci*, 42, 1, 201–208, **1973**, doi: 10.1016/0021-9797(73)90025-8.

[56] K. J. Lissant *et al.*, "Structure of high-internal-phase-ratio emulsions," **1974**, doi: 10.1016/0021-9797(74)90273-2.

[57] B. Aldemir Dikici and F. Claeyssens, "Basic Principles of Emulsion Templating and Its Use as an Emerging Manufacturing Method of Tissue Engineering Scaffolds," *Front Bioeng Biotechnol*, 8, 875, **2020**, doi: 10.3389/fbioe.2020.00875.

[58] C. Sherborne and F. Claeyssens, "Considerations Using Additive Manufacture of Emulsion Inks to Produce Respiratory Protective Filters Against Viral Respiratory Tract Infections Such as the COVID-19 Virus," *Int J Bioprint*, 7, 1, **2021**, doi: 10.18063/ijb.v7i1.316.

[59] M. S. Silverstein, "Emulsion-templated polymers: Contemporary contemplations," *Polymer*, 126, 261–282, **2017**, doi: 10.1016/j.polymer.2017.07.046.

[60] T. Zhang, R. A. Sanguramath, S. Israel, and M. S. Silverstein, "Emulsion Templating: Porous Polymers and beyond," *Macromolecules*, 52, 15, 5445–5479, **2019**, doi: 10.1021/acs.macromol.8b02576.

[61] S. Moon, J. Q. Kim, B. Q. Kim, J. Chae, and S. Q. Choi, "Processable Composites with Extreme Material Capacities: Toward Designer High Internal Phase Emulsions and Foams ," *Chem Mater*, 32, 11, 4838-4854, **2020**, doi: 10.1021/acs.chemmater.9b04952.

[62] M. S. Silverstein and N. R. Cameron, "PolyHIPEs - Porous Polymers from High Internal Phase Emulsions," *Encyclopedia of Polymer Science and Technology*, **2010**, doi: 10.1002/0471440264.pst571.

[63] D. David and M. S. Silverstein, "Porous polyurethanes synthesized within high internal phase emulsions," *J Polym Sci A Polym Chem*, 47, 21, 5806–5814, **2009**, doi: 10.1002/pola.23624.

[64] M. Sušec, S. C. Ligon, J. Stampfl, R. Liska, and P. Krajnc, "Hierarchically porous materials from layer-by-layer photopolymerization of high internal phase emulsions," *Macromol Rapid Commun*, 34, 11, 938–943, **2013**, doi: 10.1002/marc.201300016.

[65] D. W. Johnson, C. Sherborne, M. P. Didsbury, C. Pateman, N. R. Cameron, and F. Claeyssens, "Macrostructuring of emulsion-templated porous polymers by 3D laser patterning," *Adv Mater*, 25, 23, 3178–3181, **2013**, doi: 10.1002/adma.201300552.

[66] R. Owen, C. Sherborne, T. Paterson, N. H. Green, G. C. Reilly, and F. Claeyssens, "Emulsion templated scaffolds with tunable mechanical properties for bone tissue engineering," *J Mech Behav Biomed Mater*, 54, 159–172, **2016**, doi: 10.1016/j.jmbbm.2015.09.019.

[67] A. J. Wang *et al.*, "Photocurable high internal phase emulsions (HIPEs) containing hydroxyapatite for additive manufacture of tissue engineering scaffolds with multi-scale porosity," *Mater Sci Eng C*, 67, 51–58, **2016**, doi: 10.1016/j.msec.2016.04.087.

[68] A. Malayeri *et al.*, "Osteosarcoma growth on trabecular bone mimicking structures manufactured via laser direct write," *Int J Bioprint*, 2, 2, 67–77, **2016**, doi: 10.18063/ijb.2016.02.005.

[69] C. Sherborne, R. Owen, G. C. Reilly, and F. Claeyssens, "Light-based additive manufacturing of PolyHIPEs: Controlling the surface porosity for 3D cell culture applications," *Mater Des*, 156, 494–503, **2018**, doi: 10.1016/j.matdes.2018.06.061.

[70] V. Hobiger, A.-L. Kutsch, J. Stampfl, R. Liska, S. Baudis, and P. Krajnc, "Thiol-Acrylate polyHIPEs via Facile Layer-by-Layer Photopolymerization," *3D Print Addit Manuf*, **2023**, doi: 10.1089/3dp.2022.0289.

[71] N. Sengokmen Ozsoz, S. Pashneh-Tala, and F. Claeyssens, "Optimization of a High Internal Phase Emulsion-Based Resin for Use in Commercial Vat Photopolymerization Additive Manufacturing," *3D Print Addit Manuf*, **2023**, doi: 10.1089/3dp.2022.0235.

[72] N. Sengokmen-Ozsoz, R. Boston, and F. Claeyssens, "Investigating the Potential of Electroless Nickel Plating for Fabricating Ultra-Porous Metal-Based Lattice Structures Using PolyHIPE Templates," *ACS Appl Mater Interfaces*, 15, 25, 30769–30779, **2023**, doi: 10.1021/acsami.3c04637.

[73] N. A. Sears, P. S. Dhavalikar, and E. M. Cosgriff-Hernandez, "Emulsion Inks for 3D Printing of High Porosity Materials," *Macromol Rapid Commun*, 37, 16, 1369-1374, **2016**, doi: 10.1002/marc.201600236.

[74] N. Sears, P. Dhavalikar, M. Whitely, and E. Cosgriff-Hernandez, "Fabrication of biomimetic bone grafts with multi-material 3D printing," *Biofabrication*, 9, 2, **2017**, doi: 10.1088/1758-5090/aa7077.

[75] T. Yang, Y. Hu, C. Wang, and B. P. Binks, "Fabrication of Hierarchical Macroporous Biocompatible Scaffolds by Combining Pickering High Internal Phase Emulsion Templates with Three-Dimensional Printing," *ACS Appl Mater Interfaces*, 9, 27, 22950–22958, **2017**, doi: 10.1021/acsami.7b05012.

[76] S. Ghosh *et al.*, "3D Printed Hierarchical Porous Poly(ϵ-caprolactone) Scaffolds from Pickering High Internal Phase Emulsion Templating," *Langmuir*, 39, 5, 1927–1946, **2023**, doi: 10.1021/acs.langmuir.2c02936.

[77] L. Wenger, C. P. Radtke, J. Göpper, M. Wörner, and J. Hubbuch, "3D-Printable and Enzymatically Active Composite Materials Based on Hydrogel-Filled High Internal Phase Emulsions," *Front Bioeng Biotechnol*, 8, 713, **2020**, doi: 10.3389/fbioe.2020.00713.

[78] D. P. Gregory, M. Sharpies, and I. M. Tucker, "Porous material," *European Patent Office EP0299762A2*, **1987**.

[79] M. Ovadia and M. S. Silverstein, "High porosity, responsive hydrogel copolymers from emulsion templating," *Polym Int*, 65, 3, 280–289, **2016**, doi: 10.1002/pi.5052.

[80] S. Kovačič, M. S. Silverstein, S. Kovačič, and + Silverstein, "Superabsorbent, High Porosity, PAMPS-Based Hydrogels through Emulsion Templating," *Macromol Rapid Commun*, 37, 22, 1814–1819, **2016**, doi: 10.1002/marc.201600249.

[81] M. Tebboth, A. Kogelbauer, and A. Bismarck, "Liquid-Liquid Extraction within Emulsion Templated Macroporous Polymers," *Ind Eng Chem Res*, 54, 29, 7284–7291, **2015**, doi: 10.1021/acs.iecr.5b01346.

[82] F. du *et al.*, "High-internal-phase-emulsion polymeric monolith coupled with liquid chromatography–electrospray tandem mass spectrometry for enrichment and sensitive detection of trace cytokinins in plant samples," *Anal Bioanal Chem*, 407, 20, 6071–6079, **2015**, doi: 10.1007/s00216-015-8782-3.

[83] F. Du, X. Zheng, L. Sun, Q. Qin, L. Guo, and G. Ruan, "Development and validation of polymerized high internal phase emulsion monoliths coupled with HPLC and fluorescence detection for the determination of trace tetracycline antibiotics in environmental water samples," *J Sep Sci*, 38, 21, 3774–3780, **2015**, doi: 10.1002/jssc.201500497.

[84] J. Pan *et al.*, "Wulff-type boronic acids suspended hierarchical porous polymeric monolith for the specific capture of cis-diol-containing flavone under neutral condition," *Chem Eng J*, 317, 317–330, **2017**, doi: 10.1016/j.cej.2017.02.078.

[85] F. Du *et al.*, "High Internal Phase Emulsion Polymeric Monolith Extraction Coupling with High-Performance Liquid Chromatography for the Determination of Para Red and Sudan Dyes in Chilli Samples," *Food Anal Methods*, 10, 6, 2018–2026, Jun. **2017**, doi: 10.1007/s12161-016-0751-8.

[86] R. Hu, D. Wan, and M. Jin, "Molecular nanocapsule-decorated porous monolith: preparation and elimination of cationic dyes from water," *RSC Adv*, 6, 60, 55682–55688, **2016**, doi: 10.1039/c6ra10029e.

[87] Y. Zhu, Y. Zheng, F. Wang, and A. Wang, "Fabrication of magnetic macroporous chitosan-g-poly (acrylic acid) hydrogel for removal of Cd2+ and Pb2+," *Int J Biol Macromol*, 93, 483–492, **2016**, doi: 10.1016/j.ijbiomac.2016.09.005.

[88] Y. Zhu, Y. Zheng, L. Zong, F. Wang, and A. Wang, "Fabrication of magnetic hydroxypropyl cellulose-g-poly(acrylic acid) porous spheres via Pickering high internal phase emulsion for removal of Cu2+ and Cd2+," *Carbohydr Polym*, 149, 242–250, **2016**, doi: 10.1016/j.carbpol.2016.04.107.

[89] N. Barlık, B. Keskinler, M. M. Kocakerim, and G. Akay, "Functionalized PolyHIPE polymer monoliths as an anion-exchange media for removal of nitrate ions from aqueous solutions," *Desalin Water Treat*, 57, 55, 26440–26447, **2016**, doi: 10.1080/19443994.2016.1164083.

[90] S. Yu, H. Tan, J. Wang, X. Liu, and K. Zhou, "High porosity supermacroporous polystyrene materials with excellent oil-water separation and gas permeability properties," *ACS Appl Mater Interfaces*, 7, 12, 6745–6753, **2015**, doi: 10.1021/acsami.5b00196.

[91] N. Zhang, S. Zhong, T. Chen, Y. Zhou, and W. Jiang, "Emulsion-derived hierarchically porous polystyrene solid foam for oil removal from aqueous environment," *RSC Adv*, 7, 37, 22946–22953, **2017**, doi: 10.1039/c7ra02953e.

[92] X. Chen, L. Liu, K. Liu, Q. Miao, Y. Lü, and Y. Fang, "Compressible porous hybrid monoliths: preparation via a low molecular mass gelators-based gel-emulsion approach and exceptional performances," *J Mater Chem A Mater*, 3, 48, 24322–24332, **2015**, doi: 10.1039/c5ta08342g.

[93] G. Jonschker *et al.*, "Monolithic Polymer Materials for Gas Storage," *U.S. Patent Application No. 12/865,420*, **2010.**

[94] G. Akay. "Ammonia production by integrated intensified processes," *International Patent Publication PCT WO/2012/025767*, **2012**.

[95] Q. Wang, Y. Liu, J. Chen, Z. Du, and J. Mi, "Control of Uniform and Interconnected Macroporous Structure in PolyHIPE for Enhanced CO2 Adsorption/Desorption Kinetics," *Environ Sci Technol*, 50, 14, 7879–7888, **2016**, doi: 10.1021/acs.est.6b00579.

[96] W. Yi, H. Wu, H. Wang, and Q. Du, "Interconnectivity of Macroporous Hydrogels Prepared via Graphene Oxide-Stabilized Pickering High Internal Phase Emulsions," *Langmuir*, 32, 4, 982–990, **2016**, doi: 10.1021/acs.langmuir.5b04477.

[97] M. Tebboth, A. Kogelbauer, and A. Bismarck, "Highly permeable macroporous polymers via controlled agitation of emulsion templates," *Chem Eng Sci*, 137, 786–795, **2015**, doi: 10.1016/j.ces.2015.06.047.

[98] S. Kovačič *et al.*, "Synthesis and Catalytic Performance of Hierarchically Porous MIL-100(Fe)@polyHIPE Hybrid Membranes," *Macromol Rapid Commun*, 36, 17, 1605–1611, **2015**, doi: 10.1002/marc.201500241.

[99] D. Yin, Y. Guan, H. Gu, Y. Jia, and Q. Zhang, "Polymerized high internal phase emulsion monolithic material: a novel stationary phase of thin layer chromatography," *RSC Adv*, 7, 12, 7303–7309, **2017**, doi: 10.1039/c6ra27609a.

[100] Y. Wan, Y. Feng, D. Wan, and M. Jin, "Polyamino amphiphile mediated support of platinum nanoparticles on polyHIPE as an over 1500-time recyclable catalyst," *RSC Adv*, 6, 110, 109253–109258, **2016**, doi: 10.1039/c6ra19013h.

[101] S. Choudhury, D. Connolly, and B. White, "Application of polymeric high-internal-phase-emulsion-coated stationary-phase columns in open-tubular capillary electrochromatography," *J Appl Polym Sci*, 133, 48, 44237, **2016**, doi: 10.1002/app.44237.

[102] H. Gao *et al.*, "Facile synthesis of microcellular foam catalysts with adjustable hierarchical porous structure, acid–base strength and wettability for biomass energy conversion," *J Mater Chem A Mater*, 3, 25, 13507–13518, **2015**, doi: 10.1039/c5ta02239h.

[103] Y. Ye, M. Jin, and D. Wan, "One-pot synthesis of porous monolith-supported gold nanoparticles as an effective recyclable catalyst," *J Mater Chem A Mater*, 3, 25, 13519–13525, **2015**, doi: 10.1039/c5ta02925b.

[104] T. Gitli and M. S. Silverstein, "Bicontinuous hydrogel–hydrophobic polymer systems through emulsion templated simultaneous polymerizations," *Soft Matter*, 4, 12, 2475–2485, **2008**, doi: 10.1039/b809346f.

[105] T. Gitli and M. S. Silverstein, "Emulsion templated bicontinuous hydrophobic-hydrophilic polymers: Loading and release," *Polymer*, 52, 1, 107–115, **2011**, doi: 10.1016/j.polymer.2010.11.006.

[106] I. Gurevitch and M. S. Silverstein, "One-pot synthesis of elastomeric monoliths filled with individually encapsulated liquid droplets," *Macromolecules*, 45, 16, 6450–6456, **2012**, doi: 10.1021/ma301007s.

[107] C. Warwar Damouny and M. S. Silverstein, "Hydrogel-filled, semi-crystalline, nanoparticle-crosslinked, porous polymers from emulsion templating: Structure, properties, and shape memory," *Polymer*, 82, 262–273, **2016**, doi: 10.1016/j.polymer.2015.11.040.

[108] Y. Zhu, Y. Hua, S. Zhang, Y. Wang, and J. Chen, "Open-cell macroporous bead: a novel polymeric support for heterogeneous photocatalytic reactions," *J Polym Res*, 22, 1–6, **2015**, doi: 10.1007/s10965-015-0703-9.

[109] J. L. Robinson *et al.*, "Osteoinductive PolyHIPE Foams as Injectable Bone Grafts," *Tissue Eng Part A*, 22, 5–6, 403–414, **2016**, doi: 10.1089/ten.tea.2015.0370.

[110] Y. Hu, H. Gao, Z. Du, Y. Liu, Y. Yang, and C. Wang, "Pickering high internal phase emulsion-based hydroxyapatite–poly(ε-caprolactone) nanocomposite scaffolds," *J Mater Chem B*, 3, 18, 3848–3857, **2015**, doi: 10.1039/c5tb00093a.

[111] S. Changotade *et al.*, "Preliminary in Vitro Assessment of Stem Cell Compatibility with Cross-Linked Poly(ε-caprolactone urethane) Scaffolds Designed through High Internal Phase Emulsions," *Stem Cells International*, **2015**, doi: 10.1155/2015/283796.

[112] Y. Hu *et al.*, "Facile fabrication of poly(l-Lactic Acid)-Grafted hydroxyapatite/poly(lactic-co-glycolic Acid) scaffolds by pickering high internal phase emulsion templates," *ACS Appl Mater Interfaces*, 6, 19, 17166–17175, **2014**, doi: 10.1021/am504877h.

[113] Y. Hu *et al.*, "One-Pot Fabrication of Poly(ε-Caprolactone)-Incorporated Bovine Serum Albumin/Calcium Alginate/Hydroxyapatite Nanocomposite Scaffolds by High Internal Phase Emulsion Templates," *Macromol Mater Eng*, 302, 4, 1600367, **2017**, doi: 10.1002/mame.201600367.

[114] R. S. Moglia, J. L. Holm, N. A. Sears, C. J. Wilson, D. M. Harrison, and E. Cosgriff-Hernandez, "Injectable polyHIPEs as high-porosity bone grafts," *Biomacromolecules*, 12, 10, 3621–3628, **2011**, doi: 10.1021/BM2008839.

[115] A. C. Nalawade *et al.*, "Inverse high internal phase emulsion polymerization (i-HIPE) of GMMA, HEMA and GDMA for the preparation of superporous hydrogels as a tissue engineering scaffold," *J Mater Chem B*, 4, 3, 450–460, **2016**, doi: 10.1039/c5tb01873k.

[116] S. Liu *et al.*, "High internal phase emulsions stabilised by supramolecular cellulose nanocrystals and their application as cell-adhesive macroporous hydrogel monoliths," *J Mater Chem B*, 5, 14, 2671–2678, **2017**, doi: 10.1039/c7tb00145b.

[117] H. Tan, J. Wei, G. Sun, C. Mu, W. Lin, and T. Ngai, "Interconnected macroporous 3D scaffolds templated from gelatin nanoparticle-stabilized high internal phase emulsions for biomedical applications," *Soft Matter*, 13, 21, 3871–3878, **2017**, doi: 10.1039/c7sm00706j.

[118] J. L. Robinson, R. S. Moglia, M. C. Stuebben, M. A. P. Mcenery, and E. Cosgriff-Hernandez, "Achieving interconnected pore architecture in injectable PolyHIPEs for bone tissue engineering," *Tissue Eng Part A*, 20, 5–6, 1103–1112, **2014**, doi: 10.1089/ten.tea.2013.0319.

[119] R. S. Moglia, J. L. Robinson, A. D. Muschenborn, T. J. Touchet, D. J. Maitland, and E. Cosgriff-Hernandez, "Injectable polyMIPE scaffolds for soft tissue regeneration," *Polymer*, 55, 1, 426–434, **2014**, doi: 10.1016/j.polymer.2013.09.009.

[120] M. Behl and A. Lendlein, "Shape-memory polymers," *Mater Today*, 10, 4, 20–28, **2007**, doi: 10.1016/s1369-7021(07)70047-0.

[121] I. Gurevitch and M. S. Silverstein, "Shape memory polymer foams from emulsion templating," *Soft Matter*, 8, 40, 10378–10387, **2012**, doi: 10.1039/c2sm26404h.

[122] C. Warwar, and M. S. Silverstein, "Ball of string," *Mater Today*, 16, 7, 297, **2013**, doi: 10.1016/j.mattod.2013.07.006.

[123] M. Sušec, M. Paljevac, J. Kotek, and P. Krajnc, "Microcellular open porous polyester membranes from thiol-ene polymerisations of high internal phase emulsions," *Des Monomer Polym*, 19, 6, 577–583, **2016**, doi: 10.1080/15685551.2016.1187446.

[124] S. Israel, I. Gurevitch, and M. S. Silverstein, "Carbons with a hierarchical porous structure through the pyrolysis of hypercrosslinked emulsion-templated polymers," *Polymer*, 72, 453–463, **2015**, doi: 10.1016/j.polymer.2015.02.055.

[125] K. Kapilov-Buchman, L. Portal, Y. Zhang, N. Fechler, M. Antonietti, and M. S. Silverstein, "Hierarchically porous carbons from an emulsion-templated, urea-based deep eutectic," *J Mater Chem A Mater*, 5, 31, 16376–16385, **2017**, doi: 10.1039/c7ta01958k.

[126] F. Schlüter, M. Wilhelm, and K. Rezwan, "Surfactant assisted syntheses of monolithic hybrid ceramics with hierarchical porosity," *J Eur Ceram Soc*, 35, 11, 2963–2972, **2015**, doi: 10.1016/j.jeurceramsoc.2015.03.034.

[127] U. M. Patil *et al.*, "PolyHIPE Derived Freestanding 3D Carbon Foam for Cobalt Hydroxide Nanorods Based High Performance Supercapacitor," *Sci Rep*, 6, 1, 35490, 2016, doi: 10.1038/srep35490.

[128] M. Depardieu, M. Viaud, A. Buguin, J. Livage, C. Sanchez, and R. Backov, "A multiscale study of bacterial proliferation modes within novel E. coli @Si(HIPE) hybrid macrocellular living foams," *J Mater Chem B*, 4, 13, 2290–2303, **2016**, doi: 10.1039/c5tb02554k.

[129] N. R. Cameron, "High internal phase emulsion templating as a route to well-defined porous polymers," *Polymer*, 46, 5, 1439–1449, **2005**, doi: 10.1016/j.polymer.2004.11.097.

[130] E. Durgut, C. Sherborne, B. Aldemir Dikici, G. C. Reilly, and F. Claeyssens, "Preparation of Interconnected Pickering Polymerized High Internal Phase Emulsions by Arrested Coalescence," *Langmuir*, 38, 36, 10953–10962, **2022**, doi: 10.1021/acs.langmuir.2c01243.

[131] X. Mu *et al.*, "Porous polymeric materials by 3D printing of photocurable resin," *Mater Horiz*, 4, 3, 442–449, **2017**, doi: 10.1039/c7mh00084g.

[132] J. W. Choi, R. B. Wicker, S. H. Cho, C. S. Ha, and S. H. Lee, "Cure depth control for complex 3D microstructure fabrication in dynamic mask projection microstereolithography," *Rapid Prototyp J*, 15, 1, 59–70, **2009**, doi: 10.1108/13552540910925072.

[133] "Kudo 3D Printing Guide." Available from: https://www.dropbox.com/s/qs7c1w95drgmu1l/Kudo3D_Printing_Guide_v1.7.pdf?dl= 0 [Last accessed: 10/12/2023].

[134] J. Field, J. W. Haycock, F. M. Boissonade, and F. Claeyssens, "A Tuneable, Photocurable, Poly(Caprolactone)-Based Resin for Tissue Engineering—Synthesis, Characterisation and Use in Stereolithography," *Molecules*, 26, 5, 1199, 2021, doi: 10.3390/molecules26051199.

[135] "Hollow(er) Calibration Pyramid." Available from: https://www.thingiverse.com/thing:29429 [Last accessed: 10/12/2023].

[136] "C60 carbon fullerene buckyball." Available from: https://www.thingiverse.com/thing:4077417 [Last accessed: 10/12/2023].

[137] R. J. Carnachan, M. Bokhari, S. A. Przyborski, and N. R. Cameron, "Tailoring the morphology of emulsion-templated porous polymers," *Soft Matter*, 2, 7, 608–616, **2006**, doi: 10.1039/b603211g.

[138] S. Pashneh-Tala, R. Moorehead, and F. Claeyssens, "Hybrid manufacturing strategies for tissue engineering scaffolds using methacrylate functionalised poly(glycerol sebacate)," *J Biomater Appl*, 34, 8, 1114–1130, **2020**, doi: 10.1177/0885328219898385.

[139] J. Luo *et al.*, "Recent advances in separation applications of polymerized high internal phase emulsions," *J Sep Sci*, 44, 1, 169–187, **2021**. doi: 10.1002/jssc.202000612.

[140] S. Kramer, N. R. Cameron, and P. Krajnc, "Porous polymers from high internal phase emulsions as scaffolds for biological applications," *Polymers*, 13, 11, 1786, **2021**, doi: 10.3390/polym13111786.

[141] J. S. Choi, H. W. Kang, I. H. Lee, T. J. Ko, and D. W. Cho, "Development of micro-stereolithography technology using a UV lamp and optical fiber," *J Adv Manuf Technol*, 41, 281–286, **2009**, doi: 10.1007/s00170-008-1461-1.

[142] L. H. Han, G. Mapili, S. Chen, and K. Roy, "Freeform fabrication of biological scaffolds by projection photopolymerization," *2007 International Solid Freeform Fabrication Symposium*, **2007**.

[143] M. S. Pham, C. Liu, I. Todd, and J. Lertthanasarn, "Damage-tolerant architected materials inspired by crystal microstructure," *Nature*, 565, 7739, 305–311, **2019**, doi: 10.1038/s41586-018-0850-3.

[144] L. J. Gibson, "Cellular solids," *Mrs Bulletin*, 28, 4, 270-274, **2003**, doi: 10.1017/cbo9781139878326.

[145] Y. Zeng, X. Du, H. Yao, P. Li, P. Dong, and J. Chen, "An Nylon lattice structure with improved mechanical property and energy absorption capability," *JCOMC*, 8, 100285, **2022**, doi: 10.1016/j.jcomc.2022.100285.

[146] T. A. Schaedler *et al.*, "Ultralight metallic microlattices," *Science*, 334, 6058, 962–965, **2011**, doi: 10.1126/science.1211649.

[147] L. J. Gibson, "Modelling the mechanical behavior of cellular materials," *Mater Sci Eng A*, 110, 1–36, **1989**, doi: 10.1016/0921-5093(89)90154-8.

[148] A. G. Evans, J. W. Hutchinson, and M. F. Ashby, "Multifunctionality of cellular metal systems," *Prog Mater Sci*, 43, 3, 171–221, **1998**, doi: 10.1016/s0079-6425(98)00004-8.

[149] C. Pan, Y. Han, and J. Lu, "Design and optimization of lattice structures: A review," *Appl Sci*, 10, 18, 6374, **2020**, doi: 10.3390/app10186374.

[150] M. F. Ashby, "The properties of foams and lattices," *Philos Trans R Soc A*, 364, 1838, 15–30, **2006**, doi: 10.1098/rsta.2005.1678.

[151] S. Wang, Y. Ma, and Z. Deng, "Stretching-dominated truss lattice materials: Elastic anisotropy evaluation, control, and design," *Compos Struct*, 298, 116004, **2022**, doi: 10.1016/j.compstruct.2022.116004.

[152] T. Kim, C. Y. Zhao, T. J. Lu, and H. P. Hodson, "Convective heat dissipation with lattice-frame materials," *Mech Mater*, 36, 8, 767–780, **2004**, doi: 10.1016/j.mechmat.2003.07.001.

[153] A. G. Evans, J. W. Hutchinson, N. A. Fleck, M. F. Ashby, and H. N. G. Wadley, "The topological design of multifunctional cellular metals," *Prog Mater Sci*, 46, 3-4, 309-327, **2001**, doi: 10.1016/s0079-6425(00)00016-5.

[154] J. Xu, Y. Gao, H. Huang, Q. Yang, L. Guo, and L. Jiang, "Diamond-structured hollow-tube lattice Ni materials via 3D printing," *Sci China Chem*, 59, 1632–1637, **2016**, doi: 10.1007/s11426-016-0093-x.

[155] S. H. Ahn, H. J. Lee, and G. H. Kim, "Polycaprolactone scaffolds fabricated with an advanced electrohydrodynamic direct-printing method for bone tissue regeneration," *Biomacromolecules*, 12, 12, 4256–4263, **2011**, doi: 10.1021/bm201126j.

[156] Y. Takahashi, D. Okumura, and N. Ohno, "Yield and buckling behavior of Kelvin open-cell foams subjected to uniaxial compression," *Int J Mech Sci*, 52, 2, 377–385, **2010**, doi: 10.1016/j.ijmecsci.2009.10.009.

[157] K. Maloney *et al.*, "Microlattices as architected thin films: Analysis of mechanical properties and high strain elastic," *APL Mater*, 1, 2, **2013**, doi: 10.1063/1.4818168.

[158] T. J. Lu, L. Valdevit, and A. G. Evans, "Active cooling by metallic sandwich structures with periodic cores," *Prog Mater Sci*, 50, 7, 789–815, **2005**, doi: 10.1016/j.pmatsci.2005.03.001.

[159] C. S. Roper *et al.*, "Scalable 3D Bicontinuous Fluid Networks: Polymer Heat Exchangers Toward Artificial Organs," *Adv Mater*, 27, 15, 2479–2484, **2015**, doi: 10.1002/adma.201403549.

[160] Y. Liu, T. A. Schaedler, A. J. Jacobsen, and X. Chen, "Quasi-static energy absorption of hollow microlattice structures," *Compos B Eng*, 67, 39–49, **2014**, doi: 10.1016/j.compositesb.2014.06.024.

[161] Z. P. Sun, Y. B. Guo, and V. P. W. Shim, "Deformation and energy absorption characteristics of additively-manufactured polymeric lattice structures — Effects of cell topology and material anisotropy," *Thin-Walled Struct*, 169, 108420, **2021**, doi: 10.1016/j.tws.2021.108420.

[162] T. A. Schaedler, A. J. Jacobsen, and W. B. Carter, "Toward lighter, stiffer materials," *Science*, 341, 6151, 1181–1182, **2013**, doi: 10.1126/science.1243996.

[163] O. Al-Ketan, R. Rowshan, and R. K. Abu Al-Rub, "Topology-mechanical property relationship of 3D printed strut, skeletal, and sheet based periodic metallic cellular materials," *Addit Manuf*, 19, 167–183, **2018**, doi: 10.1016/j.addma.2017.12.006.

[164] Q. Fan, Y. Gao, Y. Zhao, Q. Yang, L. Guo, and L. Jiang, "Fabrication of diamond-structured composite materials with Ni-P-diamond particles by electroless plating," *Mater Lett*, 215, 242–245, **2018**, doi: 10.1016/j.matlet.2017.12.065.

[165] T. M. Tillotson and L. W. Hrubesh, "Transparent ultralow-density silica aerogels prepared by a two-step sol-gel process," *J Non Cryst Solids*, 145, 44–50, **1992**, doi: 10.1016/S0022-3093(05)80427-2.

[166] H. Hu *et al.*, "Ultralight and Highly Compressible Graphene Aerogels," *Adv Mater*, 25, 15, 2219–2223, **2013**, doi: 10.1002/adma.201204530.

[167] J. Zou *et al.*, "Ultralight multiwalled carbon nanotube aerogel," *ACS Nano*, 4, 12, 7293–7302, **2010**, doi: 10.1021/nn102246a.

[168] V. S. Deshpande, N. A. Fleck, and M. F. Ashby, "Effective properties of the octet-truss lattice material," *J Mech Phys Solids*, vol. 49, no. 8, pp. 1747–1769, Aug. 2001, doi: 10.1016/S0022-5096(01)00010-2.

[169] L. M. Moreau, D. H. Ha, C. R. Bealing, H. Zhang, R. G. Hennig, and R. D. Robinson, "Unintended phosphorus doping of nickel nanoparticles during synthesis with TOP: A discovery through structural analysis," *Nano Lett*, 12, 9, 4530–4539, **2012**, doi: 10.1021/nl301642g/.

[170] G. Dai, S. Wu, X. Huang, X. Zhang, and M. Wang, "A novel strategy for designable alloy coatings in electroless plating," *Trans Ins Met Finish*, 101, 2, 101-112, **2022**, doi: 10.1080/00202967.2022.2108574.

[171] J. Liu, X. Zhao, Q. Yang, K. Wang, Y. Fu, and Q. Yang, "Particle-reinforced ultralight hollow Ni-P-B4C microlattice composite materials," *Mater Lett*, 331, 133438, **2023**, doi: 10.1016/j.matlet.2022.133438.

[172] L. Xiao, G. Feng, S. Li, K. Mu, Q. Qin, and W. Song, "Mechanical characterization of additively-manufactured metallic lattice structures with hollow struts under static and dynamic loadings," *Int J Impact Eng*, 169, **2022**, doi: 10.1016/j.ijimpeng.2022.104333.

[173] M. G. Rashed, M. Ashraf, R. A. W. Mines, and P. J. Hazell, "Metallic microlattice materials: A current state of the art on manufacturing, mechanical properties and applications," *Mater Des*, 95, 518–533, **2016**, doi: 10.1016/j.matdes.2016.01.146.

[174] H. Barkan-Öztürk, A. Menner, A. Bismarck, and R. T. Woodward, "Simultaneous hypercrosslinking and functionalization of polyHIPEs for use as coarse powder catalyst supports," *Chem Eng Sci*, 264, 118151, **2022**, doi: 10.1016/j.ces.2022.118151.

[175] S. H. Park, T. W. Lim, D. Y. Yang, N. C. Cho, and K. S. Lee, "Fabrication of a bunch of sub- 30-nm nanofibers inside microchannels using photopolymerization via a long exposure technique," *Appl Phys Lett*, 89, 17, **2006**, doi: 10.1063/1.2363956.

[176] L. Li and B. Liu, "Study of Ni-catalyst for electroless Ni-P deposition on glass fiber," *Mater Chem Phys*, 128, 1–2, 303–310, **2011**, doi: 10.1016/j.matchemphys.2011.03.026.

[177] C. A. Loto, "Electroless Nickel Plating – A Review," *Silicon*, 8, 177–186, 2016, doi: 10.1007/s12633-015-9367-7.

[178] Z. Sun, J. Huang, L. Wang, X. Zhang, M. Li, and B. Tang, "Method for electroless nickel plating on poly(ethylene terephthalate) substrate modified with primer and self-assembled monolayer," *J Mater Sci Mater Electron*, 26, 10132–10137, **2015**, doi: 10.1007/s10854-015-3698-4.

[179] "Elegoo Mars 3 Pro 4K." Available from: https://www.elegoo.com/en-gb/products/elegoo-mars-3-pro-4k-mono-lcd-3d-printer?gclid=Cj0KCQiAo-yfBhD_ARIsANr56g6ldqxk30RhtsTBwGnvJs9PHPmltJaCjl5RIYSeD7J3CnXv_tl8I_waAuxaEALw_wcB [Last accessed: 10/12/2023].

[180] A. Uhlemann, "Lattice Structures - Mikrostrukturen." Available from: https://www.thingiverse.com/thing:2788117 [Last accessed: 10/12/2023].

[181] "Caswell UK." Available from: https://www.caswelleurope.co.uk/electroless-nickel-part-a/ [Last accessed: 10/12/2023].

[182] A. Barbetta and N. R. Cameron, "Morphology and surface area of emulsion-derived (PolyHIPE) solid foams prepared with oil-phase soluble porogenic solvents: Span 80 as surfactant," *Macromolecules*, 37, 9, 3188–3201, **2004**, doi: 10.1021/MA0359436.

[183] "IR Spectrum Table." Available from: https://www.sigmaaldrich.com/GB/en/technical-documents/technical-article/analytical-chemistry/photometry-and-reflectometry/ir-spectrum-table [Last accessed: 10/12/2023].

[184] R. F. S. Lenza and W. L. Vasconcelos, "Structural evolution of silica sols modified with formamide," *Mater Res*, 4, 3, 175–179, **2001**, doi: 10.1590/S1516-14392001000300006.

[185] S. Sotiropoulos, I. J. Brown, G. Akay, and E. Lester, "Nickel incorporation into a hollow fibre microporous polymer: a preparation route for novel high surface area nickel structures," *Mater Lett*, 35, 5-6, 383–391, **1998**, doi: 10.1016/S0167-577X(97)00283-8.

[186] G. Akay and B. Calkan, "Preparation of nanostructured microporous metal foams through flow induced electroless deposition," *J Nanomater*, 16, 1, 271, **2015**, doi: 10.1155/2015/275705.

[187] H. Pfeiffer, F. Tancret, and T. Brousse, "Synthesis, characterization and thermal stability of Ni3P coatings on nickel," *Mater Chem Phys*, 92, 2–3, 534–539, **2005**, doi: 10.1016/j.matchemphys.2005.01.055.

[188] Z. Yu *et al.*, "Ni3P as a high-performance catalytic phase for the hydrodeoxygenation of phenolic compounds," *Green Chem*, 20, 3, 609–619, **2018**, doi: 10.1039/c7gc03262e.

[189] R. T. Woodward, A. Jobbe-Duval, S. Marchesini, D. B. Anthony, C. Petit, and A. Bismarck, "Hypercrosslinked polyHIPEs as precursors to designable, hierarchically porous carbon foams," *Polymer*, 115, 146–153, **2017**, doi: 10.1016/j.polymer.2017.03.042.

[190] A. D. Roberts, X. Li, and H. Zhang, "Porous carbon spheres and monoliths: morphology control, pore size tuning and their applications as Li-ion battery anode materials," *Chem Soc Rev*, 43, 13, 4341–4356, **2014**, doi: 10.1039/c4cs00071d.

[191] M. Inagaki, H. Konno, and O. Tanaike, "Carbon materials for electrochemical capacitors," *J Power Sources*, 195, 24, 7880–7903, **2010**, doi: 10.1016/j.jpowsour.2010.06.036.

[192] G. Crini, "Non-conventional low-cost adsorbents for dye removal: A review," *Bioresour Technol*, 97, 9, 1061–1085, **2006**, doi: 10.1016/j.biortech.2005.05.001.

[193] S. Babel and T. A. Kurniawan, "Low-cost adsorbents for heavy metals uptake from contaminated water: a review," *J Hazard Mater*, 97, 1–3, 219–243, **2003**, doi: 10.1016/S0304-3894(02)00263-7.

[194] Y. Zhao, X. Liu, and Y. Han, "Microporous carbonaceous adsorbents for CO2 separation via selective adsorption," *RSC Adv*, 5, 38, 30310–30330, **2015**, doi: 10.1039/c5ra00569h.

[195] M. A. Mudassir *et al.*, "Emulsion-derived porous carbon-based materials for energy and environmental applications," *Renew Sustain Energy Rev*, 185, 113594 **2023**, doi: 10.1016/j.rser.2023.113594.

[196] J. Wang, H. Kong, J. Zhang, Y. Hao, Z. Shao, and F. Ciucci, "Carbon-based electrocatalysts for sustainable energy applications," *Prog Mater Sci*, 116, 100717, **2021**, doi: 10.1016/j.pmatsci.2020.100717.

[197] J. Lee, J. Kim, and T. Hyeon, "Recent Progress in the Synthesis of Porous Carbon Materials," *Adv Mater*, 18, 16, 2073–2094, **2006**, doi: 10.1002/adma.200501576.

[198] N. Patel, K. Okabe, and A. Oya, "Designing carbon materials with unique shapes using polymer blending and coating techniques," *Carbon*, 40, 3, 315–320, **2002**, doi: 10.1016/S0008-6223(01)00101-4.

[199] J. Gao *et al.*, "High performance of N, P co-doped metal-free carbon catalyst derived from ionic liquid for oxygen reduction reaction," *J Solid State Electrochem*, 22, 2, 519–525, **2018**, doi: 10.1007/s10008-017-3785-y.

[200] M. M. Rahman, M. M. Alam, A. M. Asiri, and M. R. Awual, "Fabrication of 4-aminophenol sensor based on hydrothermally prepared ZnO/Yb 2 O 3 nanosheets," *New J Chem*, 41, 17, 9159–9169, **2017**, doi: 10.1039/c7nj01623a.

[201] Z. Yan, Z. Peng, and J. M. Tour, "Chemical vapor deposition of graphene single crystals," *Acc Chem Res*, 47, 4, 1327–1337, **2014**, doi: 10.1021/ar4003043.

[202] O. S. G. P. Soares, R. P. Rocha, A. G. Gonçalves, J. L. Figueiredo, J. J. M. Órfão, and M. F. R. Pereira, "Easy method to prepare N-doped carbon nanotubes by ball milling," *Carbon*, 91, 114–121, **2015**, doi: 10.1016/j.carbon.2015.04.050.

[203] R. Borgohain, J. Yang, J. P. Selegue, and D. Y. Kim, "Controlled synthesis, efficient purification, and electrochemical characterization of arc-discharge carbon nano-onions," *Carbon*, 66, 272–284, **2014**, doi: 10.1016/j.carbon.2013.09.001.

[204] S. Joseph *et al.*, "Recent Advances in Functionalized Nanoporous Carbons Derived from Waste Resources and Their Applications in Energy and Environment," *Adv Sustain Syst*, 5, 1, 2000169, **2021**, doi: 10.1002/adsu.202000169.

[205] M. A. Mudassir, H. Z. Aslam, T. M. Ansari, H. Zhang, and I. Hussain, "Fundamentals and Design-Led Synthesis of Emulsion-Templated Porous Materials for Environmental Applications," *Adv Sci*, 8, 22, 2102540, **2021**, doi: 10.1002/advs.202102540.

[206] B. Aldemir Dikici, S. Dikici, and F. Claeyssens, "Synergistic effect of type and concentration of surfactant and diluting solvent on the morphology of emulsion templated matrices developed as tissue engineering scaffolds," *React Funct Polym*, 180, 105387, **2022**, doi: 10.1016/j.reactfunctpolym.2022.105387.

[207] A. Menner, V. Ikem, M. Salgueiro, M. S. P. Shaffer, and A. Bismarck, "High internal phase emulsion templates solely stabilised by functionalised titania nanoparticles," *Chem Comm*, 41, 4274–4276, **2007**, doi: 10.1039/b708935j.

[208] E. Durgut, M. Zhou, B. A. Dikici, R. Foudazi, and F. Claeyssens, "Modifying Pickering Polymerized High Internal Phase Emulsion Morphology by Adjusting Particle Hydrophilicity," *Colloids Surf A Physicochem Eng Asp*, 680, 132629, **2024**, doi: 10.1016/j.colsurfa.2023.132629.

[209] R. Foudazi, "HIPEs to PolyHIPEs," *React Funct Polym*, 164, 104917, **2021**, doi: 10.1016/j.reactfunctpolym.2021.104917.

[210] D. Wang, "Preparation, properties and applications of highly porous polymer, carbon, and silica-carbon monoliths derived from high internal phase emulsions," **2004**.

[211] D. Wang, N. L. Smith, and P. M. Budd, "Polymerization and carbonization of high internal phase emulsions," *Polym Int*, 54, 2, 297–303, **2005**, doi: 10.1002/pi.1672.

[212] R. T. Woodward *et al.*, "Hierarchically porous carbon foams from pickering high internal phase emulsions," *Carbon*, 101, 253–260, **2016**, doi: 10.1016/j.carbon.2016.02.002.

[213] R. T. Woodward, F. De Luca, A. D. Roberts, and A. Bismarck, "High-Surface-Area, Emulsion-Templated Carbon Foams by Activation of polyHIPEs Derived from Pickering Emulsions," *Materials*, 9, 9, 776, **2016**, doi: 10.3390/ma9090776.

[214] S. Ungureanu *et al.*, "First Biosourced Monolithic Macroporous SiC/C Composite Foams (Bio-SiC/C(HIPE)) Bearing Unprecedented Heat Transport Properties," *Adv Eng Mater*, 15, 10, 893–902, **2013**, doi: 10.1002/adem.201300015.

[215] N. Cohen and M. S. Silverstein, "Synthesis of emulsion-templated porous polyacrylonitrile and its pyrolysis to porous carbon monoliths," *Polymer*, 52, 2, 282–287, **2011**, doi: 10.1016/j.polymer.2010.11.026.

[216] M. Liu *et al.*, "Carbon foams prepared by an oil-in-water emulsion method," *Carbon*, 45, 13, 2710–2712, **2007**, doi: 10.1016/j.carbon.2007.08.004.

[217] A. Szczurek, V. Fierro, A. Pizzi, and A. Celzard, "Emulsion-templated porous carbon monoliths derived from tannins," *Carbon*, 74, 352–362, **2014**, doi: 10.1016/j.carbon.2014.03.047.

[218] R. Woodward *et al.*, "Carbon Foams from Polyhipe/Reduced Graphene Oxide Composites and Their Performance As Electrodes in Supercapacitor Devices," *AIChE Annual Meeting*, **2016**.

[219] R. T. Woodward *et al.*, "Carbon foams from emulsion-templated reduced graphene oxide polymer composites: electrodes for supercapacitor devices," *J Mater Chem A*, 6, 4, 1840–1849, **2018**, doi: 10.1039/c7ta09893f.

[220] H. D. Asfaw *et al.*, "Boosting the thermal stability of emulsion–templated polymers via sulfonation: an efficient synthetic route to hierarchically porous carbon foams," *ChemistrySelect*, 1, 4, 784–792, **2016**, doi: 10.1002/slct.201600139.

[221] Y. Kawai and T. Yamamoto, "Synthesis of porous carbon hollow particles maintaining their structure using hyper-cross-linked Poly(St-DVB) hollow particles," *Adv Powder Technol*, 31, 2, 614–620, **2020**, doi: 10.1016/j.apt.2019.11.016.

[222] Z. Wang, D. Cheng, C. Chen, and K. Zhou, "Hierarchically porous carbon microspheres with fully open and interconnected super-macropores for air cathodes of Zn-Air batteries," *Carbon*, 136, 54–62, **2018**, doi: 10.1016/j.carbon.2018.04.061.

[223] H. D. Asfaw, M. Roberts, R. Younesi, and K. Edström, "Emulsion-templated bicontinuous carbon network electrodes for use in 3D microstructured batteries," *J Mater Chem A*, 1, 44, 13750–13758, **2013**, doi: 10.1039/c3ta12680c.

[224] A. Suresh, S. J. Rowan, and C. Liu, "Macroscale Fabrication of Lightweight and Strong Porous Carbon Foams through Template-Coating Pair Design," *Adv Mater*, 35, 9, **2023**, doi: 10.1002/adma.202206416.

[225] N. Díez, M. Sevilla, and A. B. Fuertes, "Synthesis strategies of templated porous carbons beyond the silica nanocasting technique," *Carbon*, 178, 451–476, **2021**, doi: 10.1016/j.carbon.2021.03.029.

[226] "Elegoo Saturn 2 8K." Available: https://www.elegoo.com/products/elegoo-saturn-2-8k-10-inches-mono-lcd-3d-printer [Last accessed: 10/12/2023].

[227] S. Bernard, O. Beyssac, K. Benzerara, N. Findling, G. Tzvetkov, and G. E. Brown, "XANES, Raman and XRD study of anthracene-based cokes and saccharose-based chars submitted to high-temperature pyrolysis," *Carbon*, 48, 9, 2506–2516, **2010**, doi: 10.1016/j.carbon.2010.03.024.

[228] Z. Q. Li, C. J. Lu, Z. P. Xia, Y. Zhou, and Z. Luo, "X-ray diffraction patterns of graphite and turbostratic carbon," *Carbon*, 45, 8, 1686–1695, **2007**, doi: 10.1016/j.carbon.2007.03.038.

[229] Y. Chen, H. Liu, J. Shen, J. Gong, and J. Zhao, "Compression Behavior of Diamond Lattice Structure and Its Hall–Petch Relationship," *Adv Eng Mater*, 23, 3, 2001024, **2021**, doi: 10.1002/adem.202001024.

[230] İ. Uzun, İ. Orak, Ö. Sevgili, E. Yiğit, and M. Karakaplan, "Synthesis of canthaxanthin from β-carotene and evaluation of both substances in diode construction," *J Mater Sci: Mater Electron*, 33, 4, 1888–1898, **2022**, doi: 10.1007/S10854-021-07389-x.

[231] "Molecular structure of beta-carotene ." Available from: https://www.sigmaaldrich.com/GB/en/product/sigma/22040?utm_source=google&utm_medium=cpc&utm_campaign=15001183893&utm_content=129932657698&gclid=Cj0KCQjw-r-vBhC-ARIsAGgUO2AZ2QV5NSaXLZsVEcaBkRVe_pbNW6oWvteupivjVSNz6x4pmwND-FEaAvlREALw_wcB [Last accessed: 14/03/2024].

[232] M. Leulescu *et al.*, "Tartrazine: physical, thermal and biophysical properties of the most widely employed synthetic yellow food-colouring azo dye," *J Therm Anal Calorim*, 134, 1, 209–231, **2018**, doi: 10.1007/S10973-018-7663-3.

[233] "Molecular structure of tartrazine." Available from: https://www.sigmaaldrich.com/GB/en/product/sigma/t0388 [Last accessed: 14/03/2024].